

A multipolar effective one body waveform model for spin-aligned black hole binaries.

Alessandro Nagar^{1,2}, Gunnar Riemenschneider^{1,3}, Geraint Pratten^{4,5}, Piero Retteno^{1,2}, and Francesco Messina^{6,7}

¹*INFN Sezione di Torino, Via P. Giuria 1, 10125 Torino, Italy*

²*Institut des Hautes Etudes Scientifiques, 91440 Bures-sur-Yvette, France*

³*Dipartimento di Fisica, Università di Torino, via P. Giuria 1, 10125 Torino, Italy*

⁴*School of Physics and Astronomy and Institute for Gravitational Wave Astronomy, University of Birmingham, Edgbaston, Birmingham, B15 9TT, United Kingdom*

⁵*Departament de Física, Universitat de les Illes Balears and Institut d'Estudis Espacials de Catalunya, Crta. Valldemossa km 7.5, E-07122 Palma, Spain*

⁶*Dipartimento di Fisica, Università degli studi di Milano Bicocca, Piazza della Scienza 3, 20126 Milano, Italy and*

⁷*INFN, Sezione di Milano Bicocca, Piazza della Scienza 3, 20126 Milano, Italy*

We introduce `TEOBiResumS.SM`, an improved version of the effective-one-body (EOB) waveform model `TEOBResumS` for spin-aligned, coalescing black hole binaries, that includes subdominant gravitational waveform modes completed through merger and ringdown. Beyond the dominant $(\ell, |m|) = (2, 2)$ one, the more robust multipoles all over the parameter space are: $(2, 1)$, $(3, 3)$, $(3, 2)$, $(4, 4)$ and $(5, 5)$. Modes as $(3, 1)$, $(4, 3)$ and $(4, 2)$ can also be generated, but are less robust. The multipolar ringdown EOB waveform stems from suitably fitting many numerical relativity (NR) waveform data from the Simulating eXtreme Spacetimes (SXS) collaboration together with test-mass waveform data. Mode-mixing effects are not incorporated. The orbital (nonspinning) part of the multipolar waveform amplitudes includes test-mass results up to (relative) 6PN order and, for most modes, is Padé resummed. The m -odd waveform multipoles (up to $\ell = 5$) incorporate most of the currently available spin-dependent analytical information. Each multipolar amplitude is additionally orbital-factorized and resummed. Improving on previous work, we confirm that certain $m = \text{odd}$ modes, e.g. the $(2, 1)$, and even the $(3, 1)$, may develop a zero (or a minimum) in the amplitude for nearly equal-mass binaries and for several combinations of the individual spins. A remarkable EOB/NR agreement around such zero is found for these modes. The new waveform, and radiation reaction, prompts a new NR-calibration of the spinning sector of the model, done with only 32 datasets. The maximum $(2, 2)$ EOB/NR unfaithfulness \bar{F} with Advanced LIGO noise against the SXS catalog (~ 595 datasets) is always below 0.5% for binaries with total mass M as $10M_{\odot} \leq M \leq 200M_{\odot}$, except for a single outlier with $\max(\bar{F}) \sim 0.85\%$. When $(2, 1)$, $(3, 3)$ and $(4, 4)$ modes are included, one finds an excellent EOB/NR agreement up to $M \sim 120M_{\odot}$, above which the performance degrades slightly and moves above 3%. We also point out that the EOB dynamics may develop unphysical features for large, anti-aligned, spins and this may impact the correct construction of the $(2, 1)$ mode in some corners of the parameter space.

I. INTRODUCTION

The recent observation made by LIGO [1] and Virgo [2] of gravitational wave (GW) signals from twelve coalescing compact binaries marked the beginning of the era of gravitational wave astronomy. Of these detections, ten were associated to coalescing binary black holes (BBHs) [3–8] and two to a binary neutron star (BNS) [9, 10].

Up to recent times, gravitational waveform models used on LIGO and Virgo data only incorporated the dominant $(\ell = 2, m = 2)$ mode. This may be sufficient when the binary system is highly symmetric (e.g. nearly equal masses and nearly equal spins), but for binaries when one object is more massive than the other, or when the spins are very different, modeling the subdominant multipoles becomes an absolute necessity to avoid potential biases in the parameters [11, 12]. Similarly, at large inclinations, the modeling of gravitational wave modes beyond the dominant mode becomes increasingly important as higher modes are geometrically suppressed in the face-on/off limit. For this reason, there were recent ef-

forts in building waveform models that incorporate the subdominant modes. This was the case for phenomenological models, both in the spinning [13] or nonspinning case [14], or for effective-one-body (EOB) models [15] for spin aligned black hole binaries. In addition, Ref. [16] took advantage of a huge number of high-quality numerical relativity simulations from the SXS collaboration to construct a numerical relativity (NR) surrogate model with as many modes as possible (also including the $m = 0$ ones).

Within the effective-one-body framework [17–21] for coalescing black-hole binaries, the `SEOBNRv4HM` model introduced in Ref. [15] is the higher-mode version of the `SEOBNRv4` [22] spin-aligned model, calibrated to NR simulations, while `SEOBNRv4HMP` is its precessing version [23] and represents current state of the art. Alternatively to `SEOBNRv4`, a different spin-aligned EOB model, informed by NR simulations, is `TEOBResumS`. This model was introduced in [24], and used to independently infer the parameters of GW150914 [3]. Although this waveform model is limited to the $\ell = m = 2$ dominant mode, is publicly available either as a stand-alone C code based on the

GSL library or through the LIGO LALSuite [25] library. One of the advantages of this model is that it implements the description of the inspiral dynamics based on the (high-order) post-adiabatic (PA) approximation [26–28]. This allows one to generate long-inspiral waveforms so efficiently to be of direct use for parameter estimation purposes (see also Ref. [29] where the same approach is applied to the SEOBNRv4 Hamiltonian).

Recently, in a companion paper [30], hereafter Paper I, the nonspinning sector of `TEOBResumS`, was augmented with all subdominant waveform modes, completed through merger and ringdown, up to $\ell = m = 5$ included. This defined the `TEOBiResumMultipoles` model. In doing so, the EOB orbital interaction potential was improved thanks to a more stringent comparison with state-of-the-art NR simulations with small uncertainties. This led us to construct a multipolar model with EOB/NR unfaithfulness at most of the order of 2% (and typically well below 1%) for total mass up to $200M_\odot$ and mass ratio in the range $1 \leq q \leq 10$. It was also possible to verify that the model performs excellently up to $q = 18$, that is the NR dataset with the largest mass ratio currently available to us.

The purpose of the present work is to generalize the results of Paper I to the case of spin-aligned black-hole binaries. To improve the robustness of the multipolar waveform amplitudes towards merger, we build upon Refs. [31, 32], implementing the corresponding orbital factorization and resummation paradigm, though limited to the $m = \text{odd}$ waveform modes. Together with the changes in the nonspinning part of the dynamics discussed in Paper I, this led us to a new determination of the next-to-next-to-next-to-leading (NNNLO) spin-orbit effective parameter c_3 introduced long ago [33, 34]. The construction of the multipolar waveform around the amplitude peak of each multipole (e.g. around merger), of the next-to-quasi-circular (NQC) corrections and of the postpeak-ringdown phase follows the procedure discussed, multipole by multipole, for the nonspinning case in Paper I. The only difference is that some of the NR-informed fits incorporate now a suitable spin-dependence. The reader should be aware that this paper stems from Refs. [24, 31, 33–37] and it is essentially the follow up of Refs. [24, 30]. As such, it adopts the same notations and conventions. For this reason, we shall assume the reader to be familiar with the notation and language of those papers, that might not be reintroduced if not absolutely necessary.

The paper is organized as follows. In Sec. II we review the elements of the EOB dynamics that remained unchanged with respect to [24] and Paper I; we discuss the structure of the new multipolar waveform and the related new determination of c_3 . Section III summarizes describes in details the numerical waveforms employed in this paper (either to inform the model or to check it), focusing in particular on an estimate of their uncertainty. Section IV probes the (2, 2) mode all over the current release of the SXS catalog [38]. Section V focuses on the

behavior of higher multipolar modes, highlighting several aspects related to their accurate modelization. In particular, it is pointed out, and explained, the peculiar behavior of some $m = 1$ modes. The important EOB/NR unfaithfulness computations with higher modes are also performed there. Our concluding remarks are then collected in Sec. VI. The bulk of the text is complemented by several Appendixes. Appendix A discusses in detail the nonspinning limit of the model; Appendix B highlights a few systematics in the SXS waveform data that are relevant for higher modes; Appendix C reports all the NR-informed fits that are needed to accurately build the merger and ringdown part of the multipolar waveform.

If not otherwise specified, we use natural units with $c = G = 1$. Our notations are as follows: we denote with (m_1, m_2) the individual masses, while the mass ratio is $q \equiv m_1/m_2 \geq 1$. The total mass and symmetric mass ratio are then $M \equiv m_1 + m_2$ and $\nu = m_1 m_2 / M$. We also use the mass fractions $X_{1,2} \equiv m_{1,2} / M$ and $X_{12} \equiv X_1 - X_2 = \sqrt{1 - 4\nu}$. We address with (S_1, S_2) the individual, dimensionful, spin components along the direction of the orbital angular momentum. The dimensionless spin variables are denoted as $\chi_{1,2} \equiv S_{1,2} / (m_{1,2})^2$. We also use $\tilde{a}_{1,2} \equiv X_{1,2} \chi_{1,2}$, the effective spin $\tilde{a}_0 = \tilde{a}_1 - \tilde{a}_2$ and $\tilde{a}_{12} \equiv \tilde{a}_1 - \tilde{a}_2$.

II. THE MODEL: RELATIVE DYNAMICS AND MULTIPOLAR WAVEFORM

In this Section we collect the analytical elements of `TEOBiResumSSM` that change with respect to the original implementation of `TEOBResumS` of [24] or that stem from results of Paper I. The modifications regard all building blocks of the model: the Hamiltonian, the inspiral, EOB-resummed, waveform as well as the merger-ringdown part. However, the structure of the Hamiltonian is precisely the same of `TEOBResumS`: there is thus no need to describe it here in detail and we address the reader to Sec. II of Ref. [24]. The modifications are limited to the NR-informed effective 5PN coefficient $a_6^c(\nu)$ (that coincides with the function determined in Paper I) as well as the effective NNNLO spin-orbit parameter $c_3(\nu, \tilde{a}_1, \tilde{a}_2)$. This one needs to be redetermined, by phasing comparison with NR simulations, because of both the new $a_6^c(\nu)$, that has changed with respect to Ref. [24], and the new analytical choice for the factorized (and resummed) multipolar waveform taken from Ref. [32]. In addition, we also present here a new, spin-dependent, description of the multipolar merger and ringdown waveform, that is based on fits informed by NR simulations. These fits incorporate some, but not all, spin dependence for all modes up to $\ell = m = 5$, as we detail in Appendix C. We start by discussing the structure of the resummed waveform.

TABLE I. Resummation choices used to build our multipolar EOB waveform. The bar denotes resummation using the inverse Taylor expansion, as described by Eq. (5) of Ref. [31]. The PN-order should be intended relative to the leading-order term and also indicates the order of the additional (spinning) test-particle terms. For example, 3.5PN means that we take a polynomial of the form $1 + x^{3/2} + x^2 + x^{5/2} + \dots + x^{7/2}$, with the known ν dependence in the coefficients. Instead, 1.5^{+1} PN means that we add to the ν -dependent 1.5PN-accurate polynomial an additional term proportional to $x^{5/2}$ obtained by suitably incorporating spinning p article terms as illustrated in Sec. VB of Ref. [32]. We denote Padé resummation by P_d^n , where $N = n + d$ is the PN order.

(ℓ, m)	Resummation choices		Relative PN order	
	orbital	spin	orbital	spin
(2, 2)	$P_0^5[\rho_{22}^{\text{orb}}]$	$T[\rho_{22}^{\text{S}}]$	3^{+2} PN	3.5PN without NNLO SO term
(2, 1)	$P_1^5[\rho_{21}]$	$\hat{f}_{21}^{\text{S}} = X_{12}\overline{\hat{f}_{21}^{\text{S}(0)}} - \frac{3}{2}\tilde{a}_{12}x^{1/2}\overline{\hat{f}_{21}^{\text{S}(1)}}$	3^{+3} PN	2.5PN
(3, 3)	$P_2^4[\rho_{33}]$	$\hat{f}_{33}^{\text{S}} = X_{12}\overline{\hat{f}_{33}^{\text{S}(0)}} + \left(-\frac{1}{4} + \frac{5}{2}\nu\right)\tilde{a}_{12}x^{3/2}\hat{f}_{33}^{\text{S}(1)}$	3^{+3} PN	2.5PN
(3, 2)	$P_2^4[\rho_{32}]$	$T[\rho_{32}^{\text{S}}]$	2^{+2} PN	1.5^{+1} PN (SO only)
(3, 1)	$P_2^3[\rho_{31}^{\text{orb}}]$	$\hat{f}_{31}^{\text{S}} = X_{12}\overline{\hat{f}_{31}^{\text{S}(0)}} + \left(-\frac{9}{4} + \frac{13}{2}\nu\right)\tilde{a}_{12}x^{3/2}\hat{f}_{31}^{\text{S}(1)}$	3^{+2} PN	2.5PN
(4, 4)	$P_0^6[\rho_{44}^{\text{orb}}]$	$T[\rho_{44}^{\text{S}}]$	2^{+4} PN	1.5^{+2} PN (SO only)
(4, 3)	$P_2^4[\rho_{43}^{\text{orb}}]$	$\hat{f}_{43}^{\text{S}} = X_{12}\overline{\hat{f}_{43}^{\text{S}(0)}} - \frac{5}{4}\tilde{a}_{12}x^{1/2}$	1^{+5} PN	0.5PN (SO only)
(4, 2)	$P_0^6[\rho_{42}^{\text{orb}}]$	$T[\rho_{42}^{\text{S}}]$	2^{+4} PN	1.5^{+3} PN (SO only)
(4, 1)	$P_2^4[\rho_{41}^{\text{orb}}]$	$\hat{f}_{41}^{\text{S}} = X_{12}\overline{\hat{f}_{41}^{\text{S}(0)}} - \frac{5}{4}\tilde{a}_{12}x^{1/2}$	1^{+5} PN	0.5PN (SO only)
(5, 5)	$P_0^6[\rho_{55}^{\text{orb}}]$	$\hat{f}_{55}^{\text{S}} = X_{12}\overline{\hat{f}_{55}^{\text{S}(0)}} + 10\nu\frac{(1-3\nu)}{3-6\nu}\tilde{a}_{12}x^{3/2}$	1^{+5} PN	2PN

A. Inspiral multipolar waveform

The waveform amplitudes we use here incorporate several factorization and resummation procedures that have been discussed in previous literature [31, 32, 39, 40]. One should be warned that there are not ubiquitous recipes for what concerns the choice of resummation and/or the multipolar order to use: each multipolar amplitude can, in principle, be treated separately from the others. In practice, following Paper I, we attempt to comply at the idea of using 6PN-accurate hybrid orbital (i.e. nonspinning) amplitudes that are, whenever possible, resummed using Padé approximants. By “hybrid” we mean that the ν -dependent terms, analytically known up to 3PN accuracy, are augmented by test-particle terms up to getting a relative 6PN order in all the residual waveform amplitudes. The spin sector takes advantage of some of, but not all, the new PN information at next-to-next-to-leading-order (NNLO) that was recently presented in Ref. [15] adapting (yet unpublished) results of S. Marsat and A. Bohé. Practically all the structure of the waveform was discussed in Sec. IIIB, IIIC and IIID and of

Paper I. Since we are adopting the same notation and nomenclature introduced there, it is not worth to repeat it here. We only recall that the acronym NQC stands for “next-to-quasi-circular” and that $f_{\ell m}$ ’s or $\rho_{\ell m} \equiv (f_{\ell m})^{1/\ell}$ functions are the residual waveform amplitudes. For resumming the $m = \text{odd}$ mode waveform amplitudes we implement the orbital-factorization and resummation scheme of Ref. [32]. In brief, following the notation of this latter reference, our analytical choices for the waveform amplitudes are listed in Table I. We give below more details, discussing explicitly, and separately, the orbital and spin sectors.

1. Orbital sector

All ν -dependent terms in the multipolar amplitudes up to $\ell = 6$ are augmented with test-particle terms up to relative (hybrid) order 6PN *except* for the (2, 2) and (3, 1) modes, that rely on 3^{+2} PN information, consistently with previous work. For most of the modes, such 6PN-accurate, hybridized, amplitudes are additionally

Padé resummed consistently with the choice made in the extreme-mass-ratio limit in Ref. [32]. Note however that some multipoles actually behave *better* (when compared with test-mass numerical data) when they are left in non-resummed form. Table I lists, in the second column, the analytical representation chosen for the orbital factors up to $\ell = m = 5$. We address the Padé approximant of order (n, d) with the usual notation P_d^n , where n is the polynomial order of the numerator and d the one of the denominator. For notational consistency, we also indicate with P_0^n the Taylor-expanded form of the functions. The subdominant modes that do not contain spin information are not reported in the table. The $(5, 1)$, $(6, 1)$, $\ell = 7$ and $\ell = 8$ modes are kept in Taylor-expanded form at (global) 3^{+2} PN order for simplicity, consistently with previous work. All other $\rho_{\ell m}^{\text{orb}}$'s with $\ell = 5$ and $\ell = 6$ are resummed as $P_2^4(\rho_{\ell m}^{\text{orb}})$ approximants.

2. Spin sector

The spin-dependent terms in the waveform amplitudes are incorporated only in those multipoles where the ν -dependence beyond the leading order is analytically known, i.e. up to $\ell = m = 5$, as illustrated in Table I. For some modes, the ν -dependent information is augmented with spinning-particle terms, according to the hybridization procedure discussed in Ref. [32]. Note that the analytical resummation of the residual waveform amplitudes to improve their robustness in the strong-field, fast-velocity regime when $m = \text{even}$ is not the same as when $m = \text{odd}$. For the $m = \text{even}$ modes, the residual amplitudes are written as

$$P_d^n [\rho_{\ell m}^{\text{orb}}] + \rho_{\ell m}^{\text{S}}, \quad (1)$$

where we explicitly indicate the fact that the orbital part is Padé resummed (including in this nomenclature also the plain Taylor-expansion) according to Table I. By contrast, the spin-dependent part is kept in Taylor-expanded form, with the (relative) PN order given in Table I. Here, the notation $T[\rho_{\ell m}^{\text{S}}]$ is an explicit reminder that we are using the $\rho_{\ell m}^{\text{S}}$ in Taylor-expanded form. The amount of analytical information used in each mode is listed in the fifth column of the table. First of all, note that we *do not* include the NNLO spin-orbit term in ρ_{22}^{S} that was recently computed and is part of either SEOBNRv4 [22] and SEOBNRv4HM [15]. As it was pointed out already in Ref. [31], this term has a large impact on the EOB waveform towards merger for large, positive, spins, so that the EOB/NR difference is *larger* with this term than without it (see Fig. 6 of [31]). By contrast, the NLO-accurate amplitude alone already delivers an excellent representation of the corresponding NR amplitude and thus gives a more robust starting point for the action of the NQC factor. We do, however, include the LO cubic-in-spin term in ρ_{22}^{S} . Browsing the fifth column of Table I the notation adopted indicates that the ν -dependent terms

in $(\rho_{32}^{\text{S}}, \rho_{44}^{\text{S}}, \rho_{42}^{\text{S}})$ were *hybridized* with some of the higher-order, spin-orbit, terms obtained in the limit of a spinning particle on a Schwarzschild black hole in Ref. [41]. The rationale behind such hybridization procedure is discussed in Sec. VB of Ref. [32] and allows one to incorporate some of the leading-in- ν -dependence by suitably “dressing” the $\nu = 0$ information. One finds that the additional terms are such to increase the EOB/NR waveform amplitude agreement towards merger in a natural way. To be explicit, we have

$$\rho_{32}^{\text{S}} = c_{32}^{\text{SO}_{\text{lo}}} x^{1/2} + c_{32}^{\text{SO}_{\text{nio}}} x^{3/2} + c_{32}^{\text{SO}_{\text{nnlo}}} x^{5/2}, \quad (2)$$

where $(c_{32}^{\text{SO}_{\text{lo}}}, c_{32}^{\text{SO}_{\text{nio}}})$ are the usual known terms with the full ν dependence (see e.g. [32] for their explicit form), while

$$c_{32}^{\text{SO}_{\text{nnlo}}} = -\frac{2571199}{1924560} \tilde{a}_0 - \frac{1844993}{1924560} \tilde{a}_{12} X_{12}, \quad (3)$$

that reduces to the known spinning test-particle terms when $\nu \rightarrow 0$. Similarly, ρ_{44}^{S} reads

$$\rho_{44}^{\text{S}} = c_{44}^{\text{SO}_{\text{lo}}} x^{3/2} + c_{44}^{\text{SO}_{\text{nio}}} x^{5/2} + c_{44}^{\text{SO}_{\text{nnlo}}} x^{7/2}, \quad (4)$$

where

$$c_{44}^{\text{SO}_{\text{nio}}} = -\frac{199}{550} \tilde{a}_0 - \frac{491}{550} \tilde{a}_{12} X_{12}, \quad (5)$$

$$c_{44}^{\text{SO}_{\text{nnlo}}} = \frac{527001653}{264264000} \tilde{a}_0 + \frac{3208967}{264264000} \tilde{a}_{12} X_{12}, \quad (6)$$

For ρ_{42}^{S} we have

$$\rho_{42}^{\text{S}} = c_{42}^{\text{SO}_{\text{lo}}} x^{3/2} + c_{42}^{\text{SO}_{\text{nio}}} x^{5/2} + c_{42}^{\text{SO}_{\text{nnlo}}} x^{7/2} + c_{42}^{\text{SO}_{\text{nnnlo}}} x^{9/2}, \quad (7)$$

where the ν -dressed spinning particle coefficients read

$$c_{42}^{\text{SO}_{\text{nio}}} = -\frac{219}{550} \tilde{a}_0 + \frac{92}{275} \tilde{a}_{12} X_{12}, \quad (8)$$

$$c_{42}^{\text{SO}_{\text{nnlo}}} = -\frac{329051729}{264264000} \tilde{a}_0 + \frac{169512229}{264264000} \tilde{a}_{12} X_{12}, \quad (9)$$

$$c_{42}^{\text{SO}_{\text{nnnlo}}} = -\left(\frac{32079746680643}{16482145680000} + \frac{17581}{51975} \text{eulerlog}(x, 2) \right) \tilde{a}_0 - \left(\frac{28943192016227}{16482145680000} - \frac{10697}{51975} \text{eulerlog}(x, 2) \right) \tilde{a}_{12} X_{12}. \quad (10)$$

For the $m = \text{odd}$ modes, we apply in full the factorization of the orbital term and subsequent resummation of the spin factor with its inverse Taylor representation as illustrated in Ref. [32]. Recalling the notation therein, each m -odd waveform mode is written as

$$h_{\ell m}^{(\epsilon)} = h_{\ell m}^{N,(\epsilon)'} \tilde{h}_{\ell m}^{(\epsilon)}, \quad (11)$$

where $h_{\ell m}^{N,(\epsilon)'}$ is the usual Newtonian prefactor [39] with the overall factor X_{12} factorized out, while

$$\tilde{h}_{\ell m}^{(\epsilon)} \equiv X_{12} \hat{h}_{\ell m}^{(\epsilon)}, \quad (12)$$

and $\hat{h}_{\ell m}^{(\epsilon)}$ is the usual relativistic correction [39]. The m -odd relativistic waveform correction is then factorized as

$$\tilde{h}_{\ell m}^{(\epsilon)} = \hat{S}_{\text{eff}}^{(\epsilon)} \hat{h}_{\ell m}^{\text{tail}} e^{i\delta_{\ell m}} [P_d^n(\rho_{\ell m}^{\text{orb}})]^\ell \hat{f}_{\ell m}^{\text{S}}, \quad (13)$$

where $(\hat{h}_{\ell m}^{\text{tail}}, \delta_{\ell m})$ are the usual, well known, tail factor and residual phase correction [39]. The spin-dependent $\hat{f}_{\ell m}^{\text{S}}$ functions that we use are summarized in Table I. The same table also lists the Padé approximants $P_d^n[\rho_{\ell m}^{\text{orb}}]$ adopted for the orbital factors. For the spin factors, we take advantage of the new NNLO results of Ref. [15], in particular those concerning the $\ell = m = 5$ mode. This multipole is also resummed consistently with the others. In particular, it also includes the 2PN-accurate (or relative LO) spin-square term. The inverse-resummed

factor $\overline{\hat{f}_{55}^{\text{S}(0)}}$ explicitly reads

$$\overline{\hat{f}_{55}^{\text{S}(0)}} = \left(1 + \frac{10}{3} \tilde{a}_0 x^{3/2} - \frac{5}{2} \tilde{a}_0^2 x^2 \right)^{-1}. \quad (14)$$

The global structure of the spin factors is illustrated in Table I and we do not discuss here any further as it is a straightforward application of the procedure of Ref. [32] once modified with the new PN terms published in Ref. [15] and the spinning-particle terms of Ref. [41].

3. Residual phase corrections $\delta_{\ell m}$

Let us finally detail the expression of the $\delta_{\ell m}$ we use. Following Ref. [42], we mostly use them in Padé resummed form, augmenting, for some modes, the 3.5PN, ν -dependent terms with the next, 4.5PN-accurate, contribution in the test-particle limit [43]. In addition, we only rely on *nonspinning* information, although spin-dependent terms are available [15]. Explicitly, the expressions we use read

$$\delta_{22} = \frac{7}{3} y^{\frac{3}{2}} \frac{808920\nu\pi\sqrt{y} + 137388\pi^2 y + 35\nu^2(136080 + (154975 - 1359276\nu)y)}{808920\nu\pi\sqrt{y} + 137388\pi^2 y + 35\nu^2(136080 + (154975 + 40404\nu)y)}, \quad (15)$$

$$\delta_{21} = \frac{2}{3} y^{\frac{3}{2}} \frac{5992\pi\sqrt{y} + 2465\nu(28 - 493\nu y)}{69020\nu + 5992\pi\sqrt{y}}, \quad (16)$$

$$\delta_{33} = \frac{13}{10} y^{\frac{3}{2}} \frac{1 + \frac{94770\pi}{566279\nu}\sqrt{y}}{1 + \frac{94770\pi}{566279\nu}\sqrt{y} + \frac{80897}{3159}\nu y}, \quad (17)$$

$$\delta_{32} = \frac{10 + 33\nu}{15(1 - 3\nu)} y^{\frac{3}{2}} \frac{1}{1 - \frac{260(1-3\nu)}{7(10+33\nu)}\pi y^{\frac{3}{2}} + \frac{1}{(10+33\nu)^2} \left(\frac{91120}{27} + \frac{9112}{9}\nu - \frac{100232}{3}\nu^2 + \frac{130000}{147}\pi^2 - \frac{412880}{49}\nu\pi^2 + \frac{848640}{49}\nu^2\pi^2 \right) y^3}, \quad (18)$$

$$\delta_{31} = \frac{13}{30} y^{\frac{3}{2}} \frac{4641\nu + 1690\pi\sqrt{y}}{4641\nu + 1690\pi\sqrt{y} + 18207\nu^2 y}, \quad (19)$$

$$\delta_{44} = \frac{112 + 219\nu}{120(1 - 3\nu)} y^{\frac{3}{2}} \frac{1}{1 - \frac{201088(1-3\nu)}{231(112+219\nu)}\pi y^{\frac{3}{2}} - \frac{1-3\nu}{(112+219\nu)^2} \left(\frac{49409024}{25} + \frac{96612288}{25}\nu + \frac{8854306816}{17787}\pi^2 - \frac{49478908928}{17787}\nu\pi^2 \right) y^3}, \quad (20)$$

$$\delta_{43} = \frac{486 + 4961\nu}{810(1 - 2\nu)} y^{\frac{3}{2}} \left[1 - \frac{254502(1 - 2\nu)}{77(486 + 4961\nu)}\pi y^{\frac{3}{2}} + \frac{1}{(486 + 4961\nu)^2} \left(\frac{122106771}{5} + \frac{2004460533}{10}\nu + \right. \right. \\ \left. \left. - \frac{2492887617}{5}\nu^2 + \frac{45723320316}{5929}\pi^2 - \frac{415427177628}{5929}\nu\pi^2 + \frac{647961073992}{5929}\nu^2\pi^2 \right) y^3 \right]^{-1}, \quad (21)$$

$$\delta_{42} = \frac{7(1 + 6\nu)}{15(1 - 3\nu)} y^{\frac{3}{2}} \frac{1}{1 - \frac{6284(1-3\nu)}{1617(1+6\nu)}\pi y^{\frac{3}{2}} + \frac{1-3\nu}{(1+6\nu)^2} \left(\frac{6893}{175} + \frac{41358}{175}\nu + \frac{8646784}{871563}\pi^2 - \frac{22195088}{290521}\nu\pi^2 \right) y^3}, \quad (22)$$

$$\delta_{41} = \frac{2 + 507\nu}{10(1 - 2\nu)} y^{\frac{3}{2}} + \frac{1571}{3465}\pi^3 y^3, \quad (23)$$

$$\delta_{55} = \frac{96875 + 857528\nu}{131250(1 - 2\nu)} y^{\frac{3}{2}}, \quad (24)$$

where $y = \hat{H}_{\text{EOB}}\Omega$, with \hat{H}_{EOB} and Ω being the energy and orbital frequency of the binary system respectively. For completeness, let us also list the original Taylor expanded functions that are then resummed using the Padé approximants explicitly written above.

$$\delta_{22}^{\text{Taylor}} = \frac{7}{3}y^{\frac{3}{2}} - 24\nu y^{\frac{5}{2}} + \frac{428}{105}\pi y^3 + \left(\frac{30995}{42} + \frac{962}{5}\nu\right)\frac{\nu}{27}y^{\frac{7}{2}}, \quad (25)$$

$$\delta_{21}^{\text{Taylor}} = \frac{2}{3}y^{\frac{3}{2}} - \frac{493}{42}\nu y^{\frac{5}{2}} + \frac{107}{105}\pi y^3, \quad (26)$$

$$\delta_{33}^{\text{Taylor}} = \frac{13}{10}y^{\frac{3}{2}} - \frac{80897}{2430}\nu y^{\frac{5}{2}} + \frac{39}{7}\pi y^3, \quad (27)$$

$$\delta_{31}^{\text{Taylor}} = \frac{13}{30}y^{\frac{3}{2}} - \frac{17}{10}\nu y^{\frac{5}{2}} + \frac{13}{21}\pi y^3, \quad (28)$$

$$\delta_{32}^{\text{Taylor}} = \frac{10 + 33\nu}{15(1 - 3\nu)}y^{\frac{3}{2}} + \frac{52}{21}\pi y^3 + \left(\frac{208}{63}\pi^2 - \frac{9112}{405}\right)y^{9/2}, \quad (29)$$

$$\delta_{44}^{\text{Taylor}} = \frac{112 + 219\nu}{120(1 - 3\nu)}y^{\frac{3}{2}} + \frac{25136}{3465}\pi y^3 + \left(\frac{201088}{10395}\pi^2 - \frac{55144}{375}\right)y^{9/2}, \quad (30)$$

$$\delta_{43}^{\text{Taylor}} = \frac{486 + 4961\nu}{810(1 - 2\nu)}y^{3/2} + \frac{1571}{385}\pi y^3 + \left(-\frac{18611}{300} + \frac{3142}{385}\pi^2\right)y^{9/2}, \quad (31)$$

$$\delta_{42}^{\text{Taylor}} = \frac{7(1 + 6\nu)}{15(1 - 3\nu)}y^{3/2} + \frac{6284}{3465}\pi y^3 + \left(\frac{25136}{10395}\pi^2 - \frac{6893}{375}\right)y^{9/2}. \quad (32)$$

Comparing with Appendix D of Ref. [42], we are here explicitly using 4.5PN terms in some of the higher modes, since we found that they improve the EOB/NR frequency agreement close to merger. In practice, after factorizing the leading contribution following [42], the approximants we use for each mode are: $\delta_{22} \rightarrow P_2^2$; $\delta_{21} \rightarrow P_1^2$; $\delta_{33} \rightarrow P_2^1$; $\delta_{32} \rightarrow P_2^0$; $\delta_{31} \rightarrow P_2^1$; $\delta_{44} \rightarrow P_2^0$ and $\delta_{43} \rightarrow P_2^0$.

B. Multipolar peak, ringdown and next-to-quasi-circular corrections

The modelization of the peak and postpeak waveform multipole by multipole is done following precisely the same procedure adopted in the nonspinning case, but incorporating spin dependence (whenever possible) in all fits. As we detail in Appendix C, in practice we include: (i) complete spin-dependence for what concerns peak quantities and postpeak fits in all $\ell = m$ modes up to $\ell = 5$; (ii) modes like (2, 1), (3, 2), (4, 3) and (4, 2) include spin dependence for peak frequency and amplitude, but they adopt the simpler nonspinning fits

for the parameters entering the postpeak waveform description; (iii) the (3, 1) and (4, 1) mode only rely on nonspinning information. The values at the NQC determination points are either obtained with dedicated fits of the corresponding NR quantities, or directly from the postpeak behavior. All considered, this approach allows one to obtain a rather robust description of the ringdown waveform all over the parameter space.

C. NR-informed EOB functions: a_6^c and c_3

Finally, we discuss the NR-informed functions that enter the EOB dynamics. For $a_6^c(\nu)$, we use the function determined in Paper I. Note that this was obtained using the Padé resummed $P_2^4[\rho_{22}^{\text{orb}}]$ description of the residual $\ell = m = 2$ waveform amplitude hybridized with test-particle terms up to 6PN. For simplicity, we adopt it here *even if* we are here using ρ_{22}^{orb} at 3⁺ PN accuracy. The differences in the dynamics, at the nonspinning level, are consistent with the NR uncertainty, so it is not worth to proceed with a new, more consistent, determination of this function. The expression adopted from Paper I is

$$a_6^c = n_0 \frac{1 + n_1\nu + n_2\nu^2 + n_3\nu^3}{1 + d_1\nu}, \quad (33)$$

where

$$n_0 = 5.9951, \quad (34)$$

$$n_1 = -34.4844, \quad (35)$$

$$n_2 = -79.2997, \quad (36)$$

$$n_3 = 713.4451, \quad (37)$$

$$d_1 = -3.167. \quad (38)$$

This, together with the new analytical description of the spin-sector of the waveform (and radiation reaction) calls for a new determination of c_3 . This is obtained precisely following Sec. IIB.2 of Ref. [24], i.e. by determining the good values of c_3 such that the EOB/NR dephasing is within the nominal NR phase uncertainty at NR merger. This is done using 32 NR datasets, 30 from SXS and 2 from the BAM code. The configurations used are listed in Table II, together with the value of c_3 that assures an EOB/NR phasing at merger that is smaller than (or comparable with) the nominal numerical uncertainty (see [24]). Note also that these values are such to assure that the EOB frequency evolution towards merger is correctly reproducing the corresponding NR one. The data of Table II are fitted with a global function as $c_3(\nu, \tilde{a}_0, \tilde{a}_{12})$ that is actually simplified with respect to previous work. The fit template reads

$$c_3(\tilde{a}_1, \tilde{a}_2, \nu) = p_0 \frac{1 + n_1\tilde{a}_0 + n_2\tilde{a}_0^2 + n_3\tilde{a}_0^3 + n_4\tilde{a}_0^4}{1 + d_1\tilde{a}_0} + p_1\tilde{a}_0\nu\sqrt{1 - 4\nu} + p_2(\tilde{a}_1 - \tilde{a}_2)\nu^2, \quad (39)$$

TABLE II. Binary configurations, first-guess values of c_3 used to inform the global interpolating fit given in Eq. (39), and the corresponding c_3^{fit} values.

#	ID	(q, χ_1, χ_2)	$c_3^{\text{first guess}}$	c_3^{fit}
1	SXS:BBH:0156	(1, -0.95, -0.95)	88	87.87
2	SXS:BBH:0159	(1, -0.90, -0.90)	85.5	85.54
3	SXS:BBH:0154	(1, -0.80, -0.80)	81	80.90
4	SXS:BBH:0215	(1, -0.60, -0.60)	71.5	71.72
5	SXS:BBH:0150	(1, +0.20, +0.20)	38.0	36.92
6	SXS:BBH:0228	(1, +0.60, +0.60)	22.0	21.94
7	SXS:BBH:0230	(1, +0.80, +0.80)	15.5	16.25
8	SXS:BBH:0153	(1, +0.85, +0.85)	14.5	15.25
9	SXS:BBH:0160	(1, +0.90, +0.90)	14.9	14.53
10	SXS:BBH:0157	(1, +0.95, +0.95)	14.3	14.20
11	SXS:BBH:0177	(1, +0.99, +0.99)	14.2	14.32
12	SXS:BBH:0004	(1, -0.50, 0)	54.5	56.61
13	SXS:BBH:0231	(1, +0.90, 0)	27.0	26.18
14	SXS:BBH:0232	(1, +0.90, +0.50)	19.0	18.38
15	SXS:BBH:0005	(1, +0.50, 0)	34.3	34.34
16	SXS:BBH:0016	(1.5, -0.50, 0)	57.0	58.19
17	SXS:BBH:0255	(2, +0.60, 0)	29.0	29.75
18	SXS:BBH:0256	(2, +0.60, +0.60)	22.8	23.68
19	SXS:BBH:0257	(2, +0.85, +0.85)	15.7	17.73
20	SXS:BBH:0036	(3, -0.50, 0)	60.0	60.39
21	SXS:BBH:0267	(3, -0.50, -0.50)	69.5	65.28
22	SXS:BBH:0174	(3, +0.50, 0)	30.0	31.20
23	SXS:BBH:0286	(3, +0.50, +0.50)	26.0	27.28
24	SXS:BBH:0291	(3, +0.60, +0.60)	23.4	24.22
25	SXS:BBH:0293	(3, +0.85, +0.85)	16.2	18.48
26	SXS:BBH:0060	(5, -0.50, 0)	62.0	61.91
27	SXS:BBH:0110	(5, +0.50, 0)	31.0	29.97
28	SXS:BBH:1375	(8, -0.90, 0)	64.0	78.27
29	SXS:BBH:0064	(8, -0.50, 0)	57.0	63.23
30	SXS:BBH:0065	(8, +0.50, 0)	28.5	28.86
31	BAM	(8, +0.80, 0)	24.5	20.85
32	BAM	(8, +0.85, +0.85)	16.3	18.11

where the parameters are

$$p_0 = 45.235903, \quad (40)$$

$$n_1 = -1.688708, \quad (41)$$

$$n_2 = 0.787959, \quad (42)$$

$$n_3 = -0.018080, \quad (43)$$

$$n_4 = -0.001906, \quad (44)$$

$$d_1 = -0.751479, \quad (45)$$

$$p_1 = 47.3756, \quad (46)$$

$$p_2 = -36.1964. \quad (47)$$

Figure 1 highlights that the span of the “best” (first-guess) values of c_3 is rather limited (especially for pos-

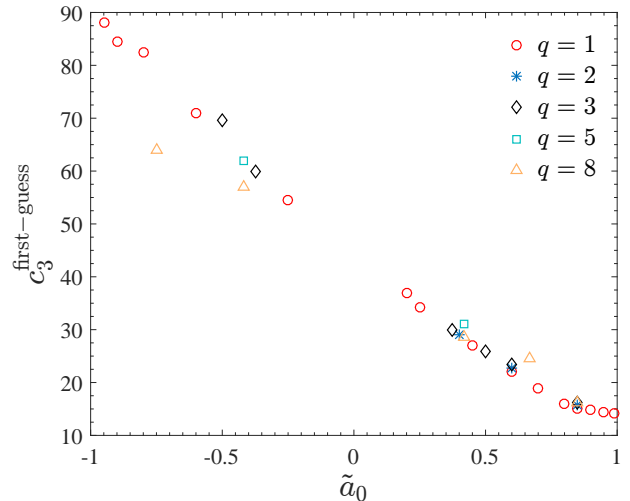


FIG. 1. The first-guess c_3 values of Table II versus the spin variable $\tilde{a}_0 \equiv S_1/(m_1 M) + S_2/(m_2 M)$. The unequal-spin and unequal-mass points can be essentially seen as a correction to the equal-mass, equal-spin values.

itively aligned spins) around the equal-mass, equal-spin case. At a practical level, this eases up the fitting procedure, that, following Ref. [24], is performed in two steps. First, one fits the equal-mass, equal-spin data with a quasi-linear function of $\tilde{a}_0 = \tilde{a}_1 + \tilde{a}_2$ with $\tilde{a}_1 = \tilde{a}_2$. This delivers the six parameters $(p_0, n_1, n_2, n_3, n_4, d_1)$. Note that the analytical structure of the fitting function was chosen in order to accurately capture the nonlinear behavior of c_3 for $\tilde{a}_0 \rightarrow 1$. In the second step one subtracts this fit, computed for the unequal-mass, unequal-spin data, from the corresponding $c_3^{\text{first-guess}}$ values and fits the residual. This gives the parameters (p_1, p_2) . The novelty with respect to Ref. [24] is that, thanks to the new analytical improvements, one finds that the unequal-spin and unequal-mass correction can be represented, in Eq. (39), with acceptable accuracy, only with the two parameters (p_1, p_2) , as we shall illustrate quantitatively in Sec. IV, after an assessment of the accuracy of the NR waveforms at our disposal.

III. NUMERICAL RELATIVITY WAVEFORMS

A. Waveforms overview

The NR data used here were separated into two categories (see Table III). On the one hand, a set of waveforms used for the *calibration* of the postpeak and ring-down waveform; on the other hand, a set used for the *validation* of the full waveform model¹. The *postpeak-*

¹ With the exceptions of the fitting of a small set of problematic parameters. These parameters are subdominant and not well

	Parameter interval ranges		Waveform count #		$\langle N_{\text{orb}} \rangle$	$\bar{F}_{\text{NR/NR}}^{\text{LevH/LevM}}$	
	$q \equiv m_1/m_2$	$\chi_{1,2}$	total	with LevM		$\bar{F}_{\text{NR/NR}}^{\text{max}}$	$\langle \bar{F}_{\text{NR/NR}}^{\text{max}} \rangle$
<i>Calibration set</i>							
SXS	[1.0, 10.0]	0	19	18	21.98	0.075%	0.0092%
SXS	[1.0, 1.0]	[-0.95, 0.9942]	38	37	22.77	0.22%	0.020%
SXS	[1.3, 8.0]	[-0.9, 0.96]	78	73	25.09	0.11%	0.0088%
BAM	[4.0, 18.0]	0	3	–	8.11	< 0.1%	< 0.1%
	[2.0, 18.0]	[-0.85, 0.85]	16	–	11.13	< 0.1%	< 0.1%
<i>Validation set</i>							
SXS	[1.0, 10.0]	0	67	52	24.98	0.066%	0.0050%
SXS	[1.0, 1.16]	[-0.97, 0.998]	79	77	20.29	0.0093%	0.0029%
SXS	[1.17, 8.0]	[-0.9, 0.95]	309	287	20.74	0.056%	0.0052%
long SXS	[1.41, 1.83]	[-0.5, 0.5]	5	5	144.05	1.52%	0.98%

TABLE III. Numerical Relativity datasets used in this work. From left to right, the columns report: catalog origin and use; interval of parameters covered for the mass ratio q and the spins $\chi_{1,2}$; total number of waveforms in the particular sub-catalog; the number of SXS data with a second resolution LevM available; the average waveform length expressed in number of orbits, $\langle N_{\text{orb}} \rangle$, counted here between the relaxation time (i.e., after the junk radiation) and the waveform amplitude peak; the absolute maximum $\bar{F}_{\text{NR/NR}}^{\text{max}}$ and the average of the individual maxima $\langle \bar{F}_{\text{NR/NR}}^{\text{max}} \rangle$ of the unfaithfulness $\bar{F}_{\text{NR/NR}}$ computed between the highest, LevH, and second highest, LevM, resolutions. The $\bar{F}_{\text{NR/NR}}$ -uncertainties versus total mass M are depicted in Fig. 2 (spinning configurations) and Fig. 20 (nonspinning configurations).

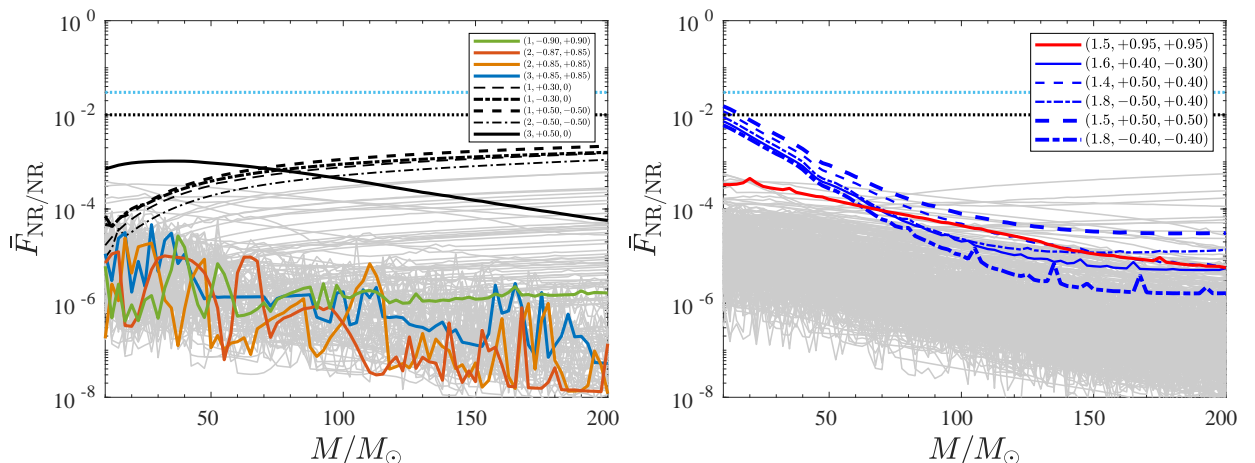


FIG. 2. NR/NR unfaithfulness uncertainty computed from Eq. (48) using the highest and next to highest resolution waveform for each SXS dataset. The left panel refers to the 116 spinning waveforms used to globally inform the model (either c_3 or ringdown) that were already available the the time of Ref. [24]. The right panel refers to the 393 spinning datasets recently released and discussed in Ref. [38]. The same quantity for nonspinning waveforms is computed in Appendix A and shown in Fig. 20.

calibration set consists of the following: (i) we enlarge the set of 23 nonspinning waveforms (19 SXS, 3 BAM, 1 test-particle) used in [30]; (ii) we use 38 SXS, spin-aligned, equal-mass waveforms with spins between $-0.95 \leq \chi_{1,2} \leq 0.9942$, see Table V; and (iii) 78 SXS

spin-aligned, unequal-mass, waveforms going up to mass ratio $q = 8$ with spins in the range $-0.9 \leq \chi_{1,2} \leq 0.96$, see Tables VI – VII, plus a single, high-quality, waveform with $(q, \chi_1, \chi_2) = (8, -0.9, 0)$; (iv) 16 BAM, spin-aligned, unequal-mass waveforms with $2 \leq q \leq 18$, encompassing two $q = 8$ waveforms with $\chi_1 = \chi_2 = \pm 0.85$ and two $q = 18$ waveforms with $\chi_1 = \pm 0.8$ and $\chi_2 = 0$, see Table VIII. All this, is complemented (v) by a sample of waveforms for a test-particle inspiralling and plunging

resolved in the NR data available in the *calibration* set. See Appendix C for further details.

on a Kerr black hole [44] with dimensionless black hole spin \hat{a} in the interval $-0.99 \leq \hat{a} \leq 0.99$. The 154 NR waveforms (excluding the test-particle waveforms) in the *Calibration* set contain an average length of 22.35 orbits, while the eccentricity never exceeds 0.004.

The *validation* set consists of 460 waveforms from the SXS catalog [45]. The waveforms span mass ratios up to $q = 8$ and spins in the range $-0.97 \leq \chi_{1,2} \leq 0.998$. This set includes 5 long waveforms with an average length of 144.05 orbits between the relaxation time and the peak of the dominant mode. The average length of the remaining waveforms is of 21.29 orbits. Eccentricity is limited to 0.001. The waveforms are listed in Tables IX – XVI. Further details on the SXS catalog can be found in Refs. [38, 46–56]. The nonspinning datasets are listed in Tables XVIII–XIX.

B. Estimating NR uncertainties for the $\ell = m = 2$ mode

The most recent update of the SXS catalog is detailed in Ref. [38]. In particular, that reference gave an estimate of the NR uncertainty due to numerical truncation error on each waveform (either precessing or nonprecessing) by computing the maximal unfaithfulness (or mismatch, see below), in flat noise, between the $\ell = m = 2$ waveform computed at highest and second highest resolutions available. This is found to be $\sim 10^{-4}$, that is then taken as a reliable estimate of the NR error. To ease the reader, we perform again here this uncertainty computation, although we (i) restrict it only to the case of nonprecessing waveform and (ii) we use the zero-detuned, high-power noise spectral density of Advanced LIGO [57]. The uncertainty of the BAM waveforms was estimated in [58] and will be referenced and summarized for the practical purposes of this work. Considering two waveforms (h_1, h_2) , the unfaithfulness is a function of the total mass M of the binary and is defined as

$$\bar{F}(M) \equiv 1 - F = 1 - \max_{t_0, \phi_0} \frac{\langle h_1, h_2 \rangle}{\|h_1\| \|h_2\|}, \quad (48)$$

where (t_0, ϕ_0) are the initial time and phase, $\|h\| \equiv \sqrt{\langle h, h \rangle}$, and the inner product between two waveforms is defined as $\langle h_1, h_2 \rangle \equiv 4\Re \int_{f_{\min}^{\text{NR}}(M)}^{\infty} \tilde{h}_1(f) \tilde{h}_2^*(f) / S_n(f) df$, where $\tilde{h}(f)$ denotes the Fourier transform of $h(t)$, $S_n(f)$ is the zero-detuned, high-power noise spectral density of Advanced LIGO [57] and $f_{\min}^{\text{NR}}(M) = \hat{f}_{\min}^{\text{NR}}/M$ is the initial frequency of the NR waveform at highest resolution, i.e. the frequency measured after the junk-radiation initial transient. Waveforms are tapered in the time-domain so as to reduce high-frequency oscillations in the corresponding Fourier transforms. Figure 2 illustrates the outcome of Eq. (48) when (h_1, h_2) are the $\ell = m = 2$ waveforms corresponding to the highest and second-highest resolution available for each SXS dataset. The left panel of Fig. 2 displays $\bar{F}(M)$ for the 116 spinning waveforms

of the *Calibration* set; in the right panel, we have the 393 spinning waveforms in the *Validation*. For almost all waveforms, the uncertainty is below 0.5%, except for the 5 long SXS (blue in the right panel of the figure) that will deserve a dedicate discussion in Sec. III C below. As a very conservative, global, estimate of the NR uncertainty, we take it to be at the 0.5% level. This choice is made to prevent over fitting of the NR-informed parameters, although we will see that very often a much better EOB/NR agreement arises naturally. Finally, note that the analysis of the quality of the SXS data is here limited to the uncertainties due to the numerical truncation error, because, as pointed out in Sec. 4 of Ref. [38], is the largely dominant one. The accuracy of the BAM waveforms was studied in Ref. [58], considering several uncertainty sources. In particular, Figs. 2 and 3 of Ref. [58] illustrate that the NR uncertainty is $\bar{F} \approx 0.1\%$ or less. Similarly to the SXS case, and to avoid overfitting and be conservative, we assume the uncertainties on all BAM waveforms at the 0.3%–0.5% level and use this as target for EOB/NR comparisons.

C. Long-inspiral Numerical Relativity waveforms

Let us comment on the 5, very-long, waveforms listed in Table XVII. All these waveforms show an inspiral of over 100 orbits before a common horizon appears². The unfaithfulness between the two highest resolution levels is shown as blue lines in Fig. 2. All dataset show a rather large \bar{F} for low masses, up to 1.5% for SXS:BBH:1415, that then decreases to the average \bar{F} around $60M_{\odot}$. This suggests that the long inspiral is more sensitive to resolution and/or other systematics effects, so that the numbers of Fig. 2 should be taken as a rather conservative uncertainty estimates.

IV. THE $\ell = m = 2$ MODE: EOB/NR UNFAITHFULNESS

We start now discussing the performance of the analytical waveform model in terms of EOB/NR unfaithfulness plots for the $\ell = m = 2$ mode, obtained computing Eq. (48) between EOB and NR waveforms. Both EOB and NR waveforms are tapered in the time-domain so as to reduce high-frequency oscillations in the corresponding Fourier transforms. Figure 3 illustrates \bar{F} versus M evaluated over the same NR waveform data used in Ref. [24], with the SXS data in the left panel and the BAM data in the right panel. As mentioned above, a subset of this data, listed in Table II, (both SXS and BAM) was used to inform the $c_3(\nu, \tilde{a}_1, \tilde{a}_2)$ function. The global performance

² SXS:BBH:1110 is excluded from this analysis since the waveform needs additional post-processing.

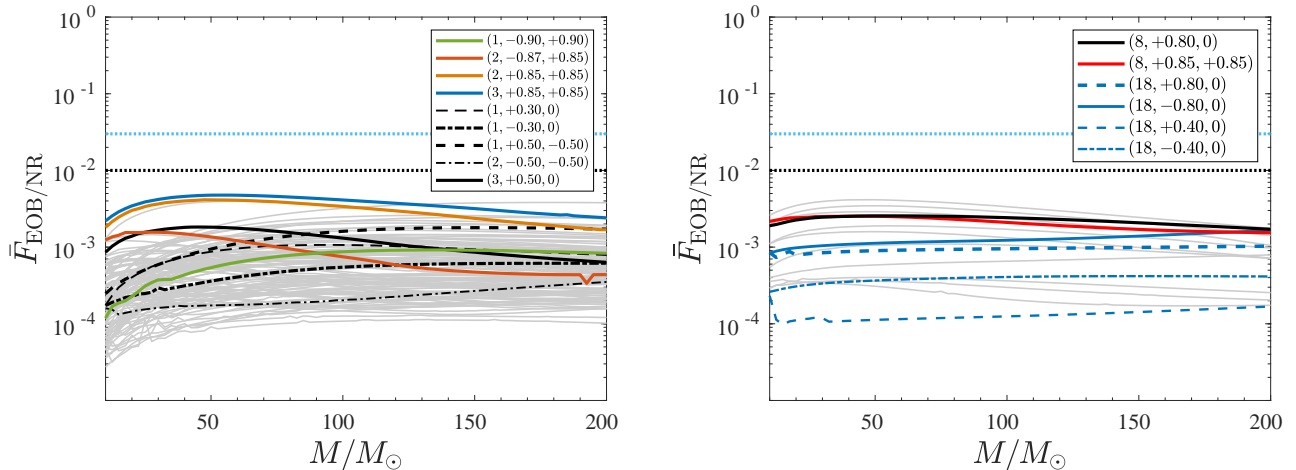


FIG. 3. EOB/NR unfaithfulness for the $\ell = m = 2$ mode obtained from Eq. (48). Left panel: computation using SXS waveforms publicly released before February 3, 2019. Right panel: same computation done with BAM waveform data. As explained in Sec. II C, a subset of all this data (see Table II) is used to inform the c_3 EOB function. Comparison with Figs. 1 and 3 of Ref. [24] allows one to appreciate the improvement with respect to the original implementation^a of `TEOBResumS`. Comparison with Fig. 2 highlights that the $\bar{F}_{\text{EOB/NR}}$ is either of the order of, or larger than the NR/NR uncertainties.

^a The reader should actually note that we changed from the, outdated, zero-detuned, high-power noise spectral density of Ref. [59] used in Ref. [24], to its most recent realization, Ref. [57].

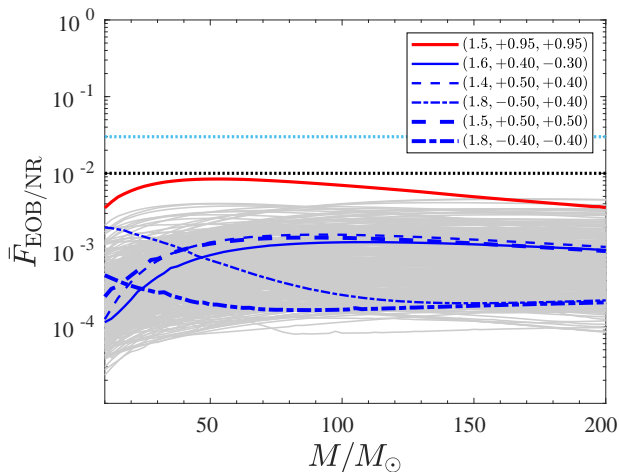


FIG. 4. EOB/NR $\ell = m = 2$ unfaithfulness computation with SXS waveform data publicly released after February 3, 2019. None of these datasets was used to inform the model in the dynamical EOB functions (a_6^c, c_3), although several were used for the postmerger waveform part. It is remarkable that $\bar{F}_{\text{EOB/NR}}^{\text{max}}$ is always below 0.4% except for a single outlier, red online, that however never exceeds 0.85%. The plot includes five exceptionally long waveforms, each one developing more than 139 GW cycles before merger, SXS:BBH:1412, 1413, 1414, 1415 and 1416 (blue online).

of the model is largely improved with respect to Ref. [24],

see Fig. 1 there³. Remarkably, the model performs excellently also for large mass ratios and large spins, without any outlier above the 1% threshold, but $\bar{F}_{\text{EOB/NR}}^{\text{max}} \lesssim 0.5\%$ all over.

After February 3, the SXS collaboration publicly released another 455⁴ new simulations at an improved accuracy. This part of the catalog mostly covers the same region of parameter space of the previous data, except for a few waveforms spanning mass ratios between 4 and 8, with spins higher than what considered before. The catalog also includes a few extremely long waveforms, with more than 100 orbits. As an additional cross check of the robustness and accuracy of our model, we compute $\bar{F}_{\text{EOB/NR}}$ all over this new set of NR waveforms. The result is displayed in Fig. 4. We find that $\bar{F}_{\text{EOB/NR}}^{\text{max}}$ always remains *below* 0.85%, a value reached only by one

³ In this respect, it is interesting to note that \bar{F} for $(2, +0.85, +0.85)$ is now around the 10^{-3} level, while in Fig. 1 of [24] is around 10^{-4} . This happens because the difference between c_3^{fit} and $c_3^{\text{first-guess}}$ is now larger than what it was in [24], see Table I there. A priori, a more flexible fitting function for c_3 would allow one to obtain even smaller values of $\bar{F}_{\text{EOB/NR}}$. Since the EOB/NR performance of the model is already rather good, we content ourselves of the current, simple, analytical representation of c_3 .

⁴ The 5 very *long* (> 100 GW cycles) simulations are separately discussed in Sec. IV A below.

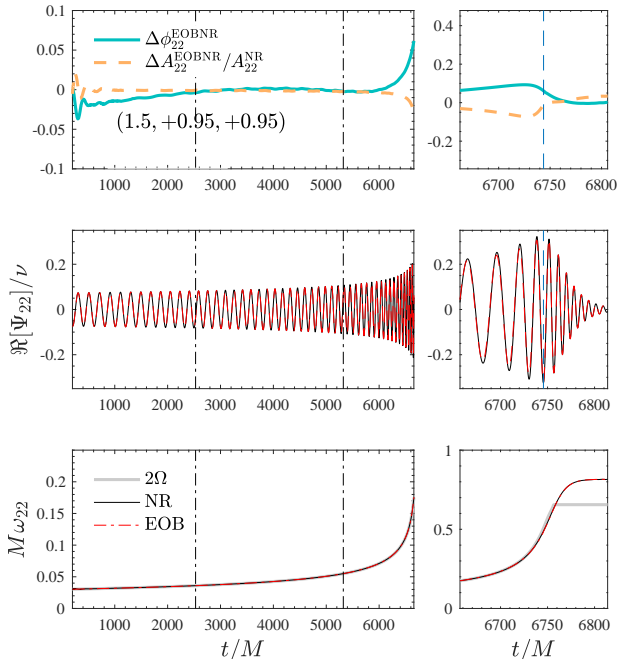


FIG. 5. Improved EOB/NR phasing comparison for SXS:BBH:1146 when the value of $c_3^{\text{fit}} = 15.96$ used in Fig. 4 is lowered to $c_3 = 11.1$. Top panel: (relative) amplitude and phase differences. Middle panel: real part of the waveform. Bottom panel: gravitational frequencies. For convenience, also twice the EOB orbital frequency 2Ω is shown on the plot. The dash-dotted vertical lines indicate the alignment frequency region, while the dashed one the merger time. This comparison illustrates that SXS:BBH:1146 is an outlier in Fig. 4 only because of the rather limited amount of NR waveforms used to inform c_3^{fit} .

dataset, $(1.5, +0.95, +0.95)$ SXS:BBH:1146, while for all others we have $\bar{F}_{\text{EOB/NR}}^{\text{max}} \lesssim 0.4\%$. This is not surprising since the set of NR waveforms used to inform c_3 does not cover, except for one single dataset with $(1.5, -0.5, 0)$, the parameter space with $1 < q < 2$. In this respect, to better understand the behavior of this outlier in Fig. 4 we checked that $c_3^{\text{fit}}(1.5, +0.95, +0.95) = 15.96$ yields an accumulated EOB/NR phase difference ~ 4.7 rad at merger once the two waveforms are aligned during the inspiral. Interestingly, by *lowering* the value of c_3 , and thus *increasing* the magnitude of the spin-orbit effective coupling and thus making the EOB waveform longer, we can easily reconcile it with the NR data. For convenience we illustrate this result in Fig. 5, that is obtained with $c_3 = 11.1$ (the two dash-dotted vertical lines indicate the alignment region). We also point the reader to Table XI, where the NR uncertainty for this dataset is estimated to be $\bar{F}_{\text{NR/NR}} = 0.0446\%$. On a different note, this suggests that the current model could be additionally, and easily, improved by also considering SXS:BBH:1146 to inform c_3^{fit} . Yet, this results highlights the robustness of our model: without any additional input from NR simulations to determine c_3 , it is able to deliver rather accurate

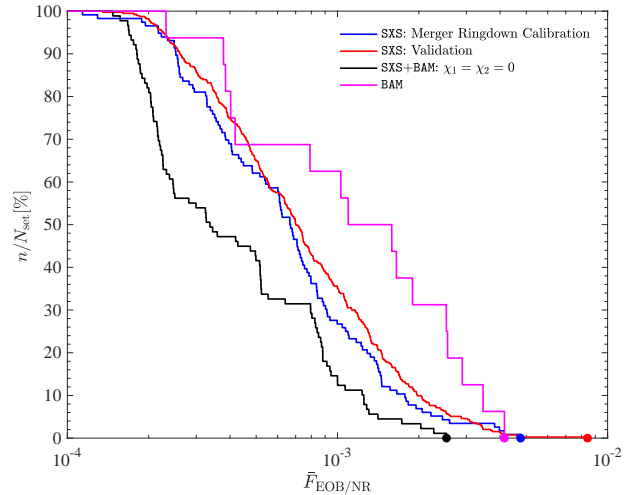


FIG. 6. Global representation of $\bar{F}_{\text{EOB/NR}}^{\text{max}}$ all over the SXS (595) and BAM (19) NR simulations. The various SXS subsets, nonspinning (black online, 89 waveforms), merger-ringdown calibration (blue online, 116 spin-aligned waveforms) and validation (red online, 388 spin-aligned waveforms) discussed in the text are represented separately. The plot shows the fraction (expressed in %) n/N_{set} , where N_{set} is the total number of waveforms in a given NR-waveform set and n is the number of waveforms, in the same set, that, given a value \bar{F} , have $\bar{F}_{\text{EOB/NR}}^{\text{max}} \geq \bar{F}$. The colored marker highlight the largest values in each NR dataset. Note that this plot incorporates 460 new SXS waveforms that were not included in Fig. 6 of [24].

waveforms even in a region of the parameter space previously not covered by NR data. The model performance is summarized in Fig. 6. For each dataset considered above, the figure exhibits the fraction of waveform whose $\bar{F}_{\text{EOB/NR}}^{\text{max}}$ is larger or equal a given value \bar{F} . Thanks to the additional analytical information incorporated and to the improved waveform resummation, `TEOBiResumS_SM` is currently the EOB model that exhibits the lowest EOB/NR unfaithfulness for the $\ell = m = 2$ mode.

A. Long-inspiral Numerical Relativity waveforms

It is interesting to note that the 5, long, NR simulation exhibit an excellent agreement ($\bar{F}_{\text{EOB/NR}} \simeq 10^{-3}$, see Fig. 4) with the analytical waveform, even during the long inspiral phase. Note that this is below the NR-uncertainty estimate in the right panel of Fig. 2 without any input in the model coming from this data. Despite such good agreement for the usual standard, an illustrative time-domain comparison done for SXS:BBH:1415, see Fig. 7, highlights some features that is worth com-

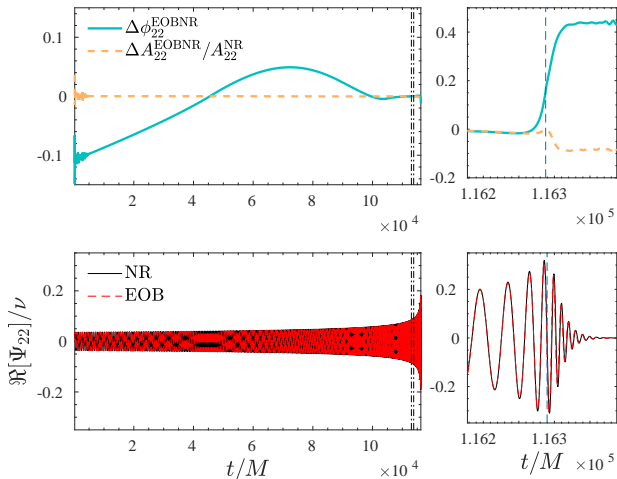


FIG. 7. EOB/NR phasing comparison for SXS:BBH:1415, (1.5, +0.50, +0.50). Note that it doesn't seem possible to flatten the phase difference up to $t/M \simeq 1 \times 10^5$. The vertical lines indicate the alignment frequency region $[M\omega_L, M\omega_R] = [0.038, 0.042]$. See text for additional discussion.

menting on⁵. At first glance, the phase agreement is excellent for any standard quality assessment, always between ± 0.1 rad. However, contrary to our expectations, we didn't succeed in flattening the phase difference by aligning the EOB and NR waveform during the early inspiral. This is usually achieved by narrowing the alignment frequency window $[M\omega_L, M\omega_R]$ and moving it to early-inspiral frequency values. By contrast, to achieve a rather flat phase difference on a reasonably large time-interval we had to progressively displace interval the frequency window to *higher* frequencies, until hitting $[M\omega_L, M\omega_R] = [0.038, 0.042]$, that corresponds to the two, dash-dotted, vertical lines in Fig. 7. In view of the rather large uncertainty on this NR waveform, we cannot really state whether this is due to some systematics in the NR waveforms or in missing physics within the EOB model. Additional analyses done using more sophisticated phasing diagnostics, e.g. the gauge-invariant $Q_\omega \equiv \omega^2/\dot{\omega}$ function [42, 60, 61], where $\omega \equiv \dot{\phi}$ is the gravitational wave frequency, might be necessary to better investigate the low-frequency consistency between the EOB and NR waveforms. An analogous behavior is shared also by the other long-term waveforms. However Fig. 4 highlights that the $\bar{F}_{\text{EOB/NR}}$ for SXS:BBH:1414 (1.83, -0.5, +0.4) and SXS:BBH:1416 (1.78, -0.4, -0.4) show a qualitatively different behavior, with $\bar{F}_{\text{EOB/NR}}$ that is starting at a slightly increased value for $M = 10M_\odot$ and then is progressively decreasing with M . When aligning the waveforms in the same frequency interval $[0.038, 0.042]$, so to obtain a quasi-flat

⁵ See Paper I and references therein for additional details concerning the alignment procedure.

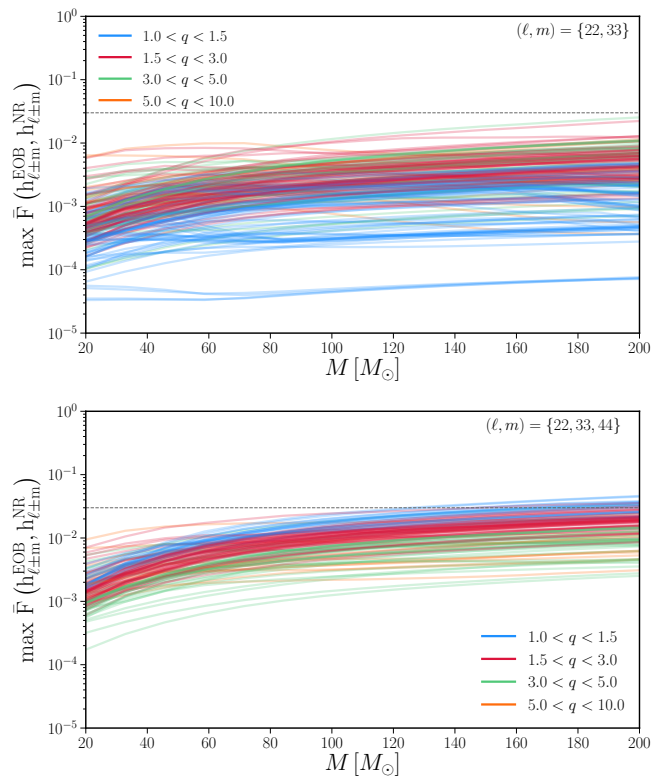


FIG. 8. EOB/NR unfaithfulness computation putting together all $\ell = m$ modes up to $\ell = 4$. Plotted is the worst-case performance maximizing the unfaithfulness over the sky, Eq.(49). The worst-case mismatches arise from near edge-on configurations, when the power emitted in the (2, 2) mode is minimized.

phase difference also outside the alignment window, one finds that the EOB/NR phase difference grows linearly backwards for $10^5 M$, to reach the 0.5-0.7 rad at the beginning of the inspiral. Although this fact might explain the behavior of $\bar{F}_{\text{EOB/NR}}$ seen in Fig. 4, conclusive NR-quality assessments require more detailed investigations that are postponed to future work.

V. HIGHER MULTIPOLAR MODES

A. Multipoles (2, 2), (3, 3) and (4, 4)

Let us move now to discussing the quality of the higher modes. For illustrative purposes, we consider explicitly four configurations with $q = 3$, with equal spins, both aligned or anti-aligned to the orbital angular momentum. More precisely, we use (3, -0.85, -0.85), (3, -0.60, -0.60), (3, -0.30, -0.30) and (3, +0.60, +0.60). The qualitative (and quantitative) behavior discussed here for this configuration is general enough to be considered paradigmatic all over the SXS waveform catalog. Figure 9 illustrates the behavior of the (2, 2), (3, 3) and

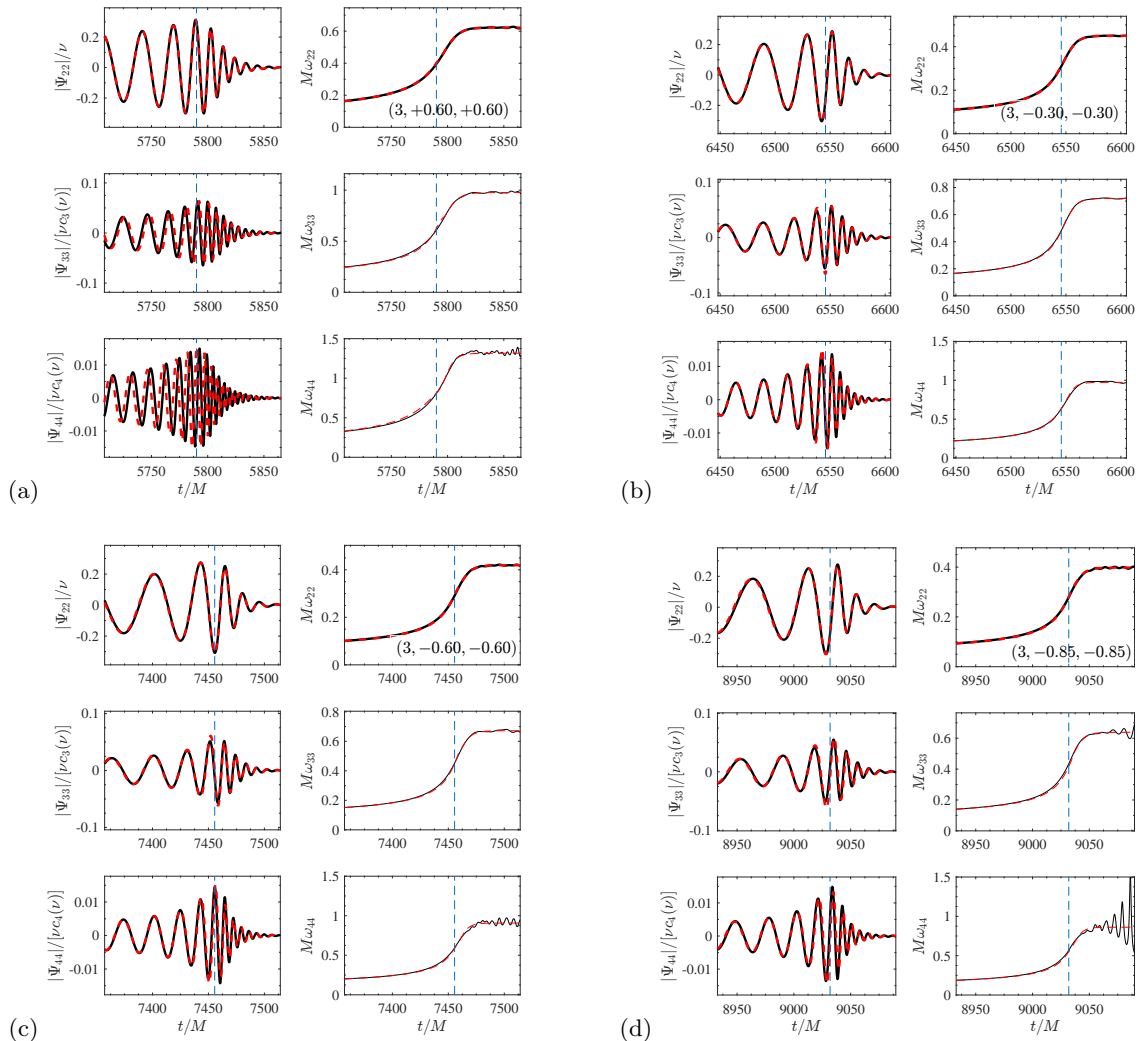


FIG. 9. Behavior of (2, 2), (3, 3) and (4, 4) modes for a few, illustrative, spin-aligned configurations with $q = 3$: comparing NR (black) with EOB (red) waveform. Each panel plots the real part (left columns) and the instantaneous frequency (right columns).

(4, 4) mode. For each multipole, we show the real part of the EOB/NR waveforms together with the instantaneous GW frequency $\omega_{\ell m}$. The EOB waveform is aligned to the NR one around merger, so to highlight the excellent EOB/NR agreement there. The EOB/NR agreement is rather good either for spins both anti-aligned or aligned with the orbital angular momentum. We should, however, mention that when the spins are large and aligned there is an increasing dephasing accumulating between the EOB and NR (4, 4) mode, as one can see in Fig. 9 (a). As it was the case for the $\ell = m = 2$ mode discussed above, a global understanding of the actual performance of the model comes from EOB/NR unfaithfulness computations. In addition to Eq. (48), due to the non-trivial angular dependence introduced by the subdominant spherical harmonics, we consider the worst-case performance of the model by maximizing the unfaithfulness over the

sky

$$\max \bar{F}(h_1, h_2) \equiv \max_{\theta, \phi} \bar{F}(h_1, h_2). \quad (49)$$

In Fig. 8, we show the worst case performance for the $\ell = m$ modes up to $\ell = 4$, finding excellent agreement up to $\sim 120M_\odot$ above which the model performance degrades slightly and moves above 3%. In all cases, the worst case mismatches arise from near edge-on configurations, where the power in the (2,2)-mode is minimized. The worst mismatches occur for mass ratios $1 \leq q \leq 1.5$ and equal-spin configurations, in which the approximate symmetry of the binary leads to a suppression of odd- m modes. For these binaries, the degraded performance will be driven by the accuracy of the (4, 4) mode in both the EOB model and the underlying NR data itself.

B. Other subdominant multipoles

1. Multipoles (2, 1), (3, 2) and (5, 5)

Let us discuss now modes (2, 1), (3, 2) and (5, 5), that can be robustly constructed over most (but crucially not all) the parameter space. To illustrate the typical behavior, we consider the same BBH configurations show in Fig. 9, but we focus now on amplitude and frequency. Each panel of the figure compares four curves: the NR one (black), the analytical EOB waveform (orange), the NQC-corrected EOB waveform (light-blue) and the complete EOB waveform that includes the ringdown part. In addition, on the (2, 1) frequency we also superpose the EOB orbital frequency, as a grey line. The blue, dashed, vertical lines in the plot mark the location of the merger point, i.e. the peak of the (2, 2) waveform amplitude. A few considerations first on the NR waveforms: during the ringdown, one clearly sees in the (2, 1) and (3, 2) the effect of mode mixing, that shows up as amplitude modulations and frequency oscillations. The origin of these features has been explained in details in Ref. [62]. By contrast, the (5, 5) mode shows features that clearly highlight some lack of accuracy in the NR data. This is more evident in both (3, -0.60, -0.60) and (3, -0.85, -0.85) configurations (see bottom rows of the (c) and (d) panels of Fig. 10. Let us focus first on the (3, 2) mode. Despite the absence of mode-mixing, the complete EOB waveform qualitatively reproduces the behavior of the NR one around peak and postpeak, especially for what concerns the amplitude. By contrast, the ringdown frequency, i.e. in the postpeak regime, is flat and *systematically larger* than the NR one because of lack of the physical information in the ringdown modelization. It is however interesting to note that the approximation is more reliable for large, anti-aligned, spins. Similarly, the shape of the waveform entailed by the action of the NQC is rather accurate and yields a reliable approximation of the frequency behavior up to merger. By contrast, the situation is different for the (2, 1) mode. When spins are aligned with the angular momentum, the standard procedure for improving the behavior of the merger waveform via NQC and the ringdown attachment works well, consistently with the nonspinning case discussed in Ref. [30]. This is clear for the case (3, +0.60, +0.60) of Fig. 10 and the procedure remains robust at least up to (3, -0.30, -0.30) as the figure illustrates. By contrast, as the magnitude of the anti-aligned spins increase, the NQC correction becomes progressively inaccurate and the resulting waveform becomes incompatible with the NR ones. This is for example the case for (3, -0.85, -0.85), where the NQC correction is unable to act so as to smoothly connect the inspiral, plunge and merger waveform to the ringdown (postmerger) part. This latter is, by contrast, reliable, except for the mode-mixing oscillation, that is missing by construction. We tracked the reason of the unphysical behavior of the NQC correction as follows. In our approach, that is the same of the nonspinning case, Paper I, the

NR information used to determine the NQC parameters is extracted $2M$ after the (2, 1) peak. As a consequence, for a successful implementation, the NQC factor should be evaluated there. Unfortunately, the EOB dynamics in this region, that is *after* merger time (i.e. the peak of the (2, 2) mode), may develop unphysical features depending on the values of the spins. The simplest way to explain what is going on is by looking at the orbital frequency, Ω . This is shown as a grey line in the (2, 1) panels of Fig. 10. One sees that for both (3, -0.60, -0.60) and (3, -0.85, -0.85) Ω becomes very small around the peak of the (2, 1) mode until it crosses zero and becomes negative. This is unexpected for this configuration and not what it is supposed to be. The unphysical character of this feature can be understood by qualitative comparison with the system made by a point-particle inspiralling and plunging on a Kerr black hole. In this case, the orbital frequency changes sign for configurations where the spin of the black hole is antialigned with the orbital angular momentum and large: the frame dragging exerted by the black-hole space time on the particle is responsible of the sign change in the frequency (see e.g. Ref. [44]). One should be aware that such dynamical behavior reflects on the waveform, and in particular on the QNMs frequency excitations, notably also at the level of the (2, 2) mode, that should have a zero at the time when the angular velocity of the particle changes sign (i.e., from counterrotation with respect to the black hole, to rotating with the black hole). Such qualitative features are not present in the NR waveform, so we believe that the EOB frequency behavior for this configuration is incorrect after merger time. This suggests that the current Hamiltonian should be modified so to avoid this feature. At a practical level, the fact that Ω crosses zero when the values of the relative separation r is small, but finite, implies that the NQC functions $n_4 \equiv p_{r_*}/(r\Omega)$ and $n_5 \equiv p_{r_*}/(r\Omega)\Omega^{2/3}$ (see Paper I) become very large and prevent the related NQC correction to the phase to act efficiently so to correctly modify the bare inspiral waveform. This is evident in panel (c) and (d) of Fig. 10. This problem affects the (2, 1) for any mass ratio when the anti-aligned spin(s) are sufficiently large. For example, a similar behavior is found also for (8, -0.90, 0). As a consequence, to use the current multipolar model for actual parameter estimation studies, it will be necessary to determine the precise region of the parameter space where the (2, 1) mode is reliable. Selecting only those datasets with $\chi_i > -0.4$, Fig. 11 shows the EOB/NR unfaithfulness, maximized over the sky, when including modes (2, 2), (2, 1) and (3, 3). Further improvement, as well as the determination of the precise range of reliability of the (2, 1) mode through merger and ringdown, are postponed to future work. Here we will just briefly explore, in Sec. VB3 below, a possible modification to the current spin-orbit sector of the Hamiltonian that may eventually improve the behavior of the (2, 1) mode in the anti-aligned spin case.

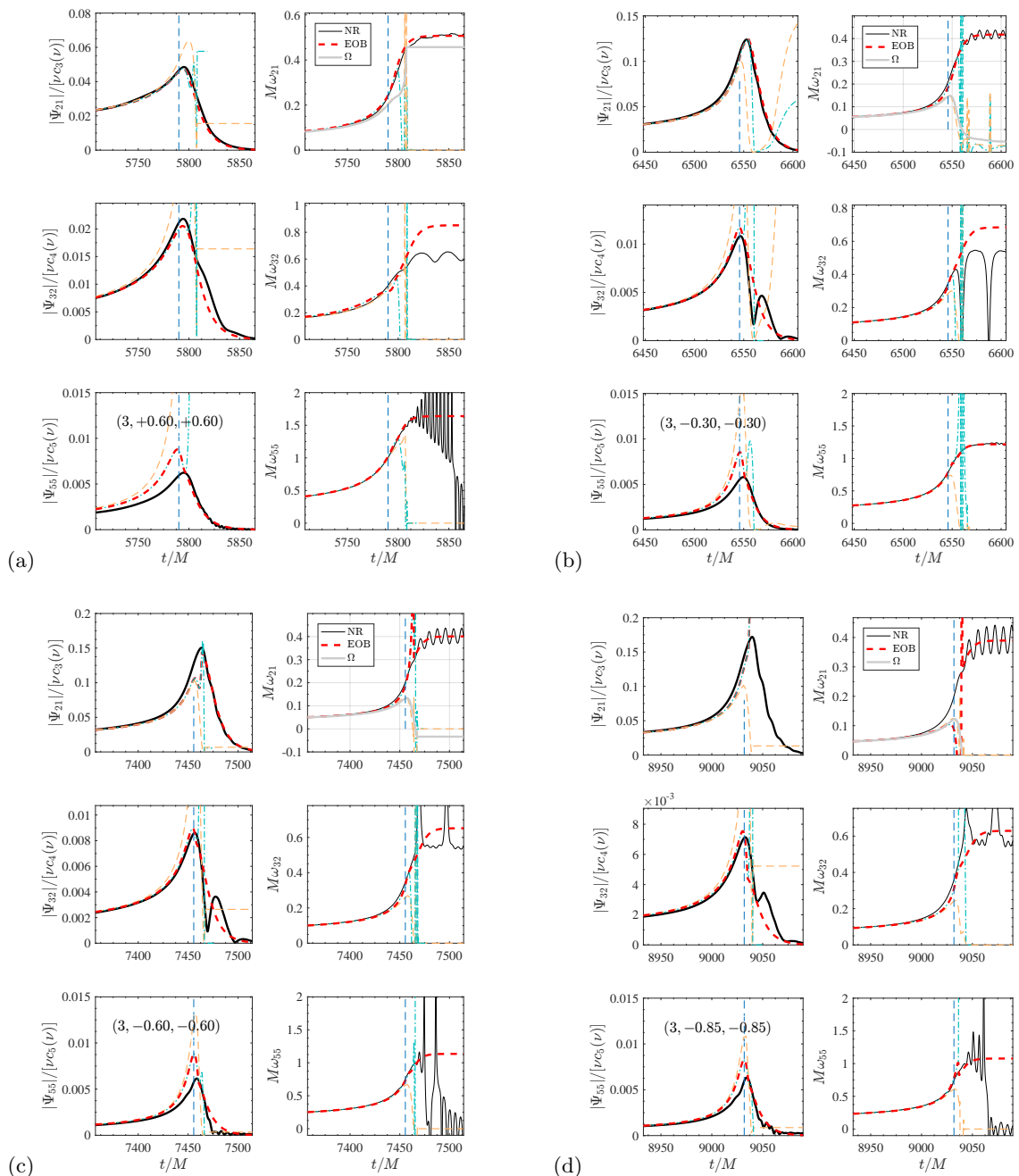


FIG. 10. Frequency and amplitude for the (2, 1), (3, 2) and (5, 5) modes for the same BBH configurations of Fig. 9. On top of the NR (black) and complete EOB curves (red, dashed), the plots also show: (i) the analytical EOB waveform, without NQC corrections and ringdown (orange online) and (ii) the NQC-augmented EOB waveform (light-blue online). The dashed, vertical, line marks the merger location, i.e. the peak of the $\ell = m = 2$ waveform amplitude. The (2, 1) frequency plots also incorporate the orbital frequency Ω (grey online). The construction of the (2, 1) mode through merger and ringdown cannot be accomplished correctly for large values of the spins anti-aligned with the orbital angular momentum [see panel (c) and (d)].

2. Multipoles (3, 1), (4, 3) and (4, 2)

From fits of the SXS waveforms we can also obtain a postmerger/ringdown description of the (3, 1), (4, 2) and (4, 3) modes. For simplicity and robustness, the (3, 1) ringdown relies on the nonspinning fits of Ref. [30], while

for (4, 3) and (4, 2) the relevant information is found in Appendix C 2g-C 2f. When the magnitude of the spins are relatively mild, these modes can be modeled rather accurately (modulo mode mixing during ringdown) as in the nonspinning case [30]. Figure 12 illustrates this fact for (3, +0.30, +0.30), with the usual EOB/NR compar-

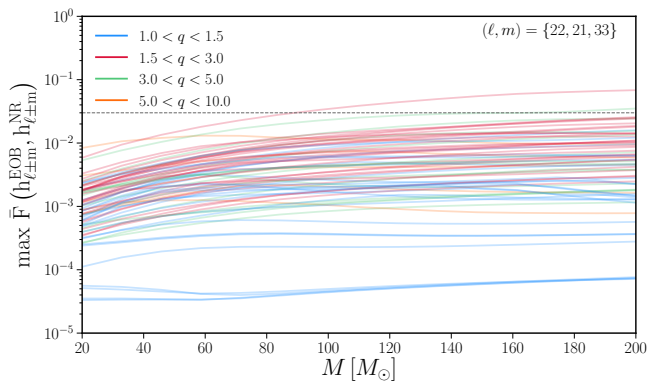


FIG. 11. EOB/NR unfaithfulness, maximized over the direction from the sky, when including (2, 2), (2, 1) and (3, 3) modes. Here we only consider a subset of the SXS waveforms with $\chi_i > -0.4$, where the (2, 1) EOB waveform mode does not present pathologies (see Fig. 10). The worst case configuration is SXS:BBH:0239, a binary of mass ratio and spins (2.0, $-0.37, +0.85$).

ison as we did above. For (4, 3) and (4, 2) modes one can appreciate the relevant action of the NQC factor. When spins are larger (and notably anti-aligned) one can have Ω -driven pathological effects like the (2, 1) mode discussed above. Seen also the (average) lower accuracy of the corresponding NR modes all over the SXS catalog, we postpone a more detailed discussion (and possible improvements) to future work.

3. Improving the behavior of the (2, 1) multipole

The correct behavior of the orbital frequency Ω in the strong-field regime is determined by subtle compensation between the orbital and spin-orbit part of the Hamiltonian. This is the region where our analytical understanding is weaker, as we have to rely on resummed results that are analytically incomplete. From the practical point of view, to NQC-complete the inspiral (2, 1) mode following the current scheme it would be sufficient the behavior of Ω be milder after the merger. In practice, we found that this is possible by implementing a small modification to the resummed (G_S, G_{S^*}) functions. The spin-orbit sector of the Hamiltonian is based on Ref. [33], in particular the gyro-gravitomagnetic functions are given by Eqs. (38), (39), (41), and (42), where the inverse separation u is replaced by the inverse centrifugal radius u_c . While $G_S^0 = 2uu_c^2$, Eq. (38) of Ref. [33], has the structure of the Kerr gyro-gravitomagnetic function, the dependence of u_c introduced in the other functions, $G_{S^*}^0$, \hat{G}_S and \hat{G}_{S^*} was an arbitrary choice. One finds that replacing such u_c dependence with the, more natural, u -dependence is sufficient to provide small modifications in the behavior of Ω that entail a far more robust behavior

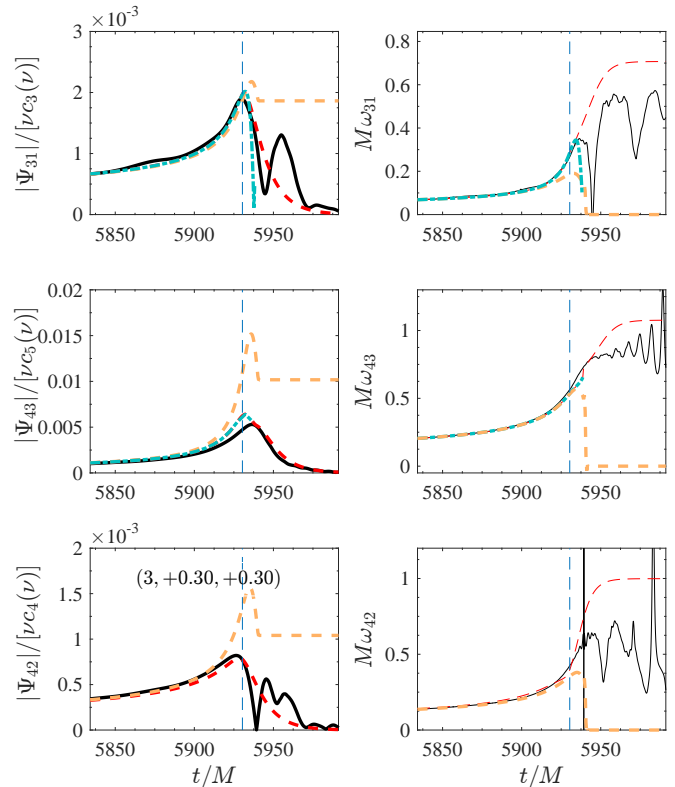


FIG. 12. Illustrative EOB/NR comparison for modes (3, 1), (4, 3) and (4, 2) for (3, +0.3, +0.3). This behavior is analogous to the nonspinning case and is robust until the spins are mild. For larger spins, these modes may suffer the same problem related to the NQC factor discussed above for the (2, 1) mode.

of the NQC correction. In practice, we use

$$G_S = 2uu_c^2 \hat{G}_S(u), \quad (50)$$

$$G_{S^*} = \frac{3}{2}u^3 \hat{G}_{S^*}(u), \quad (51)$$

where (\hat{G}_S, \hat{G}_{S^*}) are given by Eqs. (41)-(42) of Ref. [33] where u_c is replaced by u . The result of this change for (3, $-0.85, -0.85$) is illustrated in Fig. 13. Note that, since the dynamics has now changed, to get a good (2, 2) EOB/NR phasing agreement we had to use $c_3 = 86.5$ instead of $c_3^{\text{fit}} = 79.98$ from Eq. (39). Comparing Fig. 13 with the panel (d) of Fig. 10 one immediately notices the different behavior of the orbital frequency, whose peak is shallower than before. The consequence of this behavior is that the action of the NQC factor on both amplitude and frequency is more correct than before, though not yet fully accurate for this latter. Although improvable, this proves that the scheme for completing the EOB waveform through merger and ringdown for all modes that was seen to be efficient in the nonspinning case [30] can be straightforwardly generalized to the spinning case provided the dynamics, i.e. the orbital frequency, behaves correctly. The result of Fig. 13 gives us a handle to improve the description of spin-orbit effects within the EOB

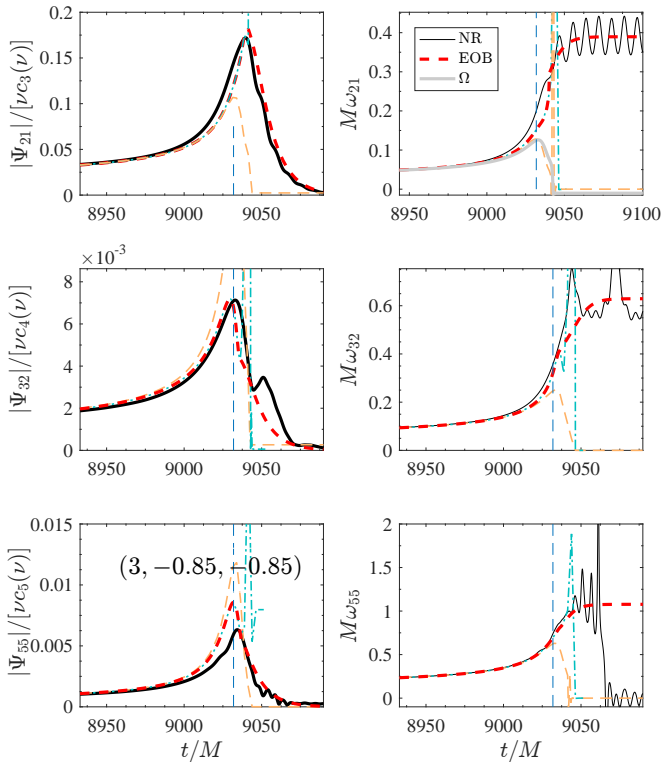


FIG. 13. Attempt of improving the behavior of the (2,1) mode for $(3, -0.85, -0.85)$ by modifying the spin-orbit sector of the EOB Hamiltonian. The related change in the EOB orbital frequency, Ω , that is seen now to decrease more mildly after its peak than in Fig. 10 (d), is sufficient to improve the efficiency of the NQC correction, so to get a more acceptable frequency growth that can be smoothly connected with the rigdown. See text for additional details.

TABLE IV. Frequency of the minimum of the (2,1) amplitude for a few BBH configurations considered in Ref. [15] and not publicly available. $M\Omega_0$ is the (orbital) frequency corresponding to a minimum (or a zero) in the amplitude. Our EOB-predicted value, from the zero of \hat{f}_{21}^S in Table I, is more consistent with the NR one than the straightforward PN value.

Name	q	χ_1	χ_2	\hat{S}	$M\Omega_0^{\text{NR}}$	$M\Omega_0^{\text{EOB}}$	$M\Omega_0^{\text{PN}}$
SXS:BBH:0614	2	0.75	-0.5	0.278	0.083	0.0968	0.057
SXS:BBH:0612	1.6	0.5	-0.5	0.115	0.068	0.0712	0.047
SXS:BBH:1377	1.1	-0.4	-0.7	-0.268	0.033	0.0330	0.029

Hamiltonian in future work.

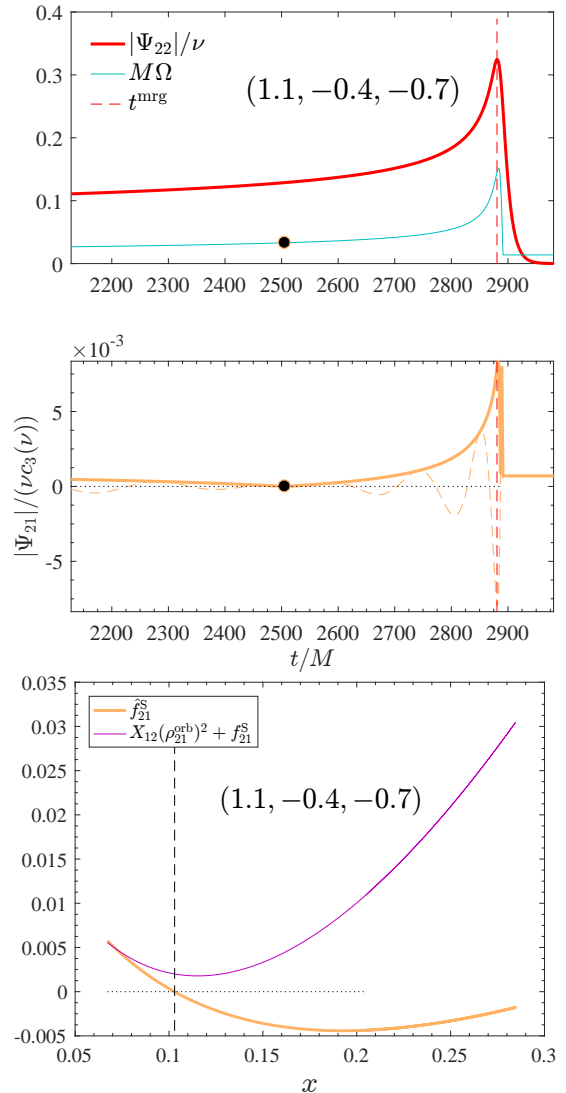


FIG. 14. Top and medium panels: occurrence of a zero in the (2,1) amplitude in configuration $(1.1, -0.4, -0.7)$, corresponding to NR dataset SXS:BBH:1377 analyzed in Ref. [15]. This dataset is not publicly available through the SXS catalog. The EOB-predicted value of the frequency is perfectly compatible with the NR value reported in Ref. [15] (see the last row of Table IV). The bottom panel compares the zero location of the resummed (orange) and non-resummed (magenta) amplitudes. See text for details.

C. Peculiar behavior of $m = 1$ waveform amplitudes for $1 \leq q \leq 2$.

Reference [15] pointed out that a few NR simulations exhibit a minimum in the (2,1) mode amplitude in the late inspiral phase. Such behavior was found in 4 SXS datasets: SXS:BBH:0254 $(2, +0.6, -0.6)$; SXS:BBH:0612 $(1.6, 0.5, -0.5)$; SXS:BBH:0614 $(2, +0.75, -0.5)$; and SXS:BBH:1377 $(1.1, -0.4, -0.7)$. Only the first among these dataset is public through the SXS catalog. In addi-

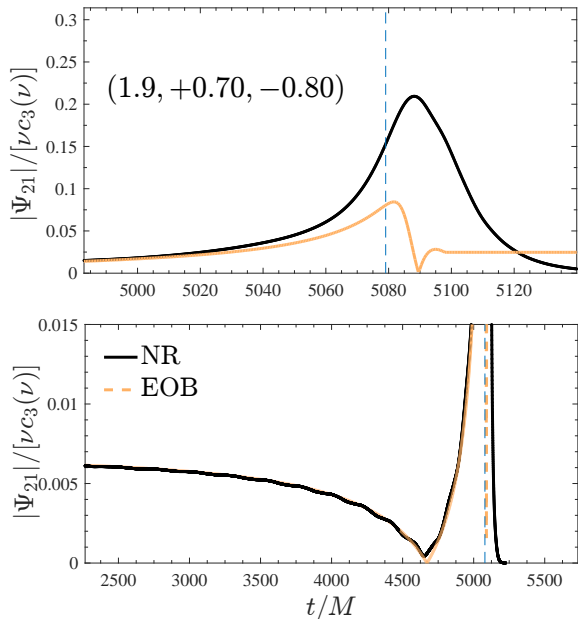


FIG. 15. Mode (2,1): comparison between the EOB amplitude (orange) and the corresponding NR one from dataset SXS:BBH:1466. The purely analytical EOB waveform multipole can accurately predict the location of the minimum (that analytically is a zero of the modulus) consistently with the one found in the NR data. The excellent agreement shown is obtained *naturally*, without the need of calibrating any additional parameter entering the waveform amplitude. The dashed vertical line corresponds to merger time, i.e. the peak of the $\ell = m = 2$ waveform. The cusp in the analytical amplitude occurs because of a zero in \hat{f}_{21}^S as illustrated in Fig. 16.

tion, Ref. [15] noticed that the same feature is present in the EOB resummed waveform (both in orbital-factorized and non-orbital factorized form). An explanation of this phenomenon was suggested on the basis of leading-order considerations, that were similarly proven using a 3PN-based analysis. In addition, Ref. [15] compared the PN prediction for the frequency corresponding to the minimum of the (2,1) mode with the value extracted from NR simulations. From this PN-based analysis, Ref. [15] suggested that the phenomenon comes from a compensation between the spinning and leading-order nonspinning terms entering the (2,1) mode. Notably, the PN based analysis aimed at explaining this feature qualitatively as well as semi-quantitatively (see Table I in Ref. [15]).

Here we revisit the analysis of Ref. [15] and we attempt to improve it along several directions thanks to the robustness of our factorized and resummed waveform amplitudes. In brief we can show that: (i) focusing on the same datasets considered in Ref. [15], we illustrate that the (2,1), *purely analytical* EOB amplitude has a minimum (in fact, a zero) rather close to the values reported in Table I of Ref. [15], and definitely much closer than the PN-based prediction; (ii) the phenomenon is here understood as coming from the compensation, occurring at

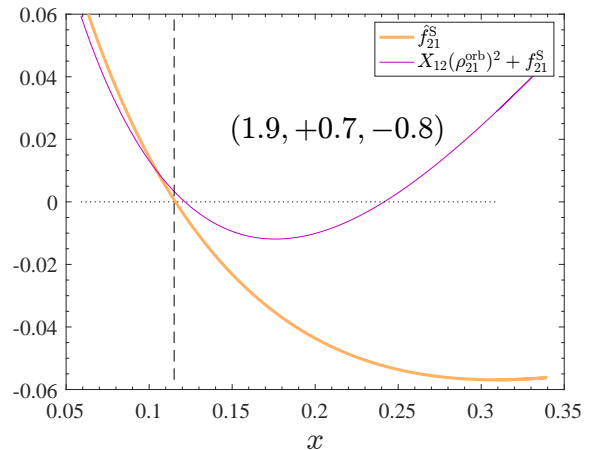


FIG. 16. Complementing Fig. 15: the behavior of the resummed versus nonresummed amplitude versus $x = \Omega^{2/3}$.

a given frequency, between the two (inverse-resummed) macro-terms that compose the analytically resummed expression of \hat{f}_{21}^S , one proportional to X_{12} and the other one proportional to \tilde{a}_{12} , and that appear with opposite signs; (iii) guided by this analytical understanding, we investigated whether some of the currently available simulations in the SXS catalog may develop a zero (that occurs in fact as a cusp) in the amplitude. Quite remarkably we found that it is indeed the case for SXS:BBH:1466, (1.9, +0.70, -0.8), that shows a clean minimum that is perfectly consistent with the EOB-based analytical prediction; (iv) since the same structure, with the minus sign, is present also in other $m = \text{odd}$ modes, we investigated whether the same phenomenon may show up also in some of the other SXS datasets. Interestingly, we found that also the (3,1) mode of SXS:BBH:1496 is consistent with the EOB-predicted analytical behavior, suggesting that such features may occur in several modes.

Let us now discuss in detail the four points listed above. Figure 14 illustrates an EOB analytical waveform for (1.1, -0.4, +0.7), that corresponds to the dataset SXS:BBH:1377. As mentioned above, this simulation is not public and so we cannot perform an explicit EOB/NR comparison. The top panel shows the $\ell = m = 2$ waveform amplitude together with the EOB orbital frequency $M\Omega$. The middle panel shows the (2,1) waveform amplitude, that develops a zero highlighted by a marker. It turns out that this zero precisely corresponds to the zero of the \hat{f}_{21}^S function once evaluated at $x = (M\Omega)^{2/3}$. This function is shown, versus x , in the bottom panel of Fig. 14. To be more quantitative, the last row of Table IV lists the corresponding frequency, that is identical to the NR-extracted value reported in the corresponding last column of Table I of [15]. To check the model further, we explored also the other two cases in the Table, similarly finding a rather good agreement between the EOB orbital frequency corresponding to the zero and

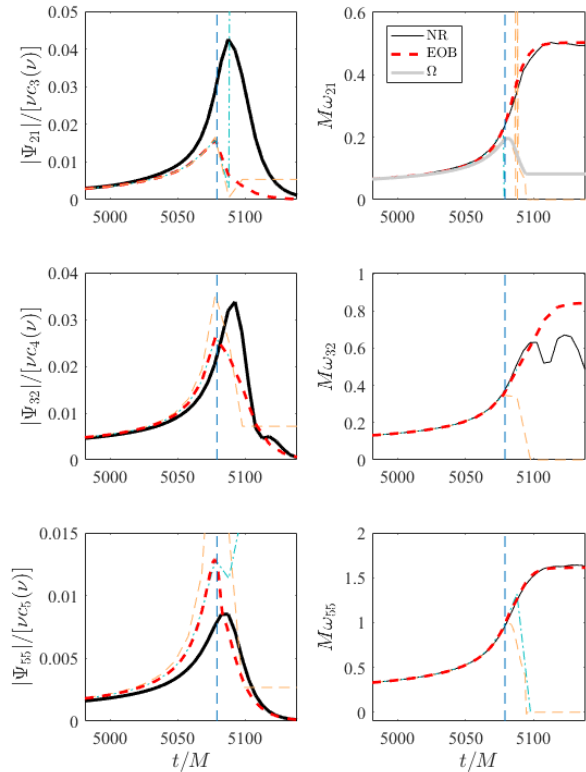


FIG. 17. EOB/NR waveform comparison for **SXS:BBH:1466** for modes (2, 1), (3, 2) and (5, 5). The frequency of the (2, 1) mode behaves correctly through merger and ringdown, while the EOB amplitude largely underestimates the NR one. As in Fig. 10, the orange curve is the purely analytical EOB waveform, while the light blue one is the NQC corrected. The vertical line marks the merger location

the NR value⁶. Our reasoning relies on our orbital factorized waveform, and in particular on the definition of \hat{f}_{21}^S . However, Ref. [15] pointed out that a zero in the amplitude may occur also in the standard, non orbital-factorized, waveform amplitude. To make some quantitative statement, we also consider the function

$$f_{21}^{\text{orb}+S} = X_{12} (\rho_{21}^{\text{orb}})^2 + f_{21}^S, \quad (52)$$

where both ρ_{21}^{orb} and f_{21}^S are kept in PN-expanded form. The orbital term is given in the usual Taylor-expanded form $\rho_{21}^{\text{orb}} = 1 + (\dots)x + (\dots)x^2 + (\dots)x^3 + (\dots)x^4 +$

⁶ Note that Ref. [15] does not explain how their $M\Omega_0^{\text{NR}}$ is computed. We may imagine that it is just given by the NR orbital frequency divided by two, which is slightly different from the EOB orbital frequency we include due to the presence of tail terms and other effects.

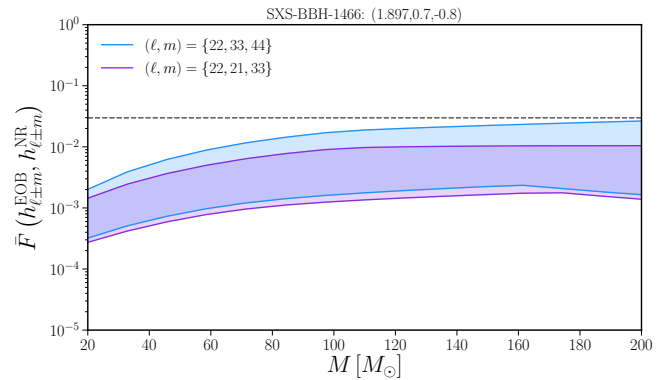


FIG. 18. The minimum and maximum EOB/NR unfaithfulness for **SXS:BBH:1466** over the whole sky. The blue curve uses the (2, 2), (3, 3) and (4, 4) modes. The purple curve uses the (2, 2), (2, 1) and (3, 3) modes. Worst case mismatches occur near edge on configurations with the unfaithfulness being below 3% up to $200M_\odot$.

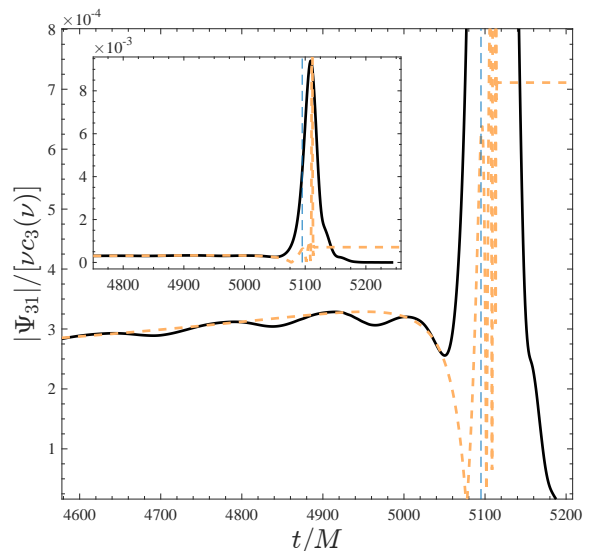


FIG. 19. Mode (3, 1): comparison between the EOB amplitude (orange) and the corresponding NR one from dataset **SXS:BBH:1496**, (1.1584, +0.7997, +0.0285). While the analytical waveform has a zero because of \hat{f}_{31} , the NR one just shows a glimpse of a global minimum, probably because of insufficient numerical resolution. Note however the excellent qualitative and quantitative consistency between the two waveforms up to that point.

(dots) x^5 . The spin term, at NNLO, reads

$$f_{21}^S = -\frac{3}{2}\tilde{a}_{12}x^{1/2} + c_{\text{SO}}^{\text{NLO}}x^{3/2} + c_{\text{SS}}^{\text{LO}}x^2 + c_{\text{SO}}^{\text{NNLO}}x^{5/2}, \quad (53)$$

where

$$c_{\text{SO}}^{\text{NLO}} = \left(\frac{110}{21} + \frac{79}{84}\nu \right) \tilde{a}_{12} - \frac{13}{84} \tilde{a}_0 X_{12}, \quad (54)$$

$$c_{\text{SS}}^{\text{LO}} = -\frac{27}{8} \tilde{a}_0 \tilde{a}_{12} + \frac{3}{8} X_{12} \left(\tilde{a}_1^2 + \frac{10}{3} \tilde{a}_1 \tilde{a}_2 + \tilde{a}_2^2 \right), \quad (55)$$

$$c_{\text{SO}}^{\text{NNLO}} = \left(-\frac{3331}{1008} - \frac{13}{504}\nu + \frac{613}{1008}\nu^2 \right) \tilde{a}_{12} \\ + \left(-\frac{443}{252} + \frac{1735}{1008} \right) \tilde{a}_0 X_{12} + \frac{3}{4} \tilde{a}_0^2 \tilde{a}_{12}. \quad (56)$$

For the configuration (1.1, -0.4, -0.7), this function, represented versus x , *does not* have a zero, as illustrated by the magenta line in the bottom panel of Fig. 14.

The closeness between the numbers in Table IV prompted us to additionally investigate for which values of spin and mass ratio the analytical (2, 1) amplitude develops a zero before merger frequency. Comparing with the configurations available through the SXS catalog (notably those up to February 3, 2019), we found that the parameters of dataset `SXS:BBH:1466` are such that the zero in the amplitude occurs at a frequency that is *smaller* than the merger frequency. We then explicitly checked the (2, 1) mode of this simulation and, as illustrated in Fig. 15, we found that it has a local minimum, that is very consistent with the cusp in the analytic EOB waveform modulus. In addition, Fig. 17 illustrates the behavior of the full waveform completed by NQC corrections and ringdown. As above, we show together the more difficult modes to model, (2, 1) and (3, 2), with (5, 5). The figure highlights that the (2, 1) frequency is well captured by the analytical model, although the amplitude is underestimated by more than a factor two. Consistently, Fig. 18 shows that the minimum and maximum unfaithfulness over the whole sky is always below 3%. This makes us confident that `TEOBiResumS.SM` can give a reliable representation of the (2, 1) mode also in this special region of the parameter space, since it naturally incorporates a feature that is absent in `SEOBNRv4HM` [15]. One should however be aware that the (2, 1) EOB mode is not as good for the case (2, +0.60, -0.60), where the corresponding NR waveform is found to have very a clean minimum much closer to the merger frequency, as noted in Ref. [15]. This is probably due to lack of additional analytical information to improve the behavior of the (2, 1) mode in the strong-field regime. It would be interesting to investigate, for future work, whether higher-order PN terms (e.g. those obtained after hybridization with test-mass results, similarly to the procedure followed for the $m = \text{even}$) could be useful to improve the behavior of the (2, 1) EOB amplitude for (2, +0.60, -0.60).

As a last exploratory study, we investigated whether some of the other m -odd multipolar amplitudes can develop a zero at a frequency smaller than the merger frequency, and we found this happens for several modes. In the SXS catalog (up to February 3, 2019) we identified a configuration where, analytically, we may expect a zero

in the (3, 1) mode. This is `SXS:BBH:1496`, with parameters (1.1584, 0.7997, 0.0285). Figure 19 compares the analytical EOB waveform amplitude with the NR one. We think it is remarkable that the NR is consistent with the analytic waveform (modulo some numerical oscillation) up to $t/M \simeq 5050$. At this time the NR waveform develops a local dip that, we conjecture, would eventually lead to an approximate cusp by increasing the resolution. We hope that these special features of the waveform could be investigated in more detail by dedicated NR simulations.

VI. CONCLUSIONS

We have introduced `TEOBiResumS.SM`, an improved, NR-informed, EOB model for nonprecessing, spinning, coalescing black hole binaries. This model incorporates several subdominant waveform modes, beyond the quadrupolar one, that are completed through merger and ringdown. The work presented here generalizes to the spinning case the nonspinning model `TEOBiResumMultipoles` presented in Paper I, Ref. [30]. Generally speaking, we found that modes with $m = \ell$, up to $\ell = 5$, are the most robust ones all over the parameter space covered by the SXS and BAM NR simulations at our disposal. The other modes, and especially the most relevant (2, 1) one, can be nonrobust for medium-to-large value of the spins anti-aligned with the orbital angular momentum. The waveform modes (and thus the radiation reaction) rely on a new resummed representation for the waveform multipolar amplitudes, that improves their robustness and predictive power through late-inspiral and merger, as well as a new, NR-informed, representation of the ringdown part.

Our results can be summarized as follows:

1. The new analytical description of the binary relative dynamics due to the orbital-factorized and resummed radiation reaction entails a new (somehow simpler) determination of the EOB flexibility functions $\{a_6^c(\nu), c_3(\nu, S_1, S_2)\}$, that is different from the one used in `TEOBResumS` [24]. We computed the EOB/NR unfaithfulness for the (2, 2) mode and found that it is always below 0.5% (except for a single outlier that grazes 0.85%) all over the current release of the SXS NR waveform catalog (595 datasets) as well as on additional data from BAM code spanning up to mass ratio $q = 18$. We remark that the performance of the model is largely improved, with respect to Ref. [24], in the large-mass-ratio, large-spin corner, notably for (8, +0.85, +0.85).
2. We provided a prescription for completing higher modes through merger and ringdown. Such prescription is the carbon copy of what previously done in the nonspinning case and discussed in Paper I. No new conceptual modification to the procedure were introduced here. The novelty is the introduction of

the spin-dependence in the NR-informed fits of the quantities needed to determine the NQC parameters and the peak-postpeak (ringdown) behavior. Such fits are done factorizing some leading-order spin contributions, as well as incorporating test-mass information, in an attempt to reduce the flexibility in the fits and to improve their robustness all over the parameter space.

We found that for $\ell = m$ modes, up to $\ell = m = 5$, the model is very robust and reliable. When putting together all $m = \ell$ modes up to $\ell = 4$, the maximal EOB/NR unfaithfulness all over the sky (with Advanced LIGO noise) is always well below 3% up to total mass $M = 120M_{\odot}$, that is exceeded slightly after because of lack of accuracy in both the EOB and the NR data itself, especially in the (4, 4) mode. The model performs similarly well ($\bar{F} \lesssim 3\%$) also when the (2, 1) mode is included. We have however pointed out that for large values of the spin, anti-aligned with the angular momentum, e.g. as (3, -0.85, -0.85), inaccuracies in the postmerger EOB dynamics prevent one to get accurate (2, 1) mode through merger and ringdown.

3. Inspired by previous work, we could confirm that the phenomenology of the (2, 1) mode is rich, in particular that its amplitude can have a zero during the late-inspiral before merger for nearly equal-mass binaries. We have presented a quantitative understanding of the phenomenon. We also showed that the EOB waveform, in its orbital-factorized and resummed avatar of Ref. [31, 32], can accurately reproduce NR waveforms with the same phenomenology, at least when the frequency of the zero is sufficiently far from merger. We remark that was achieved *without* advocating any additional ad-hoc calibration or tuning of phenomenological parameters entering the waveform amplitude. Quite interestingly, the same phenomenon may occur also in some of the other of the $m = \text{odd}$ modes. In particular, we could find, for the (3, 1) mode, a SXS configuration that shows this behavior and illustrate how it agrees with the analytical prediction.
4. In general, this work made us aware that the structure of the (2, 1) mode is very challenging to be modeled properly through peak and ringdown using the simple approach developed in Paper I. Such difficulty is shared by other modes with $m \neq \ell$ in certain region of the parameter space, whenever the peak of such mode is significantly ($\sim 7 - 8M$) delayed with respect to the merger time (e.g. the (4, 3) or (3, 1)). We consider the identification of this difficulty as one of the most relevant outcomes of this work. We think that the proper modelization of such $m \neq \ell$ modes in the transition from the late inspiral up to the waveform peak should not be done using brute force (e.g. by extending the effective postmerger fits also *before* the peak)

but rather that it requires a more detailed understanding of the underlying physical elements, in particular: (i) the structure of the waveform (e.g. with the need of naturally incorporating the zero in the amplitude also when it is known to exist at rather high frequencies, e.g. for (2, +0.60, -0.60)); and (ii) the behavior of the EOB relative dynamics (notably mirrored in the time evolution of the orbital frequency $\Omega(t)$) in the extreme region just after the merger, corresponding to very small radial separation. We have shown explicitly that one of the analytical choices adopted in `TEOBResumS`, i.e. the u_c dependence in the gyro-gravitomagnetic functions, was (partly) responsible of the problems we encountered in modeling the (2, 1) mode (see Sec. VB3). Together with a different choice of gauge, so to incorporate the test-black hole spin-orbit interaction [29], it might be possible to obtain an improved EOB dynamics more robust also in the postmerger regime, so to easily account for more subdominant multipoles via the usual NQC-completion and ringdown matching procedure.

5. The results discussed in this paper were obtained with the `Matlab` implementation of the model. However, `TEOBiResumS.SM` is freely available via a stand-alone *C*-implementation [63]. Tests of the code and evaluation of its performance in parameter-estimation context are enclosed in the related documentation and will be additionally discussed in a forthcoming publication [64]. In particular, instead of iterating on the NQC parameters (a_1, a_2), the *C*-implementation uses suitably designed fits. The performance, in terms of the $\bar{F}_{\text{EOB/NR}}$ diagnostics, is fully compatible with what discussed here.

ACKNOWLEDGMENTS

We are grateful to T. Damour for discussions. F. M., G. R. and P. R. thank IHES for hospitality during the development of this work. We thank S. Bernuzzi and R. Gamba for continuous help and assistance in the development of the stand-alone *C*-implementation of `TEOBiResumS.SM`.

Appendix A: Nonspinning limit

Here we briefly comment on the performance of the model in the nonspinning limit, as an addendum to the extensive discussion reported in Ref. [30]. In total 89 nonspinning NR waveforms are available. These are listed in Tables XVIII-XIX. Of these, 19 SXS and 3 BAM waveforms were used to inform `TEOBiResumMultipoles` for the postmerger part, see Ref. [30]. We compute \bar{F} from Eq. (48). Note that the analytical EOB waveforms are

obtained with $\chi_1 = 0$ and $\chi_2 = 10^{-4}$, so to actually probing the spin-dependent dynamics in the nonspinning limit. Figure 20 shows $\bar{F}_{\text{NR/NR}}$ (left) for the 86 SXS nonspinning waveforms and $\bar{F}_{\text{EOB/NR}}$ (right) for the full set of 89 nonspinning waveforms. Only two waveforms show a large $\bar{F}_{\text{NR/NR}}$ value: SXS:BBH:0093 ($q = 1.5$) and SXS:BBH:0063 ($q = 8$), though both remain below 8×10^{-4} . Consistently with Ref. [30], $\bar{F}_{\text{EOB/NR}}$ is well behaved all over. The largest unfaithfulness is reached by the BAM, $q = 18$ waveform at $\max(\bar{F}_{\text{EOB/NR}}) = 0.2533\%$.

Appendix B: Numerical Relativity Systematics

As was highlighted in [30], numerical noise and systematics in the NR data can lead to a degradation in the mismatches. In Fig. 8 we find that the worst mismatches typically come from near edge-on cases, where the power in the $(2, 2)$ -mode is minimized, and for mass ratios near $q \sim 1$, where the amplitude of the odd- m multipoles is suppressed. When restricting to the $(\ell, m) = (2, 2), (3, 3)$ and $(4, 4)$ modes, as shown in the bottom panel of Fig. 8, the mode that contributes the most for the near equal-mass, edge-on configurations is the $(4, 4)$ mode. However, as highlighted in Fig. 21, the $(4, 4)$ mode in the NR datasets can often be particularly problematic, especially through the merger-ringdown. In particular, we see strong oscillatory features in the instantaneous frequency and un-physical, non-monotonic behaviour in the amplitude. This can result in large mismatches that are relatively uninformative regarding the accuracy of the EOB model against NR. At higher mass ratios, where the mode is well-resolved in NR, the mismatches are under control and well below 3%. At low total masses, where we compute mismatches against a larger portion of the inspiral signal, we see excellent agreement between the EOB model and NR for all modes and configurations used in our analysis. In the mismatches shown in Fig. 8, we have removed NR datasets that display obvious pathologies, such as those demonstrated in Fig. 21.

Appendix C: Analytic modeling of the multipolar ringdown waveform

1. Introduction

In this Appendix we discuss the fits of the NR data needed for completing `TEOBiResumS.SM` through merger and ringdown. The fits concern: (i) frequency and amplitude at the peak of each multipole; (ii) the time delays $\Delta t_{\ell m}$ between the peak of each multipole and the peak of the $(2, 2)$ mode; (iii) fits for waveforms quantities at the location at the NQC extraction point. Technical details are all listed in Sec. III D and Sec. V A of Ref. [30] and we address the reader there for complementary information. In Sec. C 2 below we report fits of various wave-

TABLE V. This table summarizes the SXS NR waveform data in the *postpeak-calibration* set, with mass-ratio $q = 1$. From left to right, the columns report: the SXS simulation number, mass ratio and dimensionless spins χ_i , and the maximum value of the unfaithfulness \bar{F} between: The two highest resolutions of the NR dataset, if available, see Fig. 2, and between EOB and NR, see Fig. 3.

#	id	(q, χ_1, χ_2)	$\bar{F}_{\text{NR/NR}}^{\text{max}}[\%]$	$\bar{F}_{\text{EOB/NR}}^{\text{max}}[\%]$
1	BBH:0178	(1, +0.9942, +0.9942)	0.0066	0.0259
2	BBH:0177	(1, +0.9893, +0.9893)	0.0021	0.0345
3	BBH:0172	(1, +0.9794, +0.98)	0.0022	0.0188
4	BBH:0157	(1, +0.95, +0.95)	0.0027	0.0329
5	BBH:0160	(1, +0.9, +0.9)	0.0118	0.0114
6	BBH:0153	(1, +0.85, +0.85)	..	0.0249
7	BBH:0230	(1, +0.8, +0.8)	0.0016	0.0737
8	BBH:0228	(1, +0.6, +0.6)	0.0080	0.1458
9	BBH:0150	(1, +0.2, +0.2)	0.0027	0.0723
10	BBH:0149	(1, -0.2, -0.2)	0.0037	0.1369
11	BBH:0148	(1, -0.44, -0.44)	0.0013	0.0688
12	BBH:0215	(1, -0.6, -0.6)	0.0040	0.0903
13	BBH:0154	(1, -0.8, -0.8)	0.0036	0.0836
14	BBH:0212	(1, -0.8, -0.8)	0.0032	0.0610
15	BBH:0159	(1, -0.9, -0.9)	0.0069	0.0295
16	BBH:0156	(1, -0.95, -0.95)	0.0055	0.0798
17	BBH:0231	(1, +0.9, 0)	0.0046	0.1094
18	BBH:0232	(1, +0.9, +0.5)	0.0073	0.0430
19	BBH:0229	(1, +0.65, +0.25)	0.0053	0.1411
20	BBH:0227	(1, +0.6, 0)	0.0052	0.1776
21	BBH:0005	(1, +0.5, 0)	0.0592	0.1396
22	BBH:0226	(1, -0.9, +0.5)	0.0018	0.0679
23	BBH:0224	(1, -0.8, +0.4)	0.0020	0.0842
24	BBH:0225	(1, +0.8, +0.4)	0.0014	0.0784
25	BBH:0223	(1, +0.3, 0)	0.1520	0.1071
26	BBH:0222	(1, -0.3, 0)	0.1598	0.0616
27	BBH:0220	(1, -0.8, -0.4)	0.0040	0.1042
28	BBH:0221	(1, +0.8, -0.4)	0.0053	0.1238
29	BBH:0004	(1, -0.5, 0)	0.0189	0.0998
30	BBH:0218	(1, +0.5, -0.5)	0.2160	0.1794
31	BBH:0219	(1, +0.9, -0.5)	0.0076	0.1173
32	BBH:0216	(1, -0.6, 0)	0.0040	0.0797
33	BBH:0217	(1, -0.6, +0.6)	0.0048	0.1103
34	BBH:0214	(1, -0.62, -0.25)	0.0010	0.0621
35	BBH:0213	(1, -0.8, +0.8)	0.0040	0.0938
36	BBH:0209	(1, -0.9, -0.5)	0.0010	0.0610
37	BBH:0210	(1, -0.9, 0)	0.0024	0.0708
38	BBH:0211	(1, -0.9, +0.9)	0.0027	0.0918

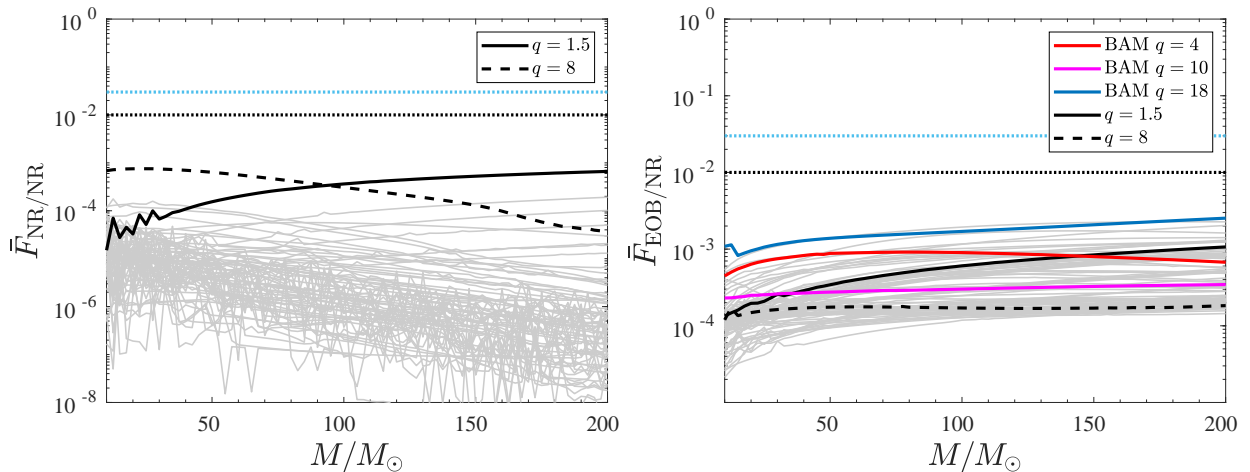


FIG. 20. Nonspinning sector. Left panel: the NR/NR unfaithfulness between the highest and second highest resolutions available. Right panel: EOB/NR unfaithfulness for all available non-spinning datasets. The analytical waveforms are evaluated with $(\chi_1, \chi_2) = (0, 10^{-4})$, so as to probe the stability of the model and its robustness in this regime.

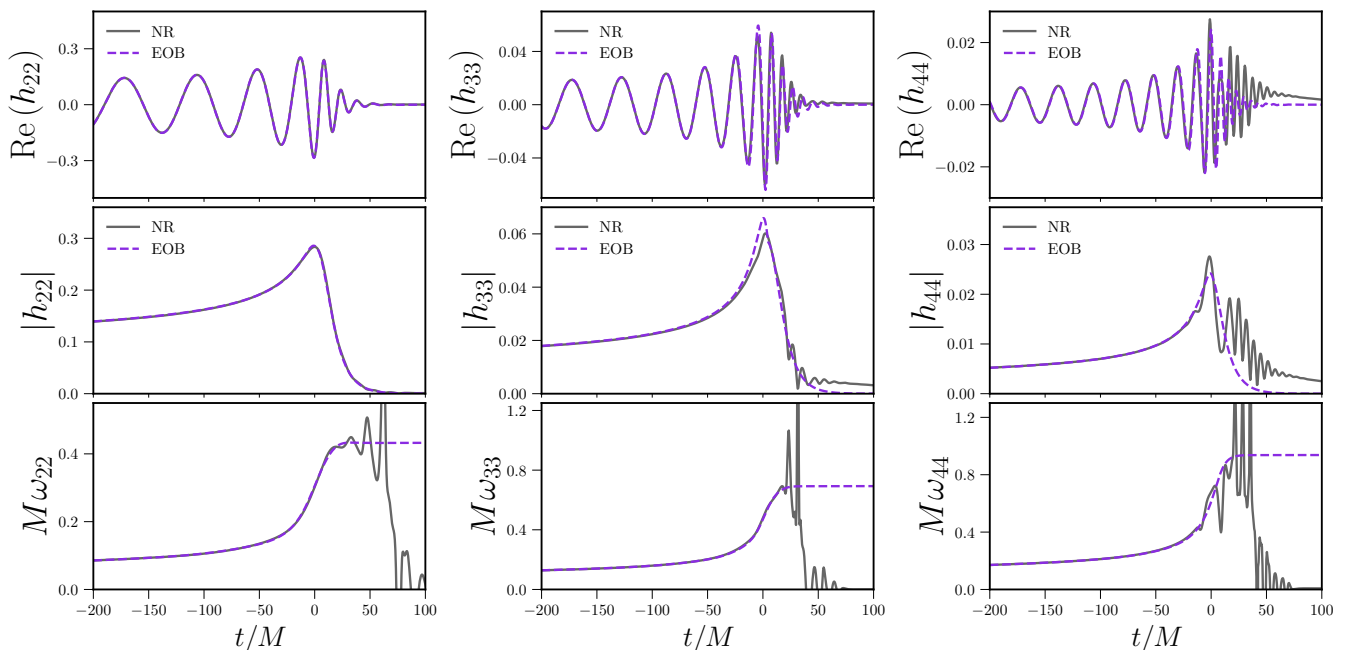


FIG. 21. Strain, amplitude and instantaneous frequency for SXS:BBH:0039. Whilst the (2,2) and (3,3) modes are well-behaved, the (4,4) mode demonstrates unphysical features, as seen by the non-monotonic behavior of the amplitude in the merger-ringdown and the strong, oscillatory features in the frequency. This is an example of how NR systematics can lead to relatively poor mismatches against the EOB model.

form quantities at the peak of each multipole, that is amplitude, frequency and time-delay $(A_{\ell m}^{\text{peak}}, \omega_{\ell m}^{\text{peak}}, \Delta t_{\ell m})$. Following Refs. [24, 30, 35, 36], the postpeak waveform needs three additional parameters $(c_3^{A\ell m}, c_3^{\phi\ell m}, c_4^{\phi\ell m})$ to be fitted to NR data. This is discussed in Sec. C3 below. We present spin-dependent fits for multipoles

(2,2), (3,3), (4,4), (5,5), although, for robustness, we prefer to use the nonspinning fits discussed in [30] except for the (2,2) mode. This gives a rather accurate representation of the waveform provided that the other quantities (e.g. the peak ones) incorporate the complete spin dependence. The fits of the quasi-normal-mode frequencies and (inverse) damping times entering $(\omega_1^{\ell m}, \alpha_1^{\ell m}, \alpha_{21}^{\ell m})$

TABLE VI. This table summarizes the SXS NR waveform data in the *postpeak-calibration* set, with mass-ratio $1 < q \leq 2$. From left to right, the columns report: the SXS simulation number, mass ratio and dimensionless spins χ_i , and the maximum value of the unfaithfulness \bar{F} between: The two highest resolutions of the NR dataset, if available, see Fig.2, and between EOB and NR, see Fig. 3.

#	id	(q, χ_1, χ_2)	$\bar{F}_{\text{NR/NR}}^{\text{max}}[\%]$	$\bar{F}_{\text{EOB/NR}}^{\text{max}}[\%]$
39	BBH:0306	(1.3, +0.96, -0.9)	0.0031	0.2059
40	BBH:0013	(1.5, +0.5, 0)	..	0.1420
41	BBH:0025	(1.5, +0.5, -0.5)	0.0278	0.2446
42	BBH:0016	(1.5, -0.5, 0)	0.0009	0.0262
43	BBH:0019	(1.5, -0.5, +0.5)	0.0213	0.0408
44	BBH:0258	(2, +0.87, -0.85)	0.0061	0.2599
45	BBH:0257	(2, +0.85, +0.85)	0.0024	0.4144
46	BBH:0254	(2, +0.6, -0.6)	0.0009	0.2218
47	BBH:0255	(2, +0.6, 0)	0.0023	0.1324
48	BBH:0256	(2, +0.6, +0.6)	0.0068	0.0771
49	BBH:0253	(2, +0.5, +0.5)	0.0040	0.0844
50	BBH:0252	(2, +0.37, -0.85)	0.0029	0.1659
51	BBH:0249	(2, +0.3, -0.3)	0.0057	0.0888
52	BBH:0250	(2, +0.3, 0)	0.0045	0.0837
53	BBH:0251	(2, +0.3, +0.3)	0.0037	0.0755
54	BBH:0248	(2, +0.13, +0.85)	0.0030	0.0666
55	BBH:0244	(2, 0, -0.6)	0.0010	0.0542
56	BBH:0245	(2, 0, -0.3)	0.0226	0.0385
57	BBH:0246	(2, 0, +0.3)	0.0081	0.0395
58	BBH:0247	(2, 0, +0.6)	0.0041	0.0440
59	BBH:0243	(2, -0.13, -0.85)	0.0006	0.0538
60	BBH:0240	(2, -0.3, -0.3)	0.0614	0.0235
61	BBH:0241	(2, -0.3, 0)	0.0129	0.0251
62	BBH:0242	(2, -0.3, +0.3)	0.0260	0.0282
63	BBH:0239	(2, -0.37, +0.85)	0.0005	0.0338
64	BBH:0238	(2, -0.5, -0.5)	0.1110	0.0351
65	BBH:0235	(2, -0.6, -0.6)	0.0048	0.0267
66	BBH:0236	(2, -0.6, 0)	0.0029	0.0483
67	BBH:0237	(2, -0.6, +0.6)	0.0014	0.0880
68	BBH:0234	(2, -0.85, -0.85)	0.0049	0.0709
69	BBH:0233	(2, -0.87, +0.85)	0.0012	0.1564

are given in [30]⁷. The waveform quantities used to determine the NQC corrections to the waveform amplitude and phase, $(A_{\ell m}^{\text{NQC}}, \omega_{\ell m}^{\text{NQC}}, \dot{A}_{\ell m}^{\text{NQC}}, \dot{\omega}_{\ell m}^{\text{NQC}})$ are usually obtained analytically from the postpeak template and all details are collected in Sec. C5 below. For the (4, 4)

⁷ The reader should note that the fits are done versus the spin of the remnant \hat{a}_f , which in turn is obtained from the fits presented in Ref. [67].

TABLE VII. This table summarizes the SXS NR waveform data in the *postpeak-calibration* set, with mass-ratio $3 \leq q$. From left to right, the columns report: the SXS simulation number, mass ratio and dimensionless spins χ_i , and the maximum value of the unfaithfulness \bar{F} between: The two highest resolutions of the NR dataset, if available, see Fig.2, and between EOB and NR, see Fig. 3.

#	id	(q, χ_1, χ_2)	$\bar{F}_{\text{NR/NR}}^{\text{max}}[\%]$	$\bar{F}_{\text{EOB/NR}}^{\text{max}}[\%]$
70	BBH:0036	(3, -0.5, 0)	0.0010	0.0405
71	BBH:0045	(3, +0.5, -0.5)	..	0.1456
72	BBH:0174	(3, +0.5, 0)	0.1040	0.1828
73	BBH:0260	(3, -0.85, -0.85)	0.0004	0.0744
74	BBH:0261	(3, -0.73, +0.85)	0.0016	0.1453
75	BBH:0262	(3, -0.6, 0)	0.0002	0.0362
76	BBH:0263	(3, -0.6, +0.6)	0.0009	0.0914
77	BBH:0264	(3, -0.6, -0.6)	0.0024	0.0449
78	BBH:0265	(3, -0.6, -0.4)	0.0008	0.0329
79	BBH:0266	(3, -0.6, +0.4)	0.0003	0.0714
80	BBH:0267	(3, -0.5, -0.5)	0.0058	0.0368
81	BBH:0268	(3, -0.4, -0.6)	0.0016	0.0249
82	BBH:0269	(3, -0.4, +0.6)	0.0017	0.0516
83	BBH:0270	(3, -0.3, -0.3)	0.0038	0.0217
84	BBH:0271	(3, -0.3, 0)	0.0014	0.0255
85	BBH:0272	(3, -0.3, +0.3)	0.0035	0.0291
86	BBH:0273	(3, -0.27, -0.85)	0.0027	0.0605
87	BBH:0274	(3, -0.23, +0.85)	0.0018	0.0355
88	BBH:0275	(3, 0, -0.6)	0.0008	0.0602
89	BBH:0276	(3, 0, -0.3)	0.0028	0.0373
90	BBH:0277	(3, 0, +0.3)	0.0029	0.0194
91	BBH:0278	(3, 0, +0.6)	0.0015	0.0252
92	BBH:0279	(3, +0.23, -0.85)	0.0010	0.0670
93	BBH:0280	(3, +0.27, +0.85)	0.0052	0.0405
94	BBH:0281	(3, +0.3, -0.3)	0.0027	0.0729
95	BBH:0282	(3, +0.3, 0)	0.0011	0.0223
96	BBH:0283	(3, +0.3, +0.3)	0.0032	0.0328
97	BBH:0284	(3, +0.4, -0.6)	0.0005	0.1288
98	BBH:0285	(3, +0.4, +0.6)	0.0013	0.0257
99	BBH:0286	(3, +0.5, +0.5)	0.0022	0.0257
100	BBH:0287	(3, +0.6, -0.6)	0.0053	0.1954
101	BBH:0288	(3, +0.6, -0.4)	0.0006	0.0683
102	BBH:0289	(3, +0.6, 0)	0.0005	0.0624
103	BBH:0290	(3, +0.6, +0.4)	0.0032	0.0260
104	BBH:0291	(3, +0.6, +0.6)	0.0010	0.0129
105	BBH:0292	(3, +0.73, -0.85)	0.0009	0.3817
106	BBH:0293	(3, +0.85, +0.85)	0.0046	0.4764
107	BBH:0060	(5, -0.5, 0)	..	0.0217
108	BBH:0110	(5, +0.5, 0)	..	0.0383
109	BBH:0208	(5, -0.9, 0)	0.0385	0.0667
110	BBH:0202	(7, +0.6, 0)	0.0048	0.3976
111	BBH:0203	(7, +0.4, 0)	0.0095	0.0556
112	BBH:0205	(7, -0.4, 0)	0.0040	0.0484
113	BBH:0207	(7, -0.6, 0)	0.0011	0.0613
114	BBH:0064	(8, -0.5, 0)	0.0338	0.0325
115	BBH:0065	(8, +0.5, 0)	0.0189	0.1440
116	BBH:1375	(8, -0.9, 0)	..	0.1223

TABLE VIII. This table summarizes the BAM NR waveform data in the *postpeak-calibration* set. From left to right, the columns report: the simulation number, mass ratio and dimensionless spins χ_i , and the maximum value of the EOB/NR unfaithfulness \bar{F} , see Fig. 3. These waveforms were mostly presented in Refs. [58, 65, 66]

#	(q, χ_1, χ_2)	$\bar{F}_{\text{EOB/NR}}^{\text{max}}[\%]$
117	(2, +0.5, +0.5)	0.3458
118	(2, +0.75, +0.75)	0.4149
119	(3, -0.5, -0.5)	0.1895
120	(4, -0.75, -0.75)	0.2898
121	(4, -0.5, -0.5)	0.1588
122	(4, -0.25, -0.25)	0.1096
123	(4, +0.25, +0.25)	0.0402
124	(4, +0.5, +0.5)	0.0385
125	(4, +0.75, +0.75)	0.0378
126	(8, -0.85, -0.85)	0.0791
127	(8, +0.8, 0)	0.2555
128	(8, +0.85, +0.85)	0.2530
129	(18, -0.8, 0)	0.1653
130	(18, -0.4, 0)	0.0418
131	(18, +0.4, 0)	0.0232
132	(18, +0.8, 0)	0.1029

mode, however, this procedure cannot deliver an accurate time-derivative of the waveform amplitude, so that a dedicated fit is given. In the case of the $(\ell, m) = (2, 2)$ mode fits for all 4 NQC quantities are also given. Unless otherwise stated all fits are done using `fitnlm` of `matlab` and `NonLinearModelFit` of `MATHEMATICA`. All fits exclusively use the the calibration set taken from the BAM catalog, test-particle data and the *calibration set* of SXS waveforms listed in Appendix III. The exception is Δt_{21} , which is informed additionally by the *test set* of SXS waveforms.

2. Modeling the peak of each multipole

Firs of all, let us recall some symmetric combinations of the spin variables that will be useful later on

$$\hat{S} \equiv \frac{S_1 + S_2}{M^2} = \frac{1}{2} (\tilde{a}_0 + X_{12} \tilde{a}_{12}), \quad (\text{C1})$$

$$\bar{S} \equiv \frac{S_1 - S_2}{M^2} = \frac{1}{2} (X_{12} \tilde{a}_0 + \tilde{a}_{12}). \quad (\text{C2})$$

We refer to the multipolar decomposition of the strain

$$h \equiv h_+ - ih_\times = \sum_{\ell, m} h_{\ell m - 2} Y_{\ell m}(\iota, \varphi). \quad (\text{C3})$$

Here $_{-2}Y_{\ell m}$ are the $s = 2$ spin-weighted, spherical harmonics. ι and φ are the polar (with respect to the direction of the orbital angular momentum) and azimuthal

TABLE IX. This table summarizes part of the SXS NR waveform data in the *validation* set with $q = 1$. From left to right, the columns report: the SXS simulation number, mass ratio and dimensionless spins χ_i , and the maximum value of the unfaithfulness \bar{F} between: The two highest resolutions of the NR dataset, if available, see Fig.2, and between EOB and NR, see Fig. 4.

#	id	(q, χ_1, χ_2)	$\bar{F}_{\text{NR/NR}}^{\text{max}}[\%]$	$\bar{F}_{\text{EOB/NR}}^{\text{max}}[\%]$
133	BBH:1124	(1, +0.9980, +0.9980)	..	0.0800
134	BBH:0158	(1, +0.97, +0.97)	0.0031	0.0510
135	BBH:0176	(1, +0.96, +0.96)	0.0065	0.0264
136	BBH:0155	(1, +0.8, +0.8)	0.0035	0.0749
137	BBH:1477	(1, +0.8, +0.8)	0.0037	0.0743
138	BBH:0328	(1, +0.8, +0.8)	0.0034	0.0733
139	BBH:2104	(1, +0.8, +0.8)	0.0033	0.0742
140	BBH:1481	(1, +0.8, +0.73)	0.0032	0.0839
141	BBH:0175	(1, +0.75, +0.75)	0.0030	0.0964
142	BBH:2106	(1, +0.9, +0.5)	0.0064	0.0441
143	BBH:1497	(1, +0.68, +0.67)	0.0032	0.1165
144	BBH:1495	(1, +0.78, +0.53)	0.0058	0.0698
145	BBH:0152	(1, +0.6, +0.6)	0.0047	0.1483
146	BBH:2099	(1, +0.8, +0.4)	0.0048	0.0790
147	BBH:2102	(1, +0.6, +0.6)	0.0007	0.1469
148	BBH:1123	(1, +0.5, +0.5)	0.0033	0.1899
149	BBH:0394	(1, +0.6, +0.4)	0.0023	0.0936
150	BBH:2103	(1, +0.65, +0.25)	0.0022	0.3458
151	BBH:2105	(1, +0.9, 0)	0.0002	0.0652
152	BBH:1122	(1, +0.44, +0.44)	0.0031	0.2051
153	BBH:1503	(1, +0.73, +0.14)	0.0028	0.1642
154	BBH:1501	(1, +0.75, +0.1)	0.0040	0.1363
155	BBH:0326	(1, +0.8, 0)	0.0056	0.1324
156	BBH:1507	(1, +0.5, +0.3)	0.0032	0.1965
157	BBH:1376	(1, +0.25, +0.5)	0.0035	0.2068
158	BBH:2101	(1, +0.6, 0)	0.0039	0.1777
159	BBH:0418	(1, +0.4, 0)	0.0041	0.1332
160	BBH:2095	(1, +0.8, -0.4)	0.0006	0.1245
161	BBH:2093	(1, +0.9, -0.5)	0.0018	0.1189
162	BBH:2097	(1, +0.3, 0)	0.0014	0.3091
163	BBH:1502	(1, +0.7, -0.4)	0.0026	0.0786
164	BBH:0366	(1, +0.2, 0)	0.0027	0.1055
165	BBH:1114	(1, +0.2, 0)	..	0.1452
166	BBH:0370	(1, +0.4, -0.2)	0.0006	0.4640
167	BBH:0376	(1, +0.6, -0.4)	0.0013	0.4585
168	BBH:1506	(1, +0.46, -0.3)	0.0023	0.1897
169	BBH:1476	(1, -0.8, +0.8)	0.0045	0.0926
170	BBH:2085	(1, -0.9, +0.9)	0.0021	0.0910
171	BBH:2087	(1, -0.8, +0.8)	0.0007	0.0932
172	BBH:0304	(1, -0.5, +0.5)	0.0014	0.2308
173	BBH:2091	(1, -0.6, +0.6)	0.0019	0.3086
174	BBH:2092	(1, +0.5, -0.5)	0.0028	0.3435
175	BBH:0327	(1, -0.8, +0.8)	0.0042	0.0457
176	BBH:0330	(1, -0.8, +0.8)	0.0005	0.0930
177	BBH:0459	(1, -0.4, +0.2)	0.0023	0.0359
178	BBH:0447	(1, -0.6, +0.4)	0.0054	0.2526
179	BBH:1351	(1, -0.23, 0)	0.0005	0.0813
180	BBH:2096	(1, -0.3, 0)	0.0005	0.1127
181	BBH:1509	(1, -0.24, -0.1)	0.0014	0.2097
182	BBH:2100	(1, -0.9, +0.5)	0.0017	0.0481
183	BBH:2098	(1, -0.8, +0.4)	0.0044	0.0475

TABLE X. This table continues to summarize the **SXS** NR waveform data in the *validation* set, with mass-ratios $1 \leq q \leq 1.2$. From left to right, the columns report: the SXS simulation number, mass ratio and dimensionless spins χ_i , and the maximum value of the unfaithfulness \bar{F} between: The two highest resolutions of the NR dataset, if available, see Fig.2, and between EOB and NR, see Fig. 4.

#	id	(q, χ_1, χ_2)	$\bar{F}_{\text{NR/NR}}^{\text{max}}[\%]$	$\bar{F}_{\text{EOB/NR}}^{\text{max}}[\%]$
184	BBH:0415	(1, -0.4, 0)	0.0021	0.1571
185	BBH:1499	(1, -0.75, +0.34)	0.0021	0.0440
186	BBH:1498	(1, +0.22, -0.8)	0.0093	0.0261
187	BBH:2090	(1, -0.6, 0)	0.0036	0.0464
188	BBH:0436	(1, -0.4, -0.2)	0.0019	0.1467
189	BBH:0585	(1, -0.6, 0)	0.0009	0.0863
190	BBH:0325	(1, -0.8, 0)	0.0022	0.1511
191	BBH:1134	(1, -0.44, -0.44)	0.0025	0.0383
192	BBH:1135	(1, -0.44, -0.44)	0.0047	0.0265
193	BBH:2088	(1, -0.62, -0.25)	0.0016	0.1088
194	BBH:1144	(1, -0.44, -0.44)	0.0054	0.0393
195	BBH:2084	(1, -0.9, 0)	0.0031	0.1176
196	BBH:1500	(1, -0.77, -0.2)	0.0012	0.0560
197	BBH:0462	(1, -0.6, -0.4)	0.0025	0.0454
198	BBH:0151	(1, -0.6, -0.6)	0.0022	0.1071
199	BBH:2094	(1, -0.8, -0.4)	0.0009	0.0999
200	BBH:2089	(1, -0.6, -0.6)	0.0072	0.0900
201	BBH:1492	(1, -0.8, -0.47)	0.0009	0.0756
202	BBH:2083	(1, -0.9, -0.5)	0.0067	0.0565
203	BBH:1475	(1, -0.8, -0.8)	0.0026	0.0468
204	BBH:2086	(1, -0.8, -0.8)	0.0033	0.0349
205	BBH:0329	(1, -0.8, -0.8)	0.0020	0.0509
206	BBH:1137	(1, -0.97, -0.97)	0.0021	0.1300
207	BBH:0544	(1, 0, +0.7)	0.0021	0.2125
208	BBH:0518	(1.1, -0.14, +0.43)	0.0012	0.1204
209	BBH:1513	(1.1, -0.1, 0)	0.0051	0.1661
210	BBH:0409	(1.2, +0.4, +0.8)	0.0058	0.1314
211	BBH:1490	(1.2, +0.41, +0.76)	0.0026	0.1835
212	BBH:1496	(1.2, +0.8, +0.03)	0.0008	0.1548
213	BBH:0311	(1.2, +0.42, +0.38)	0.0019	0.2521
214	BBH:0486	(1.2, 0, +0.8)	0.0024	0.1712
215	BBH:0559	(1.2, -0.2, +0.8)	0.0035	0.0903
216	BBH:0475	(1.2, -0.4, +0.8)	0.0036	0.0776
217	BBH:1352	(1.2, +0.71, -0.67)	0.0013	0.1645
218	BBH:0503	(1.2, -0.6, +0.8)	0.0017	0.0343
219	BBH:0312	(1.2, +0.4, -0.48)	0.0046	0.1594
220	BBH:1353	(1.2, +0.33, -0.44)	0.0013	0.3409
221	BBH:0309	(1.2, +0.33, -0.44)	0.0103	0.2187
222	BBH:0305	(1.2, +0.33, -0.44)	0.0015	0.1682
223	BBH:0318	(1.2, +0.33, -0.44)	0.0018	0.2182
224	BBH:0319	(1.2, +0.33, -0.44)	0.0096	0.1225
225	BBH:0313	(1.2, +0.38, -0.5)	0.0035	0.2190
226	BBH:0465	(1.2, +0.6, -0.8)	0.0010	0.1743
227	BBH:0314	(1.2, +0.31, -0.46)	0.0021	0.2401
228	BBH:0307	(1.2, +0.32, -0.58)	0.0016	0.1026
229	BBH:0626	(1.2, -0.83, +0.73)	0.0061	0.0217
230	BBH:0535	(1.2, +0.2, -0.8)	0.0023	0.0812
231	BBH:0523	(1.2, -0.2, -0.47)	0.0012	0.0362
232	BBH:0398	(1.2, 0, -0.8)	0.0036	0.0475
233	BBH:0386	(1.2, -0.2, -0.8)	0.0012	0.1080
234	BBH:0438	(1.2, -0.6, -0.8)	0.0021	0.0363

TABLE XI. This table summarizes the **SXS** NR waveform data in the *validation* set, with mass-ratios $1.3 \leq q \leq 1.7$. From left to right, the columns report: the SXS simulation number, mass ratio and dimensionless spins χ_i , and the maximum value of the unfaithfulness \bar{F} between: The two highest resolutions of the NR dataset, if available, see Fig.2, and between EOB and NR, see Fig. 4.

#	id	(q, χ_1, χ_2)	$\bar{F}_{\text{NR/NR}}^{\text{max}}[\%]$	$\bar{F}_{\text{EOB/NR}}^{\text{max}}[\%]$
235	BBH:0507	(1.3, +0.8, +0.4)	0.0043	0.1326
236	BBH:1493	(1.3, 0, +0.8)	0.0029	0.1639
237	BBH:0525	(1.3, +0.8, -0.4)	0.0008	0.1835
238	BBH:1505	(1.3, -0.1, +0.55)	0.0021	0.1400
239	BBH:0591	(1.2, 0, +0.4)	0.0028	0.0926
240	BBH:1508	(1.3, +0.3, -0.07)	0.0057	0.1296
241	BBH:1474	(1.3, +0.72, -0.8)	0.0025	0.2317
242	BBH:1223	(1.2, +0.38, -0.46)	0.0034	0.1685
243	BBH:0651	(1.3, 0, +0.03)	0.0051	0.1191
244	BBH:0650	(1.3, 0, +0.03)	0.0141	0.3692
245	BBH:0315	(1.3, +0.32, -0.56)	0.0011	0.3037
246	BBH:0464	(1.2, 0, -0.4)	0.0013	0.1014
247	BBH:1487	(1.3, -0.8, +0.5)	0.0022	0.0636
248	BBH:0377	(1.3, -0.8, +0.4)	0.0017	0.0739
249	BBH:0466	(1.3, -0.8, -0.4)	0.0006	0.0388
250	BBH:1471	(1.3, -0.78, -0.8)	0.0009	0.0561
251	BBH:0129	(1.4, +0.09, -0.07)	..	0.1464
252	BBH:1482	(1.4, -0.58, +0.8)	0.0016	0.0301
253	BBH:0625	(1.4, -0.71, +0.22)	0.0046	0.0519
254	BBH:1146	(1.5, +0.95, +0.95)	0.0446	0.8427
255	BBH:1473	(1.4, +0.7, +0.8)	0.0060	0.1843
256	BBH:0441	(1.5, +0.6, +0.8)	0.0034	0.1585
257	BBH:0385	(1.5, +0.8, 0)	0.0016	0.1737
258	BBH:0361	(1.5, 0, +0.8)	0.0025	0.1085
259	BBH:0372	(1.5, +0.8, -0.4)	0.0025	0.1282
260	BBH:0499	(1.5, +0.01, +0.74)	0.0041	0.1005
261	BBH:0009	(1.5, +0.5, 0)	..	0.2536
262	BBH:0392	(1.5, -0.2, +0.8)	0.0024	0.0555
263	BBH:0440	(1.5, 0, +0.4)	0.0014	0.0512
264	BBH:0369	(1.5, +0.6, -0.8)	0.0026	0.3375
265	BBH:1511	(1.5, +0.03, -0.1)	0.0024	0.0952
266	BBH:0579	(1.5, +0.4, -0.8)	0.0022	0.0881
267	BBH:0012	(1.5, -0.5, 0)	0.0068	0.0341
268	BBH:0014	(1.5, -0.5, 0)	0.0561	0.0425
269	BBH:0101	(1.5, -0.5, 0)	..	0.0284
270	BBH:0404	(1.5, 0, -0.8)	0.0032	0.0962
271	BBH:0437	(1.5, -0.2, -0.8)	0.0019	0.0552
272	BBH:1480	(1.5, -0.8, -0.3)	0.0035	0.0304
273	BBH:0397	(1.5, -0.8, -0.4)	0.0017	0.0419
274	BBH:1470	(1.5, -0.73, -0.8)	0.0035	0.0345
275	BBH:0519	(1.6, +0.64, +0.4)	0.0048	0.0812
276	BBH:1488	(1.6, -0.33, +0.75)	0.0061	0.0357
277	BBH:1479	(1.6, -0.56, -0.8)	0.0016	0.0380
278	BBH:0501	(1.7, +0.6, +0.8)	0.0063	0.1260
279	BBH:0435	(1.7, +0.4, +0.8)	0.0029	0.0817
280	BBH:0566	(1.7, +0.2, +0.8)	0.0041	0.0971
281	BBH:0382	(1.7, 0, +0.8)	0.0017	0.0701
282	BBH:0529	(1.7, 0, +0.53)	0.0035	0.0627
283	BBH:0550	(1.7, -0.2, +0.8)	0.0021	0.0534
284	BBH:0451	(1.7, 0, +0.4)	0.0022	0.0526
285	BBH:0488	(1.7, +0.6, -0.8)	0.0040	0.2618

TABLE XII. This table continues to summarize the SXS NR waveform data in the *validation* set, with mass-ratios $1.7 \leq q \leq 2$. From left to right, the columns report: the SXS simulation number, mass ratio and dimensionless spins χ_i , and the maximum value of the unfaithfulness \bar{F} between: The two highest resolutions of the NR dataset, if available, see Fig.2, and between EOB and NR, see Fig. 4.

#	id	(q, χ_1, χ_2)	$\bar{F}_{\text{NR/NR}}^{\text{max}}[\%]$	$\bar{F}_{\text{EOB/NR}}^{\text{max}}[\%]$
286	BBH:0678	(1.7, 0, +0.03)	0.0073	0.1337
287	BBH:0677	(1.7, 0, +0.03)	0.0037	0.1791
288	BBH:0676	(1.7, 0, +0.02)	0.0050	0.3450
289	BBH:0355	(1.7, -0.6, +0.8)	0.0015	0.0550
290	BBH:1491	(1.7, +0.2, -0.7)	0.0020	0.0999
291	BBH:0473	(1.7, +0.2, -0.8)	0.0019	0.0876
292	BBH:1465	(1.7, -0.79, +0.77)	0.0038	0.0740
293	BBH:0510	(1.7, -0.02, -0.75)	0.0044	0.0639
294	BBH:0423	(1.7, 0, -0.8)	0.0008	0.0577
295	BBH:0402	(1.7, -0.8, +0.4)	0.0017	0.0725
296	BBH:0414	(1.7, -0.4, -0.8)	0.0038	0.0438
297	BBH:0512	(1.7, -0.6, -0.8)	0.0006	0.0476
298	BBH:0388	(1.8, +0.8, +0.4)	0.0034	0.1265
299	BBH:0552	(1.8, +0.8, -0.4)	0.0016	0.2418
300	BBH:1510	(1.8, +0.03, +0.3)	0.0018	0.0549
301	BBH:0371	(1.8, 0, -0.4)	0.0060	0.0532
302	BBH:0545	(1.8, 0, -0.8)	0.0026	0.0306
303	BBH:0454	(1.8, -0.8, -0.4)	0.0011	0.0203
304	BBH:1469	(1.9, +0.8, +0.67)	0.0042	0.1686
305	BBH:0530	(2, 0, +0.54)	0.0015	0.0449
306	BBH:1466	(1.9, +0.7, -0.8)	0.0015	0.2468
307	BBH:0555	(1.9, 0, +0.53)	0.0008	0.0483
308	BBH:0368	(2, -0.05, +0.25)	0.0015	0.0351
309	BBH:0403	(1.9, 0, -0.05)	0.0048	0.0442
310	BBH:0580	(2, +0.02, -0.8)	0.0020	0.0756
311	BBH:2131	(2, +0.85, +0.85)	0.0011	0.3993
312	BBH:0333	(2, +0.8, +0.8)	0.0115	0.2591
313	BBH:2130	(2, +0.6, +0.6)	0.0032	0.0779
314	BBH:1478	(2, +0.8, +0.13)	0.0047	0.1406
315	BBH:2127	(2, +0.5, +0.5)	0.0102	0.0819
316	BBH:1148	(2, +0.43, +0.5)	0.0048	0.0890
317	BBH:0410	(2, +0.6, 0)	0.0047	0.2876
318	BBH:0574	(2, +0.4, +0.4)	0.0016	0.1062
319	BBH:2129	(2, +0.6, 0)	0.0016	0.1325
320	BBH:2122	(2, +0.13, +0.85)	0.0022	0.0672
321	BBH:2125	(2, +0.3, +0.3)	0.0017	0.0784
322	BBH:2132	(2, +0.87, -0.85)	0.0039	0.4141
323	BBH:0399	(2, +0.2, +0.4)	0.0013	0.0681
324	BBH:0332	(2, 0, +0.8)	0.0021	0.0495
325	BBH:0513	(2, +0.6, -0.4)	0.0030	0.1416
326	BBH:2128	(2, +0.6, -0.6)	0.0051	0.1713
327	BBH:2121	(2, 0, +0.6)	0.0017	0.0426
328	BBH:2124	(2, +0.3, 0)	0.0014	0.0793
329	BBH:0903	(2, 0, +0.6)	0.0009	0.0697
330	BBH:0893	(2, 0, +0.58)	0.0020	0.0621
331	BBH:0885	(2, 0, +0.57)	0.0024	0.1064
332	BBH:1504	(2, +0.25, +0.08)	0.0013	0.0726
333	BBH:0448	(2, +0.4, -0.4)	0.0031	0.1224
334	BBH:0407	(2, 0, +0.4)	0.0020	0.0394
335	BBH:0599	(2, +0.2, 0)	0.0027	0.0698
336	BBH:1147	(2, +0.43, -0.5)	0.0094	0.1338

TABLE XIII. This table continues to summarize the SXS NR waveform data in the *validation* set, with mass-ratios $2 \leq q \leq 2.6$. From left to right, the columns report: the SXS simulation number, mass ratio and dimensionless spins χ_i , and the maximum value of the unfaithfulness \bar{F} between: The two highest resolutions of the NR dataset, if available, see Fig.2, and between EOB and NR, see Fig. 4.

#	id	(q, χ_1, χ_2)	$\bar{F}_{\text{NR/NR}}^{\text{max}}[\%]$	$\bar{F}_{\text{EOB/NR}}^{\text{max}}[\%]$
337	BBH:2120	(2, 0, +0.3)	0.0013	0.0368
338	BBH:2123	(2, +0.3, -0.3)	0.0021	0.1055
339	BBH:2113	(2, -0.37, +0.85)	0.0012	0.0344
340	BBH:0913	(2, 0, +0.03)	0.0034	0.0802
341	BBH:0971	(2, 0, +0.03)	0.0010	0.0460
342	BBH:0987	(2, 0, +0.03)	0.0080	0.0745
343	BBH:0703	(2, 0, +0.03)	0.0085	0.1011
344	BBH:0704	(2, 0, +0.03)	0.0007	0.0949
345	BBH:0921	(2, 0, +0.03)	0.0021	0.1244
346	BBH:0702	(2, 0, +0.02)	0.0038	0.2062
347	BBH:0961	(2, 0, +0.02)	0.0011	0.1312
348	BBH:0979	(2, 0, +0.02)	0.0068	0.2057
349	BBH:0931	(2, 0, +0.0)	0.0034	0.1406
350	BBH:0554	(2, +0.2, -0.4)	0.0029	0.0954
351	BBH:0354	(2, -0.2, +0.4)	0.0006	0.0234
352	BBH:2126	(2, +0.37, -0.85)	0.0031	0.1498
353	BBH:0482	(2, -0.02, -0.13)	0.0040	0.0409
354	BBH:2119	(2, 0, -0.3)	0.0034	0.0466
355	BBH:2116	(2, -0.3, +0.3)	0.0027	0.0208
356	BBH:1112	(2, -0.2, 0)	..	0.0227
357	BBH:0375	(2, 0, -0.4)	0.0013	0.0204
358	BBH:0954	(2, 0, -0.56)	0.0031	0.0784
359	BBH:0947	(2, 0, -0.56)	0.0056	0.1312
360	BBH:0940	(2, 0, -0.57)	0.0040	0.1698
361	BBH:2118	(2, 0, -0.6)	0.0025	0.0617
362	BBH:2111	(2, -0.6, +0.6)	0.0017	0.0882
363	BBH:2115	(2, -0.3, 0)	0.0038	0.0223
364	BBH:0331	(2, 0, -0.8)	0.0075	0.0668
365	BBH:0412	(2, -0.2, -0.4)	0.0018	0.0295
366	BBH:0335	(2, -0.8, +0.8)	0.0012	0.1186
367	BBH:2107	(2, -0.87, +0.85)	0.0012	0.1700
368	BBH:2114	(2, -0.3, -0.3)	0.0021	0.0234
369	BBH:2117	(2, -0.13, -0.85)	0.0057	0.0642
370	BBH:2110	(2, -0.6, 0)	0.0021	0.0435
371	BBH:0584	(2, -0.4, -0.4)	0.0027	0.0260
372	BBH:0461	(2, -0.6, 0)	0.0018	0.0318
373	BBH:2112	(2, -0.5, -0.5)	0.0031	0.0256
374	BBH:0387	(2, -0.6, -0.4)	0.0022	0.0239
375	BBH:2109	(2, -0.6, -0.6)	0.0015	0.0273
376	BBH:0334	(2, -0.8, -0.8)	0.0033	0.0519
377	BBH:2108	(2, -0.85, -0.85)	0.0068	0.0766
378	BBH:1467	(2.2, -0.56, +0.8)	0.0051	0.0538
379	BBH:1494	(2.2, -0.47, -0.4)	0.0025	0.0303
380	BBH:1459	(2.3, +0.76, +0.8)	0.0112	0.1404
381	BBH:1468	(2.3, +0.51, +0.8)	0.0068	0.0635
382	BBH:0631	(2.3, -0.13, -0.36)	0.0036	0.0161
383	BBH:1453	(2.4, +0.8, -0.8)	0.0048	0.1916
384	BBH:1512	(2.4, +0.24, 0)	0.0045	0.0639
385	BBH:1472	(2.4, -0.8, -0.1)	0.0022	0.0243
386	BBH:1454	(2.5, -0.8, -0.73)	0.0030	0.0733
387	BBH:1462	(2.6, -0.8, +0.5)	0.0021	0.0714

TABLE XIV. This table summarizes the *SXS* NR waveform data in the *validation* set, with mass-ratios $2.9 \leq q \leq 3$. From left to right, the columns report: the *SXS* simulation number, mass ratio and dimensionless spins χ_i , and the maximum value of the unfaithfulness \bar{F} between: The two highest resolutions of the NR dataset, if available, see Fig.2, and between EOB and NR, see Fig. 4.

#	id	(q, χ_1, χ_2)	$\bar{F}_{\text{NR/NR}}^{\text{max}}[\%]$	$\bar{F}_{\text{EOB/NR}}^{\text{max}}[\%]$
388	BBH:1461	(2.9, -0.45, -0.8)	0.0044	0.0299
389	BBH:1484	(3, -0.56, +0.3)	0.0019	0.0399
390	BBH:1456	(3, +0.74, +0.7)	0.0123	0.0528
391	BBH:1150	(3, +0.7, +0.6)	0.0088	0.0176
392	BBH:1151	(3, +0.7, +0.6)	0.0093	0.0214
393	BBH:1152	(3, +0.7, +0.6)	0.0079	0.0214
394	BBH:1382	(3, +0.7, +0.6)	0.0072	0.0298
395	BBH:2163	(3, +0.6, +0.6)	0.0029	0.0135
396	BBH:2162	(3, +0.6, +0.4)	0.0020	0.0270
397	BBH:2158	(3, +0.5, +0.5)	0.0089	0.0201
398	BBH:0047	(3, +0.5, +0.5)	..	0.0212
399	BBH:2161	(3, +0.6, 0)	0.0052	0.0673
400	BBH:2157	(3, +0.4, +0.6)	0.0043	0.0256
401	BBH:2152	(3, +0.27, +0.85)	0.0047	0.0392
402	BBH:0031	(3, +0.5, 0)	0.0244	0.0679
403	BBH:0041	(3, +0.5, 0)	..	0.0571
404	BBH:2160	(3, +0.6, -0.4)	0.0058	0.1463
405	BBH:2159	(3, +0.6, -0.6)	0.0034	0.1960
406	BBH:2155	(3, +0.3, +0.3)	0.0048	0.0240
407	BBH:1387	(3, +0.47, -0.36)	0.0026	0.1079
408	BBH:2154	(3, +0.3, 0)	0.0081	0.0451
409	BBH:2156	(3, +0.4, -0.6)	0.0009	0.1299
410	BBH:2150	(3, 0, +0.6)	0.0022	0.0253
411	BBH:2153	(3, +0.3, -0.3)	0.0013	0.0719
412	BBH:2149	(3, 0, +0.3)	0.0025	0.0201
413	BBH:2146	(3, -0.23, +0.85)	0.0038	0.0354
414	BBH:2151	(3, +0.23, -0.85)	0.0014	0.0671
415	BBH:2148	(3, 0, -0.3)	0.0049	0.0373
416	BBH:2144	(3, -0.3, +0.3)	0.0032	0.0312
417	BBH:2141	(3, -0.4, +0.6)	0.0030	0.0658
418	BBH:2147	(3, 0, -0.6)	0.0045	0.0251
419	BBH:2143	(3, -0.3, 0)	0.0035	0.0232
420	BBH:2135	(3, -0.6, +0.6)	0.0026	0.1012
421	BBH:2142	(3, -0.3, -0.3)	0.0009	0.0249
422	BBH:2133	(3, -0.73, +0.85)	0.0023	0.1467
423	BBH:2138	(3, -0.6, +0.4)	0.0020	0.0748
424	BBH:0038	(3, -0.5, 0)	..	0.0276
425	BBH:0039	(3, -0.5, 0)	..	0.0271
426	BBH:0040	(3, -0.5, 0)	..	0.0224
427	BBH:2145	(3, -0.27, -0.85)	0.0044	0.0611
428	BBH:2140	(3, -0.4, -0.6)	0.0019	0.0239
429	BBH:2134	(3, -0.6, 0)	0.0023	0.0388
430	BBH:0046	(3, -0.5, -0.5)	..	0.0358
431	BBH:2139	(3, -0.5, -0.5)	0.0029	0.0363
432	BBH:2137	(3, -0.6, -0.4)	0.0019	0.0330
433	BBH:2136	(3, -0.6, -0.6)	0.0020	0.0432
434	BBH:1172	(3, -0.7, -0.6)	0.0021	0.0493
435	BBH:1170	(3, -0.7, -0.6)	0.0021	0.0739
436	BBH:1171	(3, -0.7, -0.6)	0.0024	0.0543
437	BBH:1173	(3, -0.7, -0.6)	0.0013	0.0515
438	BBH:1174	(3, -0.7, -0.6)	0.0004	0.0515

TABLE XV. This table summarizes the *SXS* NR waveform data in the *validation* set, with mass-ratios $3 \leq q \leq 5.5$. From left to right, the columns report: the *SXS* simulation number, mass ratio and dimensionless spins χ_i , and the maximum value of the unfaithfulness \bar{F} between: The two highest resolutions of the NR dataset, if available, see Fig.2, and between EOB and NR, see Fig. 4.

#	id	(q, χ_1, χ_2)	$\bar{F}_{\text{NR/NR}}^{\text{max}}[\%]$	$\bar{F}_{\text{EOB/NR}}^{\text{max}}[\%]$
439	BBH:1175	(3, -0.7, -0.6)	0.0022	0.0514
440	BBH:1485	(3, +0.35, -0.4)	0.0046	0.0889
441	BBH:1447	(3.2, +0.74, +0.8)	..	0.0558
442	BBH:1457	(3.2, +0.54, +0.8)	0.0095	0.0216
443	BBH:1483	(3.2, +0.56, -0.2)	0.0059	0.0849
444	BBH:1446	(3.2, -0.8, +0.78)	0.0047	0.1088
445	BBH:0317	(3.3, +0.52, -0.45)	0.0040	0.1162
446	BBH:1489	(3.5, +0.3, -0.17)	..	0.0459
447	BBH:1452	(3.6, +0.8, -0.43)	..	0.1924
448	BBH:1486	(3.7, +0.43, -0.03)	0.0038	0.0328
449	BBH:1458	(3.8, -0.06, +0.8)	0.0047	0.0271
450	BBH:2014	(4, +0.8, +0.4)	..	0.1195
451	BBH:1938	(4, +0.4, +0.8)	0.0102	0.0634
452	BBH:1417	(4, +0.4, +0.5)	0.0565	0.0745
453	BBH:1937	(4, +0.4, 0)	0.0031	0.0228
454	BBH:1942	(4, +0.4, -0.8)	0.0078	0.1199
455	BBH:1907	(4, 0, +0.8)	0.0072	0.0256
456	BBH:2041	(4, 0, +0.6)	0.0080	0.0483
457	BBH:2051	(4, 0, +0.6)	0.0068	0.0530
458	BBH:2047	(4, 0, +0.6)	0.0060	0.0495
459	BBH:2013	(4, 0, +0.4)	0.0023	0.0248
460	BBH:1910	(4, 0, +0.03)	0.0128	0.0473
461	BBH:2068	(4, 0, +0.04)	0.0060	0.0476
462	BBH:1908	(4, 0, +0.0)	0.0051	0.0589
463	BBH:2072	(4, 0, +0.0)	0.0110	0.0391
464	BBH:1909	(4, 0, +0.0)	0.0047	0.0260
465	BBH:2077	(4, 0, +0.0)	0.0071	0.0185
466	BBH:2036	(4, 0, -0.4)	0.0035	0.0356
467	BBH:2063	(4, 0, -0.55)	0.0055	0.0652
468	BBH:2056	(4, 0, -0.56)	0.0057	0.0667
469	BBH:2060	(4, 0, -0.57)	0.0041	0.0490
470	BBH:1911	(4, 0, -0.8)	0.0070	0.0690
471	BBH:1962	(4, -0.4, +0.8)	0.0039	0.0746
472	BBH:1961	(4, -0.4, 0)	0.0011	0.0231
473	BBH:1418	(4, -0.4, -0.5)	0.0526	0.0554
474	BBH:1966	(4, -0.4, -0.8)	0.0020	0.0309
475	BBH:1932	(4, -0.8, +0.8)	0.0021	0.1056
476	BBH:2018	(4, -0.8, +0.4)	0.0021	0.0561
477	BBH:1931	(4, -0.8, 0)	0.0004	0.0297
478	BBH:2040	(4, -0.8, -0.4)	0.0006	0.0414
479	BBH:1936	(4, -0.8, -0.8)	0.0091	0.1059
480	BBH:1451	(4, +0.31, -0.8)	0.0070	0.0637
481	BBH:1450	(4, -0.28, -0.8)	0.0020	0.0377
482	BBH:1449	(4.2, -0.8, -0.34)	0.0026	0.0392
483	BBH:1434	(4.4, +0.8, +0.8)	..	0.0347
484	BBH:1445	(4.7, -0.5, +0.8)	0.0058	0.1449
485	BBH:1463	(5, +0.61, +0.24)	0.0032	0.1126
486	BBH:0061	(5, +0.5, 0)	..	0.0403
487	BBH:0109	(5, -0.5, 0)	..	0.0404
488	BBH:1111	(5, -0.9, 0)	0.0071	0.0436
489	BBH:1428	(5.5, -0.8, -0.7)	0.0066	0.0691

TABLE XVI. This table summarizes the SXS NR waveform data in the *validation* set, with mass-ratios $5.6 \leq q \leq 8$. From left to right, the columns report: the SXS simulation number, mass ratio and dimensionless spins χ_i , and the maximum value of the unfaithfulness \bar{F} between: The two highest resolutions of the NR dataset, if available, see Fig.2, and between EOB and NR, see Fig. 4.

#	id	(q, χ_1, χ_2)	$\bar{F}_{\text{NR/NR}}^{\text{max}}[\%]$	$\bar{F}_{\text{EOB/NR}}^{\text{max}}[\%]$
490	BBH:1440	(5.6, +0.77, +0.3)	0.0055	0.3153
491	BBH:1443	(5.7, +0.4, -0.74)	0.0064	0.0238
492	BBH:1432	(5.8, +0.66, +0.8)	0.0192	0.3279
493	BBH:1438	(5.9, +0.13, +0.8)	0.0081	0.0467
494	BBH:1444	(6, -0.06, -0.76)	0.0164	0.0329
495	BBH:1437	(6, +0.8, +0.15)	0.0141	0.3749
496	BBH:1425	(6.1, -0.8, +0.67)	0.0098	0.1078
497	BBH:1436	(6.3, 0, -0.8)	0.0142	0.0363
498	BBH:1439	(6.5, +0.72, -0.3)	..	0.4042
499	BBH:1464	(6.5, -0.05, -0.32)	0.0057	0.0196
500	BBH:1424	(6.5, -0.66, -0.8)	0.0134	0.0509
501	BBH:1442	(6.6, -0.7, -0.18)	0.0018	0.0266
502	BBH:1435	(6.6, -0.79, +0.07)	0.0081	0.0284
503	BBH:1448	(7, -0.48, +0.52)	..	0.0872
504	BBH:0204	(7, +0.4, 0)	0.0434	0.0697
505	BBH:0206	(7, -0.4, 0)	0.0171	0.0649
506	BBH:1427	(7.4, -0.61, -0.73)	0.0050	0.0389
507	BBH:1429	(7.7, -0.2, -0.78)	0.0049	0.0286
508	BBH:1421	(7.8, -0.6, +0.8)	0.0046	0.1319
509	BBH:1426	(8, +0.48, +0.75)	0.0378	0.1978
510	BBH:1441	(8, +0.6, -0.48)	..	0.2876
511	BBH:1430	(8, +0.28, -0.75)	0.0302	0.0180
512	BBH:1431	(8, +0.08, -0.78)	0.0153	0.0301
513	BBH:1455	(8, -0.4, 0)	0.0023	0.0340
514	BBH:0114	(8, -0.5, 0)	..	0.0345
515	BBH:1423	(8, -0.6, -0.75)	0.0103	0.0388
516	BBH:1420	(8, -0.8, +0.8)	0.0094	0.1288
517	BBH:1433	(8, -0.74, +0.2)	0.0037	0.0500
518	BBH:1422	(8, -0.8, -0.46)	0.0060	0.0493
519	BBH:1419	(8, -0.8, -0.8)	..	0.0701

angle in the source frame. Each multipole is decomposed in amplitude $A_{\ell m}$ and a phase $\phi_{\ell m}$ as

$$h_{\ell m} = A_{\ell m} e^{i\phi_{\ell m}}. \quad (\text{C4})$$

The instantaneous GW frequency $\omega_{\ell m}$ is defined as

$$\omega_{\ell m} \equiv -\dot{\phi}_{\ell m}, \quad (\text{C5})$$

where the dot indicate the time derivative. Motivated by the leading-order analytical behavior of each multipole, we introduce the following rescaled multipolar am-

plitudes $\hat{A}_{\ell m}$:

$$\hat{A}_{22} \equiv A_{22} / \left[\nu \left(1 - \hat{S}\omega_{22} \right) \right], \quad (\text{C6})$$

$$\hat{A}_{21} \equiv A_{21} / \nu, \quad (\text{C7})$$

$$\hat{A}_{33} \equiv A_{33} / \nu, \quad (\text{C8})$$

$$\hat{A}_{32} \equiv A_{32} / \left[\nu \left(1 - \tilde{a}_0 (\omega_{32}/2)^{1/3} \right) \right], \quad (\text{C9})$$

$$\hat{A}_{44} \equiv A_{44} / \left[\nu \left(1 - \frac{1}{2} \hat{S}\omega_{44} \right) \right], \quad (\text{C10})$$

$$\hat{A}_{43} \equiv A_{43} / \nu, \quad (\text{C11})$$

$$\hat{A}_{42} \equiv A_{42} / \left[\nu \left(1 - \tilde{a}_0 (\omega_{42}/2)^{1/3} \right) \right]. \quad (\text{C12})$$

Then one defines the time where each (ℓ, m) mode peaks as

$$t_{\ell m}^{\text{peak}} \equiv t \left(\max \left[\hat{A}_{\ell m} \right] \right), \quad (\text{C13})$$

and the merger time, that is defined as the peak of the $(2, 2)$ mode, i.e.

$$t^{\text{mrg}} \equiv t_{22}^{\text{peak}}. \quad (\text{C14})$$

One then defines the time-delay between merger time and the time where each mode peak, as

$$\Delta t_{\ell m} \equiv t_{\ell m}^{\text{peak}} - t^{\text{mrg}} \quad (\text{C15})$$

For shortness, we denote quantities calculated at a given time using the corresponding superscript, e.g.

$$\hat{A}_{\ell m}^{\text{peak}} \equiv \hat{A}_{\ell m} \left(t_{\ell m}^{\text{peak}} \right). \quad (\text{C16})$$

Let us now give all details on a mode-by-mode basis.

a. $(\ell, m) = (2, 2)$ multipole

We start by describing the template with which ω_{22}^{mrg} and $\hat{A}_{22}^{\text{mrg}}$ were fitted. The same structure is used both for the amplitude and frequency at merger. We here present it explicitly for ω_{22}^{mrg} , while the same for $\hat{A}_{22}^{\text{mrg}}$ is obtained by suitably changing the coefficient labels. The frequency at merger ω_{22}^{mrg} is factorized as

$$\omega_{22}^{\text{mrg}} = \omega_{22}^{\text{mrg}0} \omega_{22}^{\text{orb}}(\nu) \omega_{22}^{\hat{S}}(\hat{S}, X_{12}), \quad (\text{C17})$$

where $\omega_{22}^{\text{mrg}0}$ is the value of the merger frequency obtained from a nonspinning test-particle waveform (see e.g. Table 3 of [44]). The nonspinning ν -dependence is then introduced by fitting the nonspinning data with a template of the form

$$\omega_{22}^{\text{orb}}(\nu) = 1 + a_1^\omega \nu + a_2^\omega \nu^2, \quad (\text{C18})$$

where the coefficients a_i^ω are determined using 19 nonspinning SXS waveforms with mass ratios $1 \leq m_1/m_2 \leq$

TABLE XVII. This table summarizes the *long-inspiral* SXS NR waveform data. From left to right, columns report: the SXS simulation number, mass ratio and dimensionless spins $\chi_{1,2}$, number of orbits N , eccentricity ϵ and the maximum value of the unfaithfulness \bar{F} computed between the highest and second highest resolution available $\bar{F}_{\text{NR/NR}}^{\text{max}}$ and between EOB waveform and the NR highest resolution $\bar{F}_{\text{EOB/NR}}^{\text{max}}$. These datasets are part of the *validation* set, while the in depth study of the other waveforms is left for future work. These waveforms are discussed in Section III C.

#	id	(q, χ_1, χ_2)	N	$\epsilon [10^{-3}]$	$\bar{F}_{\text{NR/NR}}^{\text{max}} [\%]$	$\bar{F}_{\text{EOB/NR}}^{\text{max}} [\%]$
520	SXS:BBH:1412	(1.63, +0.40, -0.30)	145.1	0.4450	0.7295	0.1266
521	SXS:BBH:1413	(1.41, +0.50, +0.40)	145.4	< 1.0	1.1856	0.1585
522	SXS:BBH:1414	(1.83, -0.50, +0.40)	143.1	< 1.6	0.8919	0.1965
523	SXS:BBH:1415	(1.50, +0.50, +0.50)	147.7	< 0.043	1.5238	0.1453
524	SXS:BBH:1416	(1.78, -0.40, -0.40)	139.0	< 1.7	0.5986	0.0468

10. The spin dependence is introduced in two steps: first one accurately fits the spin-dependence of equal-mass data. Then, additional flexibility to incorporate the spinning, unequal-mass data is introduced. More precisely the equal-mass, spin-dependence is obtained with

$$\omega_{22}^{\hat{S}}(\hat{S}, X_{12} = 0) = \frac{1 + b_1^{\omega_{m_1=m_2}} \hat{S} + b_2^{\omega_{m_1=m_2}} \hat{S}^2}{1 + b_3^{\omega_{m_1=m_2}} \hat{S}}, \quad (\text{C19})$$

which is informed by 39 equal-mass, spin-aligned, SXS waveforms. The additional dependence on mass ratio is incorporated substituting into Eq. (C19)

$$b_i^{\omega_{m_1=m_2}} \rightarrow \frac{b_i^{\omega_{m_1=m_2}} + c_{i1}^{\omega} X_{12}}{1 + c_{i2}^{\omega} X_{12}}, \quad (\text{C20})$$

with $i = \{1, 3\}$. where the additional coefficients c_{ij} are fitted using test-particle data, 77 additional SXS spinning waveforms and 14 additional NR waveforms from BAM. The coefficients are explicitly given in Table XX.

b. $(\ell, m) = (2, 1)$ multipole

The procedure followed for the subdominant modes is similar to what is done for the $(2, 2)$. There are however some differences. First of all, the peak time shift $\Delta t_{\ell m}$ is also fitted to NR simulations. Second, basing ourselves to the analytical behavior of the multipolar waveform, we have decided to use different factorizations and different variables to model each mode. For example, the $(2, 1)$ multipole (and every m -odd mode) vanishes because of symmetry in the equal-mass equal-spin case. This has brought us to consider the following factorization for $\hat{A}_{21}^{\text{peak}}$, which is written as

$$\hat{A}_{21}^{\text{peak}} = \hat{A}_{21}^{\text{peak}_0} X_{12} \hat{A}_{21}^{\text{orb}}(\nu) + \hat{A}_{21}^{\text{Spin}}(\bar{S}, \nu). \quad (\text{C21})$$

where $\hat{A}_{21}^{\text{peak}_0}$ is the peak amplitude in the test-particle limit. The factor $\hat{A}_{21}^{\text{orb}}$ is informed by non-spinning waveforms and is fitted with the template

$$\hat{A}_{21}^{\text{orb}}(\nu) = \frac{1 + a_1^{\hat{A}_{21}} \nu + a_2^{\hat{A}_{21}} \nu^2}{1 + a_3^{\hat{A}_{21}} \nu}. \quad (\text{C22})$$

The spin dependence is first captured in the test-particle limit with the function

$$\hat{A}_{21}^{\text{Spin}}(\bar{S}, \nu = 0) = \frac{1 + b_1^{\hat{A}_{21}^0} \bar{S} + b_2^{\hat{A}_{21}^0} \bar{S}^2}{1 + b_3^{\hat{A}_{21}^0} \bar{S}}. \quad (\text{C23})$$

The ν -dependence is then modeled via the replacement

$$b_i^{\hat{A}_{21}^0} \rightarrow b_i^{\hat{A}_{21}^0} + c_{i1}^{\hat{A}_{21}} \nu + c_{i2}^{\hat{A}_{21}} \nu^2, \quad (\text{C24})$$

with $i = \{1, 2, 3\}$.

The gravitational wave frequency ω_{21} is instead factorized as

$$\omega_{21}^{\text{peak}} = \omega_{21}^{\text{peak}_0} \omega_{21}^{\text{orb}}(\nu) \omega_{21}^{\text{Spin}}(\hat{S}, \nu), \quad (\text{C25})$$

where the ν -dependence of the nonspinning part is modeled as

$$\omega_{21}^{\text{orb}}(\nu) = 1 + a_1^{\omega_{21}} \nu + a_2^{\omega_{21}} \nu^2. \quad (\text{C26})$$

The spin dependence is fitted first in the test-particle limit

$$\omega_{21}^{\text{Spin}}(\hat{S}, \nu = 0) = 1 + b_1^{\omega_{21}^0} \hat{S} + b_2^{\omega_{21}^0} \hat{S}^2, \quad (\text{C27})$$

and then extended to a general mass ratio via the replacement

$$b_i^{\omega_{21}^0} \rightarrow b_i^{\omega_{21}^0} + c_i^{\omega_{21}} \nu, \quad (\text{C28})$$

with $i = \{1, 2\}$.

Finally, to represent analytically the time-delay Δt_{21} we use

$$\Delta t_{21} = \Delta t_{21}^{\text{orb}}(\nu) \Delta t_{21}^{\text{Spin}}(\bar{S}, X_{12}), \quad (\text{C29})$$

where the orbital behavior is factorized into two separate parts before fitting with

$$\Delta t_{21}^{\text{orb}}(\nu) = \left(\Delta t_{21}^0 (1 - 4\nu) + \Delta t_{21}^{\nu=1/4} 4\nu \right) \times \left(1 + a_1^{\Delta t_{21}} \nu \sqrt{1 - 4\nu} \right). \quad (\text{C30})$$

TABLE XVIII. The waveforms $1' - 22'$ have been used in Ref. [30] to inform the nonspinning sector. Waveforms $23' - 45'$ are the first part of the validation set and span mass-ratios $1 \leq q \leq 1.8$. EOB waveforms are computed with $\chi_1 = 0$ and $\chi_2 = 10^{-4}$. This comparison demonstrates the robustness of the spinning-sector of `TEOBiResumS_SM` in the nonspinning limit and the consistency with `TEOBiResumMultipoles` when spins are small. From left to right, the columns report: the SXS simulation number, mass ratio and dimensionless spins χ_i , and the maximum value of the unfaithfulness \bar{F} between: the two highest resolutions of the NR dataset, if available, see Fig. 20(left panel), and between EOB and NR, see Fig. 20(right panel).

#	id	(q, χ_1, χ_2)	$\bar{F}_{\text{NR/NR}}^{\text{max}} [\%]$	$\bar{F}_{\text{EOB/NR}}^{\text{max}} [\%]$
1'	BBH:0180	(1, 0, 0)	0.0035	0.0873
2'	BBH:0007	(1.5, 0, 0)	0.0020	0.0851
3'	BBH:0169	(2, 0, 0)	0.0032	0.0825
4'	BBH:0259	(2.5, 0, 0)	0.0050	0.0840
5'	BBH:0030	(3, 0, 0)	0.0030	0.0497
6'	BBH:0167	(4, 0, 0)	0.0057	0.0326
7'	BBH:0295	(4.5, 0, 0)	0.0066	0.0247
8'	BBH:0056	(5, 0, 0)	0.0158	0.0197
9'	BBH:0296	(5.5, 0, 0)	0.0177	0.0186
10'	BBH:0166	(6, 0, 0)	..	0.0176
11'	BBH:0297	(6.5, 0, 0)	0.0069	0.0167
12'	BBH:0298	(7, 0, 0)	0.0023	0.0169
13'	BBH:0299	(7.5, 0, 0)	0.0013	0.0172
14'	BBH:0063	(8, 0, 0)	0.0754	0.0183
15'	BBH:0300	(8.5, 0, 0)	0.0037	0.0200
16'	BBH:0301	(9, 0, 0)	0.0014	0.0203
17'	BBH:0302	(9.5, 0, 0)	0.0039	0.0219
18'	BBH:0185	(9.99, 0, 0)	0.0033	0.0246
19'	BBH:0303	(10, 0, 0)	0.0045	0.0233
20'	BAM	(4, 0, 0)	..	0.0913
21'	BAM	(10, 0, 0)	..	0.0345
22'	BAM	(18, 0, 0)	..	0.2533
23'	BBH:0001	(1, 0, 0)	..	0.1000
24'	BBH:0066	(1, 0, 0)	..	0.1252
25'	BBH:0067	(1, 0, 0)	..	0.1282
26'	BBH:0068	(1, 0, 0)	..	0.1234
27'	BBH:0070	(1, 0, 0)	..	0.0946
28'	BBH:0071	(1, 0, 0)	..	0.1252
29'	BBH:0072	(1, 0, 0)	..	0.1411
30'	BBH:0073	(1, 0, 0)	..	0.1306
31'	BBH:0086	(1, 0, 0)	..	0.1000
32'	BBH:0090	(1, 0, 0)	..	0.2034
33'	BBH:0389	(1, 0, 0)	0.0028	0.1729
34'	BBH:1132	(1, 0, 0)	0.0192	0.2272
35'	BBH:1153	(1, 0, 0)	0.0051	0.0881
36'	BBH:1154	(1, 0, 0)	0.0071	0.0882
37'	BBH:1155	(1, 0, 0)	0.0077	0.0882
38'	BBH:0198	(1.2, 0, 0)	0.0030	0.0866
39'	BBH:0310	(1.2, 0, 0)	0.0046	0.0640
40'	BBH:1143	(1.2, 0, 0)	0.0062	0.0937
41'	BBH:0008	(1.5, 0, 0)	0.0663	0.1068
42'	BBH:0093	(1.5, 0, 0)	..	0.0795
43'	BBH:0593	(1.5, 0, 0)	0.0039	0.0519
44'	BBH:0194	(1.5, 0, 0)	0.0042	0.0476
45'	BBH:1354	(1.8, 0, 0)	0.0010	0.0428

TABLE XIX. Summary of the second part of the non-spinning SXS data sets available, spanning a mass-ratio $2 \leq q \leq 10$. EOB waveforms are computed with $\chi_1 = 0$ and $\chi_2 = 10^{-4}$. This comparison demonstrates the robustness of the spinning sector of `TEOBiResumS_SM` in the nonspinning limit and the consistency with `TEOBiResumMultipoles` when spins are small. From left to right, the columns report: the SXS simulation number, mass ratio and dimensionless spins χ_i , and the maximum value of the unfaithfulness \bar{F} between: The two highest resolutions of the NR dataset, if available, see Fig. 20(left panel), and between EOB and NR, see Fig. 20(right panel).

#	id	(q, χ_1, χ_2)	$\bar{F}_{\text{NR/NR}}^{\text{max}} [\%]$	$\bar{F}_{\text{EOB/NR}}^{\text{max}} [\%]$
46'	BBH:1222	(2, 0, 0)	0.0032	0.0359
47'	BBH:0184	(2, 0, 0)	0.0039	0.0830
48'	BBH:1166	(2, 0, 0)	0.0033	0.0795
49'	BBH:0850	(2, 0, 0)	0.0047	0.0804
50'	BBH:0858	(2, 0, 0)	0.0036	0.0521
51'	BBH:1164	(2, 0, 0)	0.0010	0.0226
52'	BBH:1165	(2, 0, 0)	0.0043	0.0226
53'	BBH:1167	(2, 0, 0)	0.0027	0.0223
54'	BBH:0869	(2, 0, 0)	0.0052	0.0499
55'	BBH:0201	(2.3, 0, 0)	0.0028	0.0181
56'	BBH:0191	(2.5, 0, 0)	0.0036	0.0299
57'	BBH:1221	(3, 0, 0)	0.0016	0.0157
58'	BBH:0168	(3, 0, 0)	0.0022	0.0515
59'	BBH:0183	(3, 0, 0)	0.0029	0.0523
60'	BBH:1177	(3, 0, 0)	..	0.0521
61'	BBH:1178	(3, 0, 0)	..	0.0517
62'	BBH:1179	(3, 0, 0)	0.0020	0.0517
63'	BBH:2265	(3, 0, 0)	0.0046	0.0553
64'	BBH:0200	(3.3, 0, 0)	0.0013	0.0216
65'	BBH:0193	(3.5, 0, 0)	0.0016	0.0214
66'	BBH:0294	(3.5, 0, 0)	0.0102	0.0420
67'	BBH:1906	(4, 0, 0)	0.0014	0.0189
68'	BBH:0182	(4, 0, 0)	0.0049	0.0327
69'	BBH:2019	(4, 0, 0)	0.0016	0.0221
70'	BBH:2025	(4, 0, 0)	0.0039	0.0248
71'	BBH:2030	(4, 0, 0)	0.0034	0.0324
72'	BBH:1220	(4, 0, 0)	0.0030	0.0208
73'	BBH:0190	(4.5, 0, 0)	0.0012	0.0250
74'	BBH:0054	(5, 0, 0)	0.0024	0.0216
75'	BBH:0055	(5, 0, 0)	..	0.0208
76'	BBH:0107	(5, 0, 0)	0.0095	0.0193
77'	BBH:0112	(5, 0, 0)	..	0.0207
78'	BBH:0187	(5, 0, 0)	0.0012	0.0204
79'	BBH:0197	(5.5, 0, 0)	0.0011	0.0179
80'	BBH:0181	(6, 0, 0)	0.0007	0.0181
81'	BBH:0192	(6.6, 0, 0)	0.0020	0.0147
82'	BBH:0188	(7.2, 0, 0)	0.0022	0.0168
83'	BBH:0195	(7.8, 0, 0)	0.0040	0.0186
84'	BBH:0186	(8.3, 0, 0)	0.0014	0.0204
85'	BBH:0199	(8.7, 0, 0)	0.0089	0.0217
86'	BBH:0189	(9.2, 0, 0)	0.0015	0.0282
87'	BBH:1108	(9.2, 0, 0)	0.0032	0.0239
88'	BBH:0196	(9.7, 0, 0)	0.0045	0.0226
89'	BBH:1107	(10, 0, 0)	0.0010	0.0337

TABLE XX. Explicit coefficients and their errors for the merger frequency and amplitude fits of the (2, 2) mode. The analytic template of the fit is defined in Eqs. (C17) – (C20).

$\omega_{22}^{\text{mr}g_0}$	=	0.273356		$\hat{A}_{22}^{\text{mr}g=0}$	=	1.44959	
a_1^ω	=	0.84074	± 0.014341	$a_1^{\hat{A}}$	=	-0.041285	± 0.0078878
a_2^ω	=	1.6976	± 0.075488	$a_2^{\hat{A}}$	=	1.5971	± 0.041521
$b_1^{\omega_{m_1=m_2}}$	=	-0.42311	± 0.088583	$b_1^{\hat{A}_{m_1=m_2}}$	=	-0.74124	± 0.016178
$b_2^{\omega_{m_1=m_2}}$	=	-0.066699	± 0.042978	$b_2^{\hat{A}_{m_1=m_2}}$	=	-0.088705	± 0.0081611
$b_3^{\omega_{m_1=m_2}}$	=	-0.83053	± 0.084516	$b_3^{\hat{A}_{m_1=m_2}}$	=	-1.0939	± 0.015318
c_{11}^ω	=	0.15873	± 0.1103	$c_{11}^{\hat{A}}$	=	0.44467	± 0.037352
c_{12}^ω	=	-0.43361	± 0.2393	$c_{12}^{\hat{A}}$	=	-0.32543	± 0.081211
c_{21}^ω	=	0.60589	± 0.076215	$c_{31}^{\hat{A}}$	=	0.45828	± 0.066062
c_{22}^ω	=	-0.71383	± 0.096828	$c_{32}^{\hat{A}}$	=	-0.21245	± 0.080254

The factor $\Delta t_{21}^{\nu=1/4}$ is obtained by fitting a 2nd-order polynomial, in \hat{a}_0 to the equal-mass waveforms. Δt_{21}^0 is the test-particle value. The equal-mass spin behavior is fitted with

$$\Delta t_{21}^{\text{spin}}(\bar{S}, X_{12} = 0) = 1 + b_1^{\Delta t_{21}^{\nu=1/4}} \hat{a}_0 + b_2^{\Delta t_{21}^{\nu=1/4}} \hat{a}_0^2, \quad (\text{C31})$$

while the comparable mass case is extrapolated using

$$b_1^{\Delta t_{21}^{\nu=1/4}} \rightarrow \frac{b_1^{\Delta t_{21}^0} + c_{i1}^{\Delta t_{21}} X_{12}}{1 + c_{i2}^{\Delta t_{21}} X_{12}}, \quad (\text{C32})$$

with $i = \{1, 2\}$. The outcome of the fit, with the explicit values of all coefficients, is found in Table XXI.

c. $(\ell, m) = (3, 3)$ multipole

For this mode, the peak amplitude is written as the sum of two terms

$$\hat{A}_{33}^{\text{peak}} = \hat{A}_{33}^{\text{peak}_0} X_{12} \hat{A}_{33}^{\text{orb}}(\nu) + \hat{A}_{33}^{\text{Spin}}(\tilde{a}_{12}, \nu), \quad (\text{C33})$$

where $\hat{A}_{33}^{\text{peak}_0}$ is the peak amplitude in the test particle limit. The orbital term is modeled as

$$\hat{A}_{33}^{\text{orb}}(\nu) = \frac{1 + a_1^{\hat{A}_{33}} \nu + a_2^{\hat{A}_{33}} \nu^2}{1 + a_3^{\hat{A}_{33}} \nu}. \quad (\text{C34})$$

The spin dependence is first fitted in the test-particle limit using

$$\hat{A}_{33}^{\text{Spin}}(\tilde{a}_{12}, \nu = 0) = \frac{b_1^{\hat{A}_{33}^0} \tilde{a}_{12}}{1 + b_2^{\hat{A}_{33}^0} \tilde{a}_{12}}, \quad (\text{C35})$$

and then extended to comparable masses via the replacements

$$b_1^{\hat{A}_{33}^0} \rightarrow \frac{b_1^{\hat{A}_{33}^0} + c_{11}^{\hat{A}_{33}} \nu}{1 + c_{12}^{\hat{A}_{33}} \nu + c_{13}^{\hat{A}_{33}} \nu^2}, \quad (\text{C36})$$

$$b_2^{\hat{A}_{33}^0} \rightarrow \frac{b_2^{\hat{A}_{33}^0} + c_{21}^{\hat{A}_{33}} \nu}{1 + c_{22}^{\hat{A}_{33}} \nu + c_{23}^{\hat{A}_{33}} \nu^2}. \quad (\text{C37})$$

The instantaneous frequency ω_{33} is factorized as

$$\omega_{33}^{\text{peak}} = \omega_{33}^{\text{peak}_0} \omega_{33}^{\text{orb}}(\nu) \omega_{33}^{\text{Spin}}(\hat{S}, \nu), \quad (\text{C38})$$

where

$$\omega_{33}^{\text{orb}}(\nu) = 1 + a_1^{\omega_{33}} \nu + a_2^{\omega_{33}} \nu^2. \quad (\text{C39})$$

The test-particle spin factor is given by

$$\omega_{33}^{\text{Spin}}(\hat{S}, \nu = 0) = \frac{1 + b_1^{\omega_{33}^0} \hat{S} + b_2^{\omega_{33}^0} \hat{S}^2}{1 + b_3^{\omega_{33}^0} \hat{S}}, \quad (\text{C40})$$

while the general spin-dependence stems from the replacement

$$b_i^{\omega_{33}^0} \rightarrow \frac{b_i^{\omega_{33}^0} + c_{i1}^{\omega_{33}} \nu}{1 + c_{i2}^{\omega_{33}} \nu}, \quad (\text{C41})$$

with $i = \{1, 3\}$.

To describe Δt_{33} we start from the expression

$$\Delta t_{33} = \Delta t_{33}^0 \Delta t_{33}^{\text{orb}}(\nu) \Delta t_{33}^{\text{Spin}}(\hat{S}, \nu), \quad (\text{C42})$$

with

$$\Delta t_{33}^{\text{orb}}(\nu) = 1 + a_1^{\Delta t_{33}} \nu + a_2^{\Delta t_{33}} \nu^2, \quad (\text{C43})$$

$$\Delta t_{33}^{\text{Spin}}(\hat{S}, \nu = 0) = \frac{1 + b_1^{\Delta t_{33}^0} \hat{S} + b_2^{\Delta t_{33}^0} \hat{S}^2}{1 + b_3^{\Delta t_{33}^0} \hat{S}}. \quad (\text{C44})$$

The spin-dependence is obtained from the replacement

$$b_1^{\Delta t_{33}^0} \rightarrow \frac{b_1^{\Delta t_{33}^0} + c_{i1}^{\Delta t_{33}} \nu}{1 + c_{i2}^{\Delta t_{33}} \nu}, \quad (\text{C45})$$

with $i = \{1, 2, 3\}$. The explicit values of the fit coefficients are listed in Table XXII.

TABLE XXI. Explicit coefficients of the fits of $\hat{A}_{21}^{\text{peak}}$, $\omega_{21}^{\text{peak}}$ and Δt_{21} .

$\hat{A}_{21}^{\text{peak}_0}$	=	0.523878	$\omega_{21}^{\text{peak}_0}$	=	0.290643	Δt_{21}^0	=	11.75925
$a_1^{\hat{A}_{21}}$	=	3.33622	$a_1^{\omega_{21}}$	=	-0.563075	$\Delta t_{21}^{\nu=1/4}$	=	6.6264
$a_2^{\hat{A}_{21}}$	=	3.47085	$a_2^{\omega_{21}}$	=	3.28677	$a_1^{\Delta t_{21}}$	=	-2.0728
$a_3^{\hat{A}_{21}}$	=	4.76236						
$b_1^{\hat{A}_{21}^0}$	=	-0.428186	$b_1^{\omega_{21}^0}$	=	0.179639	$b_1^{\Delta t_{21}^0}$	=	0.0472289
$b_2^{\hat{A}_{21}^0}$	=	-0.335659	$b_2^{\omega_{21}^0}$	=	-0.302122	$b_2^{\Delta t_{21}^0}$	=	0.115583
$b_3^{\hat{A}_{21}^0}$	=	0.828923						
$c_{11}^{\hat{A}_{21}}$	=	0.891139	$c_1^{\omega_{21}}$	=	-1.20684	$c_{11}^{\Delta t_{21}}$	=	-1976.13
$c_{12}^{\hat{A}_{21}}$	=	-5.191702	$c_2^{\omega_{21}}$	=	0.425645	$c_{12}^{\Delta t_{21}}$	=	3719.88
$c_{21}^{\hat{A}_{21}}$	=	3.480139				$c_{21}^{\Delta t_{21}}$	=	-2545.41
$c_{22}^{\hat{A}_{21}}$	=	10.237782				$c_{22}^{\Delta t_{21}}$	=	5277.62
$c_{31}^{\hat{A}_{21}}$	=	-13.867475						
$c_{32}^{\hat{A}_{21}}$	=	10.525510						

TABLE XXII. Explicit coefficients of the fits of $\hat{A}_{33}^{\text{peak}}$, $\omega_{33}^{\text{peak}}$ and Δt_{33} .

$\hat{A}_{33}^{\text{peak}_0}$	=	0.566017	$\omega_{33}^{\text{peak}_0}$	=	0.454128	Δt_{33}^0	=	3.42593
$a_1^{\hat{A}_{33}}$	=	-0.22523	$a_1^{\omega_{33}}$	=	1.08224	$a_1^{\Delta t_{33}}$	=	0.183349
$a_2^{\hat{A}_{33}}$	=	3.0569	$a_2^{\omega_{33}}$	=	2.59333	$a_2^{\Delta t_{33}}$	=	4.22361
$a_3^{\hat{A}_{33}}$	=	-0.396851						
$b_1^{\hat{A}_{33}^0}$	=	0.100069	$b_1^{\omega_{33}^0}$	=	-0.406161	$b_1^{\Delta t_{33}^0}$	=	-0.49791
$b_2^{\hat{A}_{33}^0}$	=	-0.455859	$b_2^{\omega_{33}^0}$	=	-0.0647944	$b_2^{\Delta t_{33}^0}$	=	-0.18754
			$b_3^{\omega_{33}^0}$	=	-0.748126	$b_3^{\Delta t_{33}^0}$	=	-1.07291
$c_{11}^{\hat{A}_{33}}$	=	-0.401156	$c_{11}^{\omega_{33}}$	=	0.85777	$c_{11}^{\Delta t_{33}}$	=	-1.9478
$c_{12}^{\hat{A}_{33}}$	=	-0.141551	$c_{12}^{\omega_{33}}$	=	-0.70066	$c_{12}^{\Delta t_{33}}$	=	13.9828
$c_{13}^{\hat{A}_{33}}$	=	-15.4949	$c_{31}^{\omega_{33}}$	=	2.97025	$c_{21}^{\Delta t_{33}}$	=	1.25084
$c_{21}^{\hat{A}_{33}}$	=	1.84962	$c_{32}^{\omega_{33}}$	=	-3.96242	$c_{22}^{\Delta t_{33}}$	=	-3.41811
$c_{22}^{\hat{A}_{33}}$	=	-2.03512				$c_{31}^{\Delta t_{33}}$	=	-1043.15
$c_{23}^{\hat{A}_{33}}$	=	-4.92334				$c_{32}^{\Delta t_{33}}$	=	1033.85

d. $(\ell, m) = (3, 2)$ multipole

The peak amplitude of the $(3, 2)$ mode is fitted with a factorized template of the form

$$\hat{A}_{32}^{\text{peak}} = \hat{A}_{32}^{\text{peak}_0} (1 - 3\nu) \hat{A}_{32}^{\text{orb}}(\nu) \hat{A}_{32}^{\text{Spin}}(\bar{S}, \nu), \quad (\text{C46})$$

where $\hat{A}_{32}^{\text{peak}_0}$ is the peak amplitude of the mode in the test-particle limit. The factor $\hat{A}_{32}^{\text{orb}}$ is informed by non-spinning waveforms and is fitted with the template

$$\hat{A}_{32}^{\text{orb}}(\nu) = \frac{1 + a_1^{\hat{A}_{32}} \nu + a_2^{\hat{A}_{32}} \nu^2}{1 + a_3^{\hat{A}_{32}} \nu}. \quad (\text{C47})$$

The spin dependence is first captured for the test-particle limit with the function

$$\hat{A}_{32}^{\text{Spin}}(\bar{S}, \nu = 0) = \frac{1 + b_1^{\hat{A}_{32}^0} \tilde{a}_0}{1 + b_2^{\hat{A}_{32}^0} \tilde{a}_0}, \quad (\text{C48})$$

while the ν -dependence enters via the replacement

$$b_i^{\hat{A}_{32}^0} \rightarrow \frac{b_i^{\hat{A}_{32}^0} + c_{i1}^{\hat{A}_{32}} \nu + c_{i2}^{\hat{A}_{32}} \nu^2}{1 + c_{i3}^{\hat{A}_{32}} \nu + c_{i4}^{\hat{A}_{32}} \nu^2}, \quad (\text{C49})$$

with $i = \{1, 2\}$.

The instantaneous frequency ω_{32} mode is factorized as

$$\omega_{32}^{\text{peak}} = \omega_{32}^{\text{peak}_0} \omega_{32}^{\text{orb}}(\nu) \omega_{32}^{\text{Spin}}(\tilde{a}_0, \nu). \quad (\text{C50})$$

The orbital dependence is modeled as

$$\omega_{32}^{\text{orb}}(\nu) = \frac{1 + a_1^{\omega_{32}} \nu + a_2^{\omega_{32}} \nu^2}{1 + a_3^{\omega_{32}} \nu + a_4^{\omega_{32}} \nu^2}. \quad (\text{C51})$$

The spin dependence is fitted first for the equal-mass case

$$\omega_{32}^{\text{Spin}}(\tilde{a}_0, \nu = 1/4) = \frac{1 + b_1^{\omega_{32}^{\nu=1/4}} \tilde{a}_0 + b_2^{\omega_{32}^{\nu=1/4}} \tilde{a}_0^2}{1 + b_3^{\omega_{32}^{\nu=1/4}} \tilde{a}_0}, \quad (\text{C52})$$

while the additional dependence on the mass ratio enters via the replacements

$$b_i^{\omega_{32}^0} \rightarrow \frac{b_i^{\omega_{32}^{\nu=1/4}} + c_i^{\omega_{32}} X_{12} + c_{i2}^{\omega_{32}} X_{12}^2}{1 + c_{i3}^{\omega_{32}} X_{12}}, \quad (\text{C53})$$

with $i = \{1, 2\}$. The coefficients of $\hat{A}_{32}^{\text{peak}}$ and $\omega_{32}^{\text{peak}}$ are explicitly listed in Table XXVII.

Moving to Δt_{32} , it is given by

$$\Delta t_{32} = \Delta t_{32}^0 \Delta t_{32}^{\text{orb}}(\nu) \Delta t_{32}^{\text{spin}}(\hat{S}, \nu), \quad (\text{C54})$$

where the orbital behavior is fitted with

$$\Delta t_{32}^{\text{orb}}(\nu) = \frac{1 + a_1^{\Delta t_{32}} \nu + a_2^{\Delta t_{32}} \nu^2}{1 + a_3^{\Delta t_{32}} \nu + a_4^{\Delta t_{32}} \nu^2}. \quad (\text{C55})$$

The spin behavior is more complicated than the corresponding term of other modes. This is separated into two sectors, as

$$\begin{aligned} \Delta t_{32}^{\text{spin}}(\hat{S}, \nu) &= \Delta t_{32}^{\text{spin}_{\nu > 1/5}}(\hat{S}, \nu) \Theta(\nu - 1/5) \\ &\quad + \Delta t_{32}^{\text{spin}_{\nu \leq 1/5}}(\hat{S}, \nu) [1 - \Theta(\nu - 1/5)], \end{aligned} \quad (\text{C56})$$

where Θ denotes the Heaviside step function. In the $\nu > 1/5$ regime the fit is first done to the equal-mass case

$$\Delta t_{32}^{\text{spin}_{\nu > 1/5}}(\hat{S}, \nu = 1/4) = \frac{1 + b_1^{\Delta t_{32}^{\nu=1/4}} \hat{S} + b_2^{\Delta t_{32}^{\nu=1/4}} \hat{S}^2}{1 + b_3^{\Delta t_{32}^{\nu=1/4}} \hat{S}}. \quad (\text{C57})$$

Then it is extrapolated following

$$b_i^{\Delta t_{32}^{\nu=1/4}} \rightarrow \frac{b_i^{\Delta t_{32}^{\nu=1/4}} + c_{i1}^{\Delta t_{32}} X_{12} + c_{i2}^{\Delta t_{32}} X_{12}^2 + c_{i3}^{\Delta t_{32}} X_{12}^3}{1 + c_{i4}^{\Delta t_{32}} X_{12} + c_{i5}^{\Delta t_{32}} X_{12}^2}, \quad (\text{C58})$$

with $i = \{1, 2, 3\}$.

In the $\nu \leq 1/5$ regime the fit is first done to the equal-mass case

$$\Delta t_{32}^{\text{spin}_{\nu \leq 1/5}}(\hat{S}, \nu = 0) = \frac{1 + b_1^{\Delta t_{32}^0} \hat{S} + b_2^{\Delta t_{32}^0} \hat{S}^2}{1 + b_3^{\Delta t_{32}^0} \hat{S}}. \quad (\text{C59})$$

Then it is extrapolated following

$$b_i^{\Delta t_{32}^0} \rightarrow \frac{b_i^{\Delta t_{32}^0} + c_{i1}^{\Delta t_{32}} \nu + c_{i2}^{\Delta t_{32}} \nu^2 + c_{i3}^{\Delta t_{32}} \nu^3}{1 + c_{i4}^{\Delta t_{32}} \nu + c_{i5}^{\Delta t_{32}} \nu^2}, \quad (\text{C60})$$

with $i = \{1, 2, 3\}$. The coefficients appearing in Δt_{32} are shown in Table XXIV.

e. $(\ell, m) = (4, 4)$ multipole

The peak amplitude of the $(4, 4)$ mode is fitted with

$$\hat{A}_{44}^{\text{peak}} = \hat{A}_{44}^{\text{peak}_0} (1 - 3\nu) \hat{A}_{44}^{\text{orb}}(\nu) \hat{A}_{44}^{\text{Spin}}(\hat{S}, \nu), \quad (\text{C61})$$

TABLE XXIII. Explicit coefficients of the fits of $\hat{A}_{32}^{\text{peak}}$ and $\omega_{32}^{\text{peak}}$.

$\hat{A}_{32}^{\text{peak}_0}$	= 0.199019	$\omega_{32}^{\text{peak}_0}$	= 0.451607
$a_1^{\hat{A}_{32}}$	= -6.06831	$a_1^{\omega_{32}}$	= -9.13525
$a_2^{\hat{A}_{32}}$	= 10.7505	$a_2^{\omega_{32}}$	= 21.488
$a_3^{\hat{A}_{32}}$	= -3.68883	$a_3^{\omega_{32}}$	= -8.81384
		$a_4^{\omega_{32}}$	= 20.0595
$b_1^{\hat{A}_{32}^0}$	= -0.258378	$b_1^{\omega_{32}^{\nu=1/4}}$	= -0.458126
$b_2^{\hat{A}_{32}^0}$	= 0.679163	$b_2^{\omega_{32}^{\nu=1/4}}$	= 0.0474616
		$b_3^{\omega_{32}^{\nu=1/4}}$	= -0.486049
$c_{11}^{\hat{A}_{32}}$	= 4.36263	$c_{11}^{\omega_{32}}$	= 3.25319
$c_{12}^{\hat{A}_{32}}$	= -12.5897	$c_{12}^{\omega_{32}}$	= 0.535555
$c_{13}^{\hat{A}_{32}}$	= -7.73233	$c_{13}^{\omega_{32}}$	= -8.07905
$c_{14}^{\hat{A}_{32}}$	= 16.2082	$c_{21}^{\omega_{32}}$	= 1.00066
$c_{21}^{\hat{A}_{32}}$	= 3.04724	$c_{22}^{\omega_{32}}$	= -1.1333
$c_{22}^{\hat{A}_{32}}$	= 46.5711	$c_{23}^{\omega_{32}}$	= 0.601572
$c_{23}^{\hat{A}_{32}}$	= 2.10475		
$c_{24}^{\hat{A}_{32}}$	= 56.9136		

where $\hat{A}_{44}^{\text{peak}_0}$ is the peak amplitude of the mode in the test-particle limit. The factor $\hat{A}_{44}^{\text{orb}}$ is informed by non-spinning waveforms and is fitted with the template

$$\hat{A}_{44}^{\text{orb}}(\nu) = \frac{1 + a_1^{\hat{A}_{44}} \nu + a_2^{\hat{A}_{44}} \nu^2}{1 + a_3^{\hat{A}_{44}} \nu}. \quad (\text{C62})$$

The spin dependence is first captured for the test-particle limit with the function

$$\hat{A}_{44}^{\text{Spin}}(\hat{S}, \nu = 0) = \frac{1 + b_1^{\hat{A}_{44}^0} \hat{S} + b_2^{\hat{A}_{44}^0} \hat{S}^2}{1 + b_3^{\hat{A}_{44}^0} \hat{S}}, \quad (\text{C63})$$

and then extended in the comparable mass region of the parameter space through

$$b_i^{\hat{A}_{44}^0} \rightarrow \frac{b_i^{\hat{A}_{44}^0} + c_{i1}^{\hat{A}_{44}} \nu + c_{i2}^{\hat{A}_{44}} \nu^2}{1 + c_{i3}^{\hat{A}_{44}} \nu + c_{i4}^{\hat{A}_{44}} \nu^2}, \quad \text{with } i = \{1, 2, 3\}. \quad (\text{C64})$$

The peak frequency ω_{44} is factorized as

$$\omega_{44}^{\text{peak}} = \omega_{44}^{\text{peak}_0} \omega_{44}^{\text{orb}}(\nu) \omega_{44}^{\text{Spin}}(\hat{S}, \nu). \quad (\text{C65})$$

The orbital dependence is modeled through

$$\omega_{44}^{\text{orb}}(\nu) = \frac{1 + a_1^{\omega_{44}} \nu + a_2^{\omega_{44}} \nu^2}{1 + a_3^{\omega_{44}} \nu + a_4^{\omega_{44}} \nu^2}. \quad (\text{C66})$$

The spin dependence is fitted first for the test-particle limit as

$$\omega_{44}^{\text{Spin}}(\hat{S}, \nu = 0) = \frac{1 + b_1^{\omega_{44}^0} \hat{S} + b_2^{\omega_{44}^0} \hat{S}^2 + b_3^{\omega_{44}^0} \hat{S}^3}{1 + b_4^{\omega_{44}^0} \hat{S}}. \quad (\text{C67})$$

TABLE XXIV. Explicit coefficients of Δt_{32} .

Δt_{32}^0	=	9.16665	$\Delta t_{11}^{\nu'_{32}}$	=	-0.037634	$\Delta t_{11}^{\nu'_{32} X_{12}}$	=	2.497188
$a_1^{\Delta t_{32}}$	=	-11.3497	$\Delta t_{12}^{\nu'_{32}}$	=	12.456704	$\Delta t_{12}^{\nu'_{32} X_{12}}$	=	-7.532596
$a_2^{\Delta t_{32}}$	=	32.9144	$\Delta t_{13}^{\nu'_{32}}$	=	2.670868	$\Delta t_{13}^{\nu'_{32} X_{12}}$	=	4.645986
$a_3^{\Delta t_{32}}$	=	-8.36579	$\Delta t_{14}^{\nu'_{32}}$	=	-12.255859	$\Delta t_{14}^{\nu'_{32} X_{12}}$	=	-3.652524
$a_4^{\Delta t_{32}}$	=	20.1017	$\Delta t_{15}^{\nu'_{32}}$	=	37.843505	$\Delta t_{15}^{\nu'_{32} X_{12}}$	=	3.398687
$b_1^{\Delta t_{32}^0}$	=	-0.34161	$\Delta t_{21}^{\nu'_{32}}$	=	-25.058475	$\Delta t_{21}^{\nu'_{32} X_{12}}$	=	7.054185
$b_2^{\Delta t_{32}^0}$	=	-0.46107	$\Delta t_{22}^{\nu'_{32}}$	=	449.470722	$\Delta t_{22}^{\nu'_{32} X_{12}}$	=	-12.260185
$b_3^{\Delta t_{32}^0}$	=	0.34744	$\Delta t_{23}^{\nu'_{32}}$	=	-1413.508735	$\Delta t_{23}^{\nu'_{32} X_{12}}$	=	5.724802
$b_1^{\Delta t_{32}^{\nu=1/4}}$	=	0.15477	$\Delta t_{24}^{\nu'_{32}}$	=	-11.852596	$\Delta t_{24}^{\nu'_{32} X_{12}}$	=	-3.242611
$b_2^{\Delta t_{32}^{\nu=1/4}}$	=	-0.755639	$\Delta t_{25}^{\nu'_{32}}$	=	41.348059	$\Delta t_{25}^{\nu'_{32} X_{12}}$	=	2.714232
$b_3^{\Delta t_{32}^{\nu=1/4}}$	=	0.21816	$\Delta t_{31}^{\nu'_{32}}$	=	-5.650710	$\Delta t_{31}^{\nu'_{32} X_{12}}$	=	2.614565
			$\Delta t_{32}^{\nu'_{32}}$	=	-9.567484	$\Delta t_{32}^{\nu'_{32} X_{12}}$	=	-9.507583
			$\Delta t_{33}^{\nu'_{32}}$	=	173.182999	$\Delta t_{33}^{\nu'_{32} X_{12}}$	=	7.321586
			$\Delta t_{34}^{\nu'_{32}}$	=	-10.938605	$\Delta t_{34}^{\nu'_{32} X_{12}}$	=	-3.937568
			$\Delta t_{35}^{\nu'_{32}}$	=	35.670656	$\Delta t_{35}^{\nu'_{32} X_{12}}$	=	4.584970

The spin dependence in the comparable mass region of the parameter space is modeled through

$$b_i^{\omega_{44}^0} \rightarrow \frac{b_i^{\omega_{44}^0} + c_{i1}^{\omega_{44}^0} \nu + c_{i2}^{\omega_{44}^0} \nu^2}{1 + c_{i3}^{\omega_{44}^0} \nu + c_{i4}^{\omega_{44}^0} \nu^2}, \quad (\text{C68})$$

with $i = \{1, 2, 3, 4\}$.

We fit Δt_{44} in a factorized form as

$$\Delta t_{44} = \Delta t_{44}^0 \Delta t_{44}^{\text{orb}}(\nu) \Delta t_{44}^{\text{spin}}(\hat{S}, X_{12}). \quad (\text{C69})$$

The orbital behavior is fitted with

$$\Delta t_{44}^{\text{orb}}(\nu) = \frac{1 + a_1^{\Delta t_{44}} \nu + a_2^{\Delta t_{44}} \nu^2}{1 + a_3^{\Delta t_{44}} \nu + a_4^{\Delta t_{44}} \nu^2}, \quad (\text{C70})$$

while the spinning one is first fitted to equal mass simulations as

$$\Delta t_{44}^{\text{spin}}(\hat{S}, X_{12} = 0) = \frac{1 + b_1^{\Delta t_{44}^{\nu=1/4}} \hat{S}}{1 + b_2^{\Delta t_{44}^{\nu=1/4}} \hat{S}}. \quad (\text{C71})$$

The general ν -dependence enters via the replacement

$$b_i^{\Delta t_{44}^{\nu=1/4}} \rightarrow b_i^{\Delta t_{44}^{\nu=1/4}} + c_{i1}^{\Delta t_{44}} X_{12} + c_{i2}^{\Delta t_{44}} X_{12}^2, \quad (\text{C72})$$

with $i = \{1, 2\}$. The explicit values of the fit coefficients can be found in Table XXV.

f. $(\ell, m) = (4, 3)$ multipole

The peak amplitude of the $(4, 3)$ mode is fitted with

$$\hat{A}_{43}^{\text{peak}} = \hat{A}_{43}^{\text{peak}_0} X_{12} (1 - 2\nu) \hat{A}_{43}^{\text{orb}}(\nu) + \hat{A}_{43}^{\text{Spin}}(\tilde{a}_0, \nu), \quad (\text{C73})$$

where $\hat{A}_{43}^{\text{peak}_0}$ is the peak amplitude of the mode in the test-particle limit. The factor $\hat{A}_{43}^{\text{orb}}$ is informed by non-spinning waveforms and is fitted with the template

$$\hat{A}_{43}^{\text{orb}}(\nu) = \frac{1 + a_1^{\hat{A}_{43}} \nu + a_2^{\hat{A}_{43}} \nu^2}{1 + a_3^{\hat{A}_{43}} \nu}. \quad (\text{C74})$$

The spin dependence is first captured for the test-particle limit with the function

$$\hat{A}_{43}^{\text{Spin}}(\tilde{a}_0, \nu = 0) = \frac{1 + b_1^{\hat{A}_{43}^0} \tilde{a}_0 + b_2^{\hat{A}_{43}^0} \tilde{a}_0^2}{1 + b_3^{\hat{A}_{43}^0} \tilde{a}_0}. \quad (\text{C75})$$

The spin dependence in the comparable mass region of the parameter space is modeled through

$$b_i^{\hat{A}_{43}^0} \rightarrow \frac{b_i^{\hat{A}_{43}^0} + c_{i1}^{\hat{A}_{43}^0} \nu}{1 + c_{i2}^{\hat{A}_{43}^0} \nu + c_{i3}^{\hat{A}_{43}^0} \nu^2}, \quad (\text{C76})$$

with $i = \{1, 2, 3\}$. For the equal mass case however a special fit is made to accurately capture the correct behavior, i.e.

$$\hat{A}_{43}^{\text{peak}}\left(\tilde{a}_{12}, \nu = \frac{1}{4}\right) = \frac{b_1^{\hat{A}_{43}^{\nu=1/4}} \tilde{a}_{12} + b_2^{\hat{A}_{43}^{\nu=1/4}} \tilde{a}_{12}^2}{1 + b_3^{\hat{A}_{43}^{\nu=1/4}} \tilde{a}_{12}}. \quad (\text{C77})$$

The instantaneous frequency at peak $\omega_{43}^{\text{peak}}$ is factorized as

$$\omega_{43}^{\text{peak}} = \omega_{43}^{\text{peak}_0} \omega_{43}^{\text{orb}}(\nu) \omega_{43}^{\text{Spin}}(\hat{S}, \nu), \quad (\text{C78})$$

where the orbital factor is modeled as

$$\omega_{43}^{\text{orb}}(\nu) = \frac{1 + a_1^{\omega_{43}} \nu + a_2^{\omega_{43}} \nu^2}{1 + a_3^{\omega_{43}} \nu + a_4^{\omega_{43}} \nu^2}. \quad (\text{C79})$$

TABLE XXV. Explicit coefficients of the fits of $\hat{A}_{44}^{\text{peak}}$, $\omega_{44}^{\text{peak}}$ and Δt_{44} .

$\hat{A}_{44}^{\text{peak}_0}$	=	0.276618	$\omega_{44}^{\text{peak}_0}$	=	0.635659	Δt_{44}^0	=	5.27778
$a_1^{\hat{A}_{44}}$	=	-3.7082	$a_1^{\omega_{44}}$	=	-0.964614	$a_1^{\Delta t_{44}}$	=	-8.35574
$a_2^{\hat{A}_{44}}$	=	0.280906	$a_2^{\omega_{44}}$	=	-11.1828	$a_2^{\Delta t_{44}}$	=	17.5288
$a_3^{\hat{A}_{44}}$	=	-3.71276	$a_3^{\omega_{44}}$	=	-2.08471	$a_3^{\Delta t_{44}}$	=	-6.50259
			$a_4^{\omega_{44}}$	=	-6.89287	$a_4^{\Delta t_{44}}$	=	10.1575
$b_1^{\hat{A}_{44}^0}$	=	-0.316647	$b_1^{\omega_{44}^0}$	=	-0.445192	$b_1^{\Delta t_{44}^{\nu=1/4}}$	=	0.00159701
$b_2^{\hat{A}_{44}^0}$	=	-0.062423	$b_2^{\omega_{44}^0}$	=	-0.0985658	$b_2^{\Delta t_{44}^{\nu=1/4}}$	=	-1.14134
$b_3^{\hat{A}_{44}^0}$	=	-0.852876	$b_3^{\omega_{44}^0}$	=	-0.0307812			
			$b_4^{\omega_{44}^0}$	=	-0.801552			
$c_{11}^{\hat{A}_{44}}$	=	1.2436	$c_{11}^{\omega_{44}}$	=	-0.92902	$c_{11}^{\Delta t_{44}}$	=	-2.28656
$c_{12}^{\hat{A}_{44}}$	=	-1.60555	$c_{12}^{\omega_{44}}$	=	10.86310	$c_{12}^{\Delta t_{44}}$	=	1.66532
$c_{13}^{\hat{A}_{44}}$	=	-4.05685	$c_{13}^{\omega_{44}}$	=	-4.44930	$c_{21}^{\Delta t_{44}}$	=	-0.589331
$c_{14}^{\hat{A}_{44}}$	=	1.59143	$c_{14}^{\omega_{44}}$	=	3.01808	$c_{22}^{\Delta t_{44}}$	=	0.708784
$c_{21}^{\hat{A}_{44}}$	=	0.837418	$c_{22}^{\omega_{44}}$	=	1.62523			
$c_{22}^{\hat{A}_{44}}$	=	-2.93528	$c_{23}^{\omega_{44}}$	=	-7.70486			
$c_{23}^{\hat{A}_{44}}$	=	-11.5591	$c_{23}^{\omega_{44}}$	=	15.06517			
$c_{24}^{\hat{A}_{44}}$	=	34.1863	$c_{41}^{\omega_{44}}$	=	0.93790			
$c_{31}^{\hat{A}_{44}}$	=	0.950035	$c_{42}^{\omega_{44}}$	=	8.36038			
$c_{32}^{\hat{A}_{44}}$	=	7.95168	$c_{43}^{\omega_{44}}$	=	-4.85774			
$c_{33}^{\hat{A}_{44}}$	=	-1.26899	$c_{44}^{\omega_{44}}$	=	4.80446			
$c_{34}^{\hat{A}_{44}}$	=	-9.72147						

The spin dependence is fitted first for the test-particle case

$$\omega_{43}^{\text{Spin}}(\hat{S}, \nu = 0) = \frac{1 + b_1^{\omega_{43}^0} \hat{S} + b_2^{\omega_{43}^0} \hat{S}^2}{1 + b_3^{\omega_{43}^0} \hat{S}}, \quad (\text{C80})$$

and then extended to other regions of the parameter space with

$$b_i^{\omega_{43}^0} \rightarrow \frac{b_i^{\omega_{43}^0} + c_{i1}^{\omega_{43}} \nu + c_{i2}^{\omega_{43}} \nu^2}{1 + c_{i3}^{\omega_{43}} \nu}, \quad (\text{C81})$$

where $i = \{1, 2, 3\}$.

For what concerns Δt_{43} , it is represented as

$$\Delta t_{43} = \Delta t_{43}^0 \Delta t_{43}^{\text{orb}}(\nu) \Delta t_{43}^{\text{spin}}(\hat{S}, \nu), \quad (\text{C82})$$

with

$$\Delta t_{43}^{\text{orb}}(\nu) = \frac{1 + a_1^{\Delta t_{43}} \nu + a_2^{\Delta t_{43}} \nu^2}{1 + a_3^{\Delta t_{43}} \nu + a_4^{\Delta t_{43}} \nu^2}, \quad (\text{C83})$$

$$\Delta t_{43}^{\text{spin}}(\hat{S}, \nu = 0) = \frac{1 + b_1^{\Delta t_{43}^0} \hat{S} + b_2^{\Delta t_{43}^0} \hat{S}^2}{1 + b_3^{\Delta t_{43}^0} \hat{S}}. \quad (\text{C84})$$

We then incorporate the general ν -dependence via the replacement

$$b_i^{\Delta t_{43}^0} \rightarrow \frac{b_i^{\Delta t_{43}^0} + c_{i1}^{\Delta t_{43}} \nu + c_{i2}^{\Delta t_{43}} \nu^2}{1 + c_{i3}^{\Delta t_{43}} \nu + c_{i4}^{\Delta t_{43}} \nu^2}, \quad (\text{C85})$$

with $i = \{1, 2, 3\}$. The explicit values of the fit coefficients are listed in Table XXVI.

$$g. \quad (\ell, m) = (4, 2) \text{ multipole}$$

The peak amplitude of the (4, 2) mode is fitted with a factorized template of the form

$$\hat{A}_{42}^{\text{peak}} = \hat{A}_{42}^{\text{peak}_0} (1 - 3\nu) \hat{A}_{42}^{\text{orb}}(\nu) \hat{A}_{42}^{\text{Spin}}(\hat{S}, \nu), \quad (\text{C86})$$

where $\hat{A}_{42}^{\text{peak}_0}$ is the peak amplitude of the mode in the test-particle limit. The factor $\hat{A}_{42}^{\text{orb}}$ is informed by non-spinning waveforms and is fitted with the template

$$\hat{A}_{42}^{\text{orb}}(\nu) = 1 + a_1^{\hat{A}_{42}} \nu + a_2^{\hat{A}_{42}} \nu^2. \quad (\text{C87})$$

The spin dependence is first captured for the test-particle limit with the function

$$\hat{A}_{42}^{\text{Spin}}(\hat{S}, \nu = 0) = \frac{1 + b_1^{\hat{A}_{42}^0} \hat{S} + b_2^{\hat{A}_{42}^0} \hat{S}^2}{1 + b_3^{\hat{A}_{42}^0} \hat{S} + b_4^{\hat{A}_{42}^0} \hat{S}^2}. \quad (\text{C88})$$

The general ν -dependence is then taken into account via the replacement

$$b_i^{\hat{A}_{42}^0} \rightarrow \frac{b_i^{\hat{A}_{42}^0} + c_{i1}^{\hat{A}_{42}} \nu}{1 + c_{i2}^{\hat{A}_{42}} \nu}, \quad (\text{C89})$$

TABLE XXVI. Explicit coefficients of the fits of $\hat{A}_{43}^{\text{peak}}$, $\omega_{43}^{\text{peak}}$ and Δt_{43} .

$\hat{A}_{43}^{\text{peak}_0}$	=	0.0941570	$\omega_{43}^{\text{peak}_0}$	=	0.636130	Δt_{43}^0	=	9.53705
$a_1^{\hat{A}_{43}}$	=	-5.74386	$a_1^{\omega_{43}}$	=	-9.02463	$a_1^{\Delta t_{43}}$	=	-11.2377
$a_2^{\hat{A}_{43}}$	=	12.6016	$a_2^{\omega_{43}}$	=	21.9802	$a_2^{\Delta t_{43}}$	=	38.3177
$a_3^{\hat{A}_{43}}$	=	-3.27435	$a_3^{\omega_{43}}$	=	-8.75892	$a_3^{\Delta t_{43}}$	=	-7.29734
$a_4^{\omega_{43}}$	=	20.5624				$a_4^{\Delta t_{43}}$	=	21.4267
$b_1^{\hat{A}_{43}^0}$	=	-0.02132252	$b_1^{\omega_{43}^0}$	=	-0.973324	$b_1^{\Delta t_{43}^0}$	=	-1.371832
$b_2^{\hat{A}_{43}^0}$	=	0.02592749	$b_2^{\omega_{43}^0}$	=	-0.109921	$b_2^{\Delta t_{43}^0}$	=	0.362375
$b_3^{\hat{A}_{43}^0}$	=	-0.826977	$b_3^{\omega_{43}^0}$	=	-1.08036	$b_3^{\Delta t_{43}^0}$	=	-1.0808402
$b_1^{\hat{A}_{43}^{\nu=1/4}}$	=	-0.00471163						
$b_2^{\hat{A}_{43}^{\nu=1/4}}$	=	0.0291409						
$b_3^{\hat{A}_{43}^{\nu=1/4}}$	=	-0.351031						
$c_{11}^{\hat{A}_{43}}$	=	0.249099	$c_{11}^{\omega_{43}}$	=	11.5224	$c_{11}^{\Delta t_{43}}$	=	3.215984
$c_{12}^{\hat{A}_{43}}$	=	-7.345984	$c_{12}^{\omega_{43}}$	=	-26.8421	$c_{12}^{\Delta t_{43}}$	=	42.133767
$c_{13}^{\hat{A}_{43}}$	=	108.923746	$c_{13}^{\omega_{43}}$	=	-2.84285	$c_{13}^{\Delta t_{43}}$	=	-9.440398
$c_{21}^{\hat{A}_{43}}$	=	-0.104206	$c_{21}^{\omega_{43}}$	=	3.51943	$c_{14}^{\Delta t_{43}}$	=	35.160776
$c_{22}^{\hat{A}_{43}}$	=	7.073534	$c_{22}^{\omega_{43}}$	=	-12.1688	$c_{21}^{\Delta t_{43}}$	=	1.133942
$c_{23}^{\hat{A}_{43}}$	=	-44.374738	$c_{23}^{\omega_{43}}$	=	-3.96385	$c_{22}^{\Delta t_{43}}$	=	-10.356311
$c_{31}^{\hat{A}_{43}}$	=	3.545134	$c_{31}^{\omega_{43}}$	=	5.53433	$c_{23}^{\Delta t_{43}}$	=	-6.701429
$c_{32}^{\hat{A}_{43}}$	=	1.341375	$c_{32}^{\omega_{43}}$	=	3.73988	$c_{24}^{\Delta t_{43}}$	=	10.726960
$c_{33}^{\hat{A}_{43}}$	=	-19.552083	$c_{33}^{\omega_{43}}$	=	4.219	$c_{31}^{\Delta t_{43}}$	=	-6.036207
						$c_{32}^{\Delta t_{43}}$	=	67.730599
						$c_{33}^{\Delta t_{43}}$	=	-3.082275
						$c_{34}^{\Delta t_{43}}$	=	11.547917

with $i = \{1, 2, 3, 4\}$.

The instantaneous frequency $\omega_{42}^{\text{peak}}$ is factorized as

$$\omega_{42}^{\text{peak}} = \omega_{42}^{\text{peak}_0} \omega_{42}^{\text{orb}}(\nu) \omega_{42}^{\text{Spin}}(\hat{S}, \nu) \quad (\text{C90})$$

The orbital dependence is modeled through

$$\omega_{42}^{\text{orb}}(\nu) = \frac{1 + a_1^{\omega_{42}} \nu + a_2^{\omega_{42}} \nu^2}{1 + a_3^{\omega_{42}} \nu + a_4^{\omega_{42}} \nu^2}. \quad (\text{C91})$$

The spin dependence is fitted first for the test-mass case with

$$\omega_{42}^{\text{Spin}}(\hat{S}, \nu = 0) = \frac{1 + b_1^{\omega_{42}^0} \hat{S} + b_2^{\omega_{42}^0} \hat{S}^2}{1 + b_3^{\omega_{42}^0} \hat{S} + b_4^{\omega_{42}^0} \hat{S}^2}, \quad (\text{C92})$$

and then the general ν -dependence is taken into account via the replacement

$$b_i^{\omega_{42}^0} \rightarrow \frac{b_i^{\omega_{42}^0} + c_{i1}^{\omega_{42}} \nu}{1 + c_{i2}^{\omega_{42}} \nu + c_{i3}^{\omega_{42}} \nu^2}, \quad (\text{C93})$$

with $i = \{1, 2, 3, 4\}$. The delay Δt_{42} is fitted as

$$\Delta t_{42} = \Delta t_{42}^0 \Delta t_{42}^{\text{orb}}(\nu) \Delta t_{42}^{\text{Spin}}(\hat{S}, \nu), \quad (\text{C94})$$

where

$$\Delta t_{42}^{\text{orb}}(\nu) = \frac{1 + a_1^{\Delta t_{42}} \nu + a_2^{\Delta t_{42}} \nu^2}{1 + a_3^{\Delta t_{42}} \nu + a_4^{\Delta t_{42}} \nu^2}, \quad (\text{C95})$$

$$\Delta t_{42}^{\text{Spin}}(\hat{S}, \nu = 0) = \frac{1 + b_1^{\Delta t_{42}^0} \hat{S}}{1 + b_2^{\Delta t_{42}^0} \hat{S}}. \quad (\text{C96})$$

For $\nu < 6/25$ the spin factor is approximated by the test-particle fit. For the other regions, it is extrapolated using

$$b_i^{\Delta t_{42}^0} \rightarrow \frac{b_1^{\Delta t_{42}^0} + c_{i1}^{\Delta t_{42}} \nu}{1 + c_{i2}^{\Delta t_{42}} \nu}, \quad (\text{C97})$$

with $i = \{1, 2\}$. The explicit values of the coefficients of the fits are listed in Table XXVII.

h. $(\ell, m) = (5, 5)$ multipole

For this multipole, the peak amplitude is written as the sum of two terms as

$$\hat{A}_{55}^{\text{peak}} = \hat{A}_{55}^{\text{peak}_0} X_{12}(1 - 2\nu) \hat{A}_{55}^{\text{orb}}(\nu) + \hat{A}_{55}^{\text{Spin}}(\tilde{a}_{12}, \nu), \quad (\text{C98})$$

TABLE XXVII. Explicit coefficients of the fits of $\hat{A}_{42}^{\text{peak}}$, $\omega_{42}^{\text{peak}}$ and Δt_{42} .

$\hat{A}_{42}^{\text{peak}_0}$	=	0.0314364	$\omega_{42}^{\text{peak}_0}$	=	0.617533	Δt_{42}^0	=	11.66665
$a_1^{\hat{A}_{42}}$	=	-4.56243	$a_1^{\omega_{42}}$	=	-7.44121	$a_1^{\Delta t_{42}}$	=	-9.844617
$a_2^{\hat{A}_{42}}$	=	6.4522	$a_2^{\omega_{42}}$	=	14.233	$a_2^{\Delta t_{42}}$	=	23.32294
			$a_3^{\omega_{42}}$	=	-6.61754	$a_3^{\Delta t_{42}}$	=	-5.760481
			$a_4^{\omega_{42}}$	=	11.4329	$a_4^{\Delta t_{42}}$	=	7.121793
$b_1^{\hat{A}_{42}^0}$	=	-1.63682	$b_1^{\omega_{42}^0}$	=	-2.37589	$b_1^{\Delta t_{42}^0}$	=	-1.3002045
$b_2^{\hat{A}_{42}^0}$	=	0.854459	$b_2^{\omega_{42}^0}$	=	1.97249	$b_2^{\Delta t_{42}^0}$	=	-0.9494348
$b_3^{\hat{A}_{42}^0}$	=	0.120537	$b_3^{\omega_{42}^0}$	=	-2.36107			
$b_4^{\hat{A}_{42}^0}$	=	-0.399718	$b_4^{\omega_{42}^0}$	=	2.16383			
$c_{11}^{\hat{A}_{42}}$	=	6.53943	$c_{11}^{\omega_{42}}$	=	10.1045	$c_{11}^{\Delta t_{42}}$	=	24.604717
$c_{12}^{\hat{A}_{42}}$	=	-4.00073	$c_{12}^{\omega_{42}}$	=	-6.94127	$c_{12}^{\Delta t_{42}}$	=	-0.808279
$c_{21}^{\hat{A}_{42}}$	=	-0.638688	$c_{13}^{\omega_{42}}$	=	12.1857	$c_{21}^{\Delta t_{42}}$	=	62.471781
$c_{22}^{\hat{A}_{42}}$	=	-3.94066	$c_{21}^{\omega_{42}}$	=	-1.62866	$c_{22}^{\Delta t_{42}}$	=	48.340961
$c_{31}^{\hat{A}_{42}}$	=	-0.482148	$c_{22}^{\omega_{42}}$	=	-2.6756			
$c_{32}^{\hat{A}_{42}}$	=	$7.668 \times 10^{-9} - 4$	$c_{23}^{\omega_{42}}$	=	-4.7536			
$c_{41}^{\hat{A}_{42}}$	=	1.25617	$c_{31}^{\omega_{42}}$	=	10.071			
$c_{42}^{\hat{A}_{42}}$	=	-4.04848	$c_{32}^{\omega_{42}}$	=	-6.7299			
			$c_{33}^{\omega_{43}}$	=	12.0377			
			$c_{41}^{\omega_{42}}$	=	-8.56139			
			$c_{42}^{\omega_{42}}$	=	-5.27136			
			$c_{43}^{\omega_{43}}$	=	5.10653			

where $\hat{A}_{55}^{\text{peak}_0}$ is the peak amplitude in the test particle limit. The non-spinning ν -dependence is modeled as

$$\hat{A}_{55}^{\text{orb}}(\nu) = 1 + a_1^{\hat{A}_{55}} \nu + a_2^{\hat{A}_{55}} \nu^2. \quad (\text{C99})$$

The spin dependence is first fitted to the test-particle limit using

$$\hat{A}_{55}^{\text{Spin}}(\tilde{a}_{12}, \nu = 0) = \frac{b_1^{\hat{A}_{55}^0} \tilde{a}_{12}}{1 + b_2^{\hat{A}_{55}^0} \tilde{a}_{12}}, \quad (\text{C100})$$

and then extrapolated to the comparable mass region through

$$b_1^{\hat{A}_{55}^0} \rightarrow \frac{b_1^{\hat{A}_{55}^0}}{1 + c_{11}^{\hat{A}_{55}} \nu + c_{12}^{\hat{A}_{55}} \nu^2}, \quad (\text{C101})$$

$$b_2^{\hat{A}_{55}^0} \rightarrow \frac{b_2^{\hat{A}_{55}^0}}{1 + c_{21}^{\hat{A}_{55}} \nu + c_{22}^{\hat{A}_{55}} \nu^2}. \quad (\text{C102})$$

The frequency of the (5, 5) mode is factorized as

$$\omega_{55}^{\text{peak}} = \omega_{55}^{\text{peak}_0} \omega_{55}^{\text{orb}}(\nu) \omega_{55}^{\text{Spin}}(\hat{S}, \nu), \quad (\text{C103})$$

where

$$\omega_{55}^{\text{orb}}(\nu) = \frac{1 + a_1^{\omega_{55}} \nu + a_2^{\omega_{55}} \nu^2}{1 + a_3^{\omega_{55}} \nu}, \quad (\text{C104})$$

and the test-particle spin factor is given by

$$\omega_{55}^{\text{Spin}}(\hat{S}, \nu = 0) = \frac{1 + b_1^{\omega_{55}^0} \hat{S}}{1 + b_2^{\omega_{55}^0} \hat{S}}. \quad (\text{C105})$$

The spin dependence in the general case is obtained by means of

$$b_i^{\omega_{55}^0} \rightarrow \frac{b_i^{\omega_{55}^0} + c_{i1}^{\omega_{55}} \nu}{1 + c_{i2}^{\omega_{55}} \nu}, \quad (\text{C106})$$

with $i = \{1, 2\}$. Note that, in this case, we do not incorporate spin-dependence in Δ_{55} , but only rely on the nonspinning fit of Ref. [30].

3. NR-fitting of the postpeak parameters

In this Appendix we report the fits of the postpeak parameters ($c_3^{A_{\ell m}}, c_3^{\phi_{\ell m}}, c_4^{\phi_{\ell m}}$) for all multipoles multipoles discussed in the main text. For (2, 2), (3, 3), (4, 4), (5, 5) we present fits that explicitly depend on the spins of the black holes. By contrast, the same parameters for the other multipoles (2, 1), (3, 2), (3, 1) (4, 3), (4, 2), are approximated by the spin-independent fits of Ref. [30]. Let us note, however, that we prefer to *not use* the full spin-dependent fits of ($c_3^{\phi_{33}}, c_4^{\phi_{33}}$) and in ($c_3^{\phi_{44}}, c_4^{\phi_{44}}$). Instead the fits of Ref. [30] are used to get a more robust behavior

TABLE XXVIII. Explicit coefficients of the fits of $\hat{A}_{55}^{\text{peak}}$ and $\omega_{55}^{\text{peak}}$

$\hat{A}_{55}^{\text{peak}_0}$	=	0.00522697	$\omega_{55}^{\text{peak}_0}$	=	0.818117
$a_1^{A_{55}}$	=	-0.29628	$a_1^{\omega_{55}}$	=	-2.8918
$a_2^{A_{55}}$	=	6.4207	$a_2^{\omega_{55}}$	=	-3.2012
			$a_3^{\omega_{55}}$	=	-3.773
$b_1^{A_{55}^0}$	=	0.04360530	$b_1^{\omega_{55}^0}$	=	-0.332703
$b_2^{A_{55}^0}$	=	-0.5769451	$b_2^{\omega_{55}^0}$	=	-0.675738
$c_{11}^{A_{55}}$	=	5.720690	$c_{11}^{\omega_{55}}$	=	1.487294
$c_{12}^{A_{55}}$	=	44.868515	$c_{12}^{\omega_{55}}$	=	-2.058537
$c_{21}^{A_{55}}$	=	12.777090	$c_{21}^{\omega_{55}}$	=	1.454248
$c_{22}^{A_{55}}$	=	-42.548247	$c_{22}^{\omega_{55}}$	=	-1.301284

of ω_{33} and ω_{44} in all corners of the parameter space, notably when the mass ratio is between one and two and the spins are large. See Appendix C 4 for a brief discussion.

a. *The $(\ell, m) = (2, 2)$ postpeak*

The data of $(c_3^{A_{22}}, c_3^{\phi_{22}}, c_4^{\phi_{22}})$ were extracted from NR fitting the NR waveforms in the calibration set over an interval starting at the peak of length $4\tau_1^{22}$.

The fits are done in three steps, based on the model

$$Y(\nu; \hat{S}) = b_0^Y(\nu) + b_1^Y(X_{12})\hat{S} + b_2^Y(X_{12})\hat{S}^2 + b_3^Y(X_{12})\hat{S}^3 + b_4^Y(X_{12})\hat{S}^4. \quad (\text{C107})$$

In the first step $Y(\nu; \hat{S} = 0)$ is fitted to the non-spinning data. In the second step $b_i^Y(X_{12} = 0)$ are fitted to the equal mass data. In the third and final step the fits are extrapolated to the comparable mass case imposing the 1-D fits informed in the previous two steps. The coefficients of the fit are listed in Table XXIX.

b. *The $(\ell, m) = (3, 3)$ postpeak*

The data of $(c_3^{A_{33}}, c_3^{\phi_{33}}, c_4^{\phi_{33}})$ were extracted from NR fitting the NR waveforms in the calibration set over an interval starting at the peak of length $1\tau_1^{33}$. The interpolation is modeled with the template

$$Y(\nu; \hat{S}) = b_0^Y(\nu) + b_1^Y(X_{12})\hat{S}. \quad (\text{C108})$$

While for the case of $c_3^{A_{33}}$ the fit is done versus \tilde{a}_{12} . The fits are done in two hierarchical steps. (i) $b_0^Y(\nu)$ is fitted to the non-spinning data. (ii) $b_1^Y(X_{12})$ is fitted with a quadratic polynomial, while imposing the fit of $b_0^Y(\nu)$. The fits are given explicitly in Table XXX.

c. *The $(\ell, m) = (4, 4)$ postpeak*

The data of $(c_3^{A_{44}}, c_3^{\phi_{44}}, c_4^{\phi_{44}})$ were extracted from NR fitting the NR waveforms in the calibration set over an interval starting at the peak of length $1\tau_1^{44}$. The interpolation of $(c_3^{\phi_{44}}, c_4^{\phi_{44}})$ is modeled with the template

$$Y(\nu; \hat{S}) = b_0^Y(\nu) + b_1^Y(X_{12})\hat{S} + b_2^Y(X_{12})\hat{S}^2 \quad (\text{C109})$$

in three steps, similar to the the $(2, 2)$ mode. (i) $b_0^Y(\nu)$ is fitted to the non-spinning data. (ii) $b_i^Y(X_{12} = 0)$ is fitted to the equal mass data. (iii) The full dependence of $b_i^Y(X_{12})$ on X_{12} is fitted while imposing the one-dimensional fits informed in the first two steps. c_{344}^A is modeled with the template

$$c_3^{A_{44}}(\nu; \hat{S}) = b_0^{c_3^{A_{44}}}(\nu) + b_1^{c_3^{A_{44}}}\nu\hat{S} + b_2^{c_3^{A_{44}}}\nu\hat{S}^2. \quad (\text{C110})$$

The fit is done in two steps. (i) $b_0^{c_3^{A_{44}}}(\nu)$ is fitted to the non-spinning data. (ii) The coefficients $b_i^{c_3^{A_{44}}}$ are informed using the spinning data, while imposing the non-spinning fit. The fits are given explicitly in Table XXXI.

d. *The $(\ell, m) = (5, 5)$ postpeak*

The data of $(c_3^{A_{55}}, c_3^{\phi_{55}}, c_4^{\phi_{55}})$ were extracted from NR fitting the NR waveforms in the calibration set over an interval starting at the peak of length $1\tau_1^{55}$. The interpolation is modeled with the template

$$Y(\nu; \hat{S}) = b_0^Y(\nu) + b_1^Y(X_{12})\hat{S} + b_2^Y(X_{12})\hat{S}^2. \quad (\text{C111})$$

While for the case of $c_3^{A_{55}}$ the fit is done versus \tilde{a}_{12} . The fits are done in two hierarchical steps. (i) $b_0^Y(\nu)$ is fitted to the non-spinning data. (ii) $b_i^Y(X_{12})$ are fitted with a linear polynomial, while imposing the fit of $b_0^Y(\nu)$. The fits are given explicitly in Table XXXII.

TABLE XXIX. The fitted coefficients of $(c_3^{A22}, c_3^{\phi22}, c_4^{\phi22})$ as defined in Eq. (C107).

$Y = c_3^{A22}$		$Y = c_3^{\phi22}$		$Y = c_4^{\phi22}$	
$b_0^{c_3^A}(\nu)$	$= -0.5585 \quad 0.81196\nu$	$b_0^{c_3^\phi}(\nu)$	$= 3.8436 \quad +0.71565\nu$	$b_0^{c_4^\phi}(\nu)$	$= 1.4736 \quad 2.2337\nu$
$b_1^{c_3^A}(X_{12})$	$= -0.398576 \quad +0.1659421X_{12}$	$b_1^{c_3^\phi}(X_{12})$	$= 5.12794 \quad -1.323643X_{12}$	$b_1^{c_4^\phi}(X_{12})$	$= 8.26539 \quad +0.779683X_{12}$
$b_2^{c_3^A}(X_{12})$	$= 0.099805 \quad -0.2560047X_{12}$	$b_2^{c_3^\phi}(X_{12})$	$= 9.9136 \quad -3.555007X_{12}$	$b_2^{c_4^\phi}(X_{12})$	$= 14.2053 \quad -0.069638X_{12}$
$b_3^{c_3^A}(X_{12})$	$= 0.72125 \quad -0.9418946X_{12}$	$b_3^{c_3^\phi}(X_{12})$	$= -4.1075 \quad +7.011267X_{12}$	$b_3^{c_4^\phi}(X_{12})$	$= 0$
$b_4^{c_3^A}(X_{12})$	$= 0$	$b_4^{c_3^\phi}(X_{12})$	$= -31.5562 \quad +32.737824X_{12}$	$b_4^{c_4^\phi}(X_{12})$	$= 0$

TABLE XXX. The explicit fits of $(c_3^{A33}, c_3^{\phi33}, c_4^{\phi33})$. The reader should note that the fits of $(c_3^{\phi33}, c_4^{\phi33})$ are not used for any of the results given in the main text. Instead the corresponding fits of Ref. [30] are used. See Appendix C 4 for a brief discussion.

$c_3^{A33}(\nu, X_{12}, \tilde{a}_{12})$	$= -0.5585 \quad +0.81196\nu$	$+$	$(-0.3502608 \quad +1.587606X_{12} \quad -1.555325X_{12}^2)$	\tilde{a}_{12}
$c_3^{\phi33}(\nu, X_{12}, \hat{S})$	$= 3.0611 \quad -6.1597\nu$	$+$	$(-0.634377 \quad +5.983525X_{12} \quad -5.8819X_{12}^2)$	\hat{S}
$c_4^{\phi33}(\nu, X_{12}, \hat{S})$	$= 1.789 \quad -5.6684\nu$	$+$	$(-3.877528 \quad +12.0433X_{12} \quad -6.524665X_{12}^2)$	\hat{S}

4. Motivating the choices for the (3, 3) and (4, 4) postmerger phases

As mentioned above, the results presented in the main text *do not* rely on the fits of $(c_3^{\phi33}, c_4^{\phi33})$ and $(c_3^{\phi44}, c_4^{\phi44})$ given in Appendix C 3 with the full spin dependence, but instead use only their spin-independent part, as already presented Ref. [30]. This choice was made so to ensure a more robust behavior of the frequency at the beginning of the ringdown when the spins are positive and large. We illustrate this argument inspecting the behavior of ω_{44} for two highly-spinning configurations. Figure 22 shows EOB/NR comparisons with two EOB waveforms obtained with either the nonspinning fits (red online) or those with the full spin dependence (green). One sees that the spin-dependent fit performs rather well for **SXS:BBH:1124** (1, 0.998, 0.998), consistently with the fact that we used **SXS:BBH:0178**, with parameters (1, 0.9942, 0.9942), to inform the fit. By contrast, one sees that the same description applied to a different configuration, (1.5, 0.95, 0.95), corresponding to **SXS:BBH:1146**, does not perform equally well, with a nonnegligible gap between the EOB and NR frequencies accumulating right after the peak. One finds, however, that removing the spin-dependence in $(c_3^{\phi44}, c_4^{\phi44})$ allows one to obtain a much closer EOB/NR consistency for **SXS:BBH:1146**. For the other case, moving to the nonspinning description slightly worsens the agreement, both before and after the waveform peak⁸. On the basis of these results, and especially seen the rather good \bar{F} behavior illustrated in Fig. 8, we decided to be simple and

remove the spin dependence in $(c_3^{\phi44}, c_4^{\phi44})$. We applied the same rationale also to the (3, 3) mode. Clearly, in case of very high-spins, current fits should be improved to some extent, increasing the calibration set so to incorporate more points in that corner of the parameter space. This will be investigated in future work.

5. Modeling the NQC extraction points

Let us finally discuss analytic representations of the NR point (amplitude, frequency and derivative) on the multipolar waveform that is needed for computing the NQC corrections to the waveform multipole by multipole. For the (2, 2) and (3, 3) modes we give below dedicated fits. For all other modes, the useful NR quantities are obtained analytically from the (fitted) post-peak analytical waveform discussed above. Let us recall here that, for each mode, the NQC time is always

$$t_{\ell m}^{\text{NQC}} \equiv t_{\ell m}^{\text{peak}} + 2. \quad (\text{C112})$$

All quantities mentioned below with the NQC label are computed at $t = t_{\ell m}^{\text{NQC}}$.

a. The (2, 2) NQC extraction point

For the (2, 2) mode the NQC-point quantities $\{\hat{A}_{22}^{\text{NQC}}, \dot{A}_{22}^{\text{NQC}}, \omega_{22}^{\text{NQC}}, \dot{\omega}_{22}^{\text{NQC}}\}$ are fitted directly. The 3-piece hybrid fit, presented in [24, 37] is modified for $q > 4$. The fits of $\{\hat{A}_{22}^{\text{NQC}}, \omega_{22}^{\text{NQC}}\}$ are done using the template discussed already for the peak, see Appendix C 2 a. The reader should note however that the fit of ω_{22}^{NQC} has additional flexibility. The replacement in (C20) is also done for $i = 2$ for this case. In the following the fitting of

⁸ The reader should note that the postpeak phasing impacts the inspiral waveform through the NQC extraction points obtained from the postpeak template. See Appendix C 5 c

TABLE XXXI. The explicit fits of $(c_3^{A44}, c_3^{\phi44}, c_4^{\phi44})$. The reader should note that the fits of $(c_3^{\phi44}, c_4^{\phi44})$ are not used for any of the results given in the main text. Instead the corresponding fits of Ref. [30] are used. See Appendix C 4 for a brief discussion.

$c_3^{A44}(\nu, \hat{S})$	=	-0.41591	+3.2099 ν	-	9.614738 ν	\hat{S}	+	122.461125 ν	\hat{S}^2
$c_3^{\phi44}(\nu, X_{12}, \hat{S})$	=	$\frac{3.6662-30.072\nu+76.371\nu^2}{1-3.5522\nu}$		+	(-4.9184 +7.911653 X_{12})	\hat{S}	+	(-15.6772 +21.181688 X_{12})	\hat{S}^2
$c_4^{\phi44}(\nu, X_{12}, \hat{S})$	=	0.21595	+23.216 ν	+	(-3.4207 +11.746452 X_{12})	\hat{S}	+	(-15.5383 +34.922883 X_{12})	\hat{S}^2

TABLE XXXII. The explicit fits of $(c_3^{A55}, c_3^{\phi55}, c_4^{\phi55})$.

$c_3^{A55}(\nu, X_{12}, \tilde{a}_{12})$	=	-7.063079	+65.464944 ν	+	(-2.055335 -0.585373 X_{12})	\tilde{a}_{12}	+	(-12.631409 +19.271346 X_{12})	\tilde{a}_{12}^2
$c_3^{\phi55}(\nu, X_{12}, \hat{S})$	=	-1.510167	+30.569461 ν	+	(-2.687133 +4.873750 X_{12})	\hat{S}	+	(-14.629684 +19.696954 X_{12})	\hat{S}^2
$c_4^{\phi55}(\nu, X_{12}, \hat{S})$	=	-1.383721	+56.871881 ν	+	(+7.198729 -3.870998 X_{12})	\hat{S}	+	(-25.992190 +36.882645 X_{12})	\hat{S}^2

$\dot{A}_{22}^{\text{NQC}}$ and $\dot{\omega}_{22}^{\text{NQC}}$. Both rely on the same template thus it is only given for the former explicitly. To fit the time derivative of the amplitude at t_{NQC} it was proven useful to not fit it directly, but to fit $\dot{A}_{22}^{\text{NQC}}/\nu\omega_{22}^{\text{NQC}}$, starting with the following factorization

$$\frac{\dot{A}_{22}^{\text{NQC}}}{\nu\omega_{22}^{\text{NQC}}} = \left[\hat{A}_{22}^{\text{NQC}_{\text{orb}}}(\nu) + \hat{A}_{22}^{\text{NQC}_{\text{spin}}}(X_{12}, \hat{S}) \right]. \quad (\text{C113})$$

The nonspinning contribution is fitted as

$$\hat{A}_{22}^{\text{NQC}_{\text{orb}}}(\nu) = 1 + a_1 \hat{A}_{22}^{\text{NQC}} \nu + a_2 \hat{A}_{22}^{\text{NQC}} \nu^2. \quad (\text{C114})$$

The spin-dependence is represented as

$$\hat{A}_{22}^{\text{NQC}_{\text{spin}}}(X_{12}, \hat{S}) = b_1 \hat{A}_{22}^{\text{NQC}_{m_1=m_2}} \hat{S} + b_1 \hat{A}_{22}^{\text{NQC}_{m_1=m_2}} \hat{S}^2. \quad (\text{C115})$$

The extrapolation to the $m_1 \neq m_2$ regime is done via the replacement

$$b_i \hat{A}_{22}^{\text{NQC}_{m_1=m_2}} \rightarrow b_i \hat{A}_{22}^{\text{NQC}_{m_1=m_2}} + c_i \hat{A}_{22}^{\text{NQC}_{m_1=m_2}} X_{12}, \quad (\text{C116})$$

with $i = \{1, 2\}$. All coefficients are listed explicitly in Table XXXIII.

b. The (3, 3) NQC extraction point

Let us discuss now explicit fits for $\{\hat{A}_{33}^{\text{NQC}}, \dot{A}_{33}^{\text{NQC}}, \omega_{33}^{\text{NQC}}, \dot{\omega}_{33}^{\text{NQC}}\}$. The amplitude $\hat{A}_{33}^{\text{NQC}}$ is written as two separate terms as

$$\hat{A}_{33}^{\text{NQC}} = \hat{A}_{33}^{\text{NQC}_0} X_{12} \hat{A}_{33}^{\text{NQC}_{\text{orb}}}(\nu) + \hat{A}_{33}^{\text{NQC}_S}(\nu, \tilde{a}_{12}), \quad (\text{C117})$$

where $\hat{A}_{33}^{\text{NQC}_0}$ is the test-particle value. The non-spinning sector is fitted after factorization of $\hat{A}_{33}^{\text{NQC}_0} X_{12}$ with

$$\hat{A}_{33}^{\text{NQC}_{\text{orb}}}(\nu) = 1 + a_1 \hat{A}_{33}^{\text{NQC}} \nu + a_2 \hat{A}_{33}^{\text{NQC}} \nu^2. \quad (\text{C118})$$

The spin-dependent factor $\hat{A}_{33}^{\text{NQC}_S}$ is first fitted in the $\nu = 0$ limit with

$$\hat{A}_{33}^{\text{NQC}_S} = \frac{b_1 \hat{A}_{33}^{\text{NQC}} \tilde{a}_{12} + b_2 \hat{A}_{33}^{\text{NQC}} \tilde{a}_{12}^2}{1 + b_3 \hat{A}_{33}^{\text{NQC}} \tilde{a}_{12}}. \quad (\text{C119})$$

and then extended to the $\nu \neq 0$ regime through

$$b_i \hat{A}_{33}^{\text{NQC}} \rightarrow \frac{b_i \hat{A}_{33}^{\text{NQC}} + c_i \hat{A}_{33}^{\text{NQC}} \nu}{1 + c_i \hat{A}_{33}^{\text{NQC}} \nu} \text{ with } i = \{1, 2, 3\}. \quad (\text{C120})$$

The time-derivative of the amplitude $\dot{A}_{33}^{\text{NQC}}$ was fitted in two steps. In the first step, one is fitting only equal-mass data (but, crucially, including also data with unequal spins), as

$$\frac{\dot{A}_{33}^{\text{NQC}_{\nu=1/4}}}{10^5} = d_0 \dot{A}_{33}^{\text{NQC}_{\nu=1/4}} + d_1 \dot{A}_{33}^{\text{NQC}_{\nu=1/4}} \tilde{a}_{12} + d_2 \dot{A}_{33}^{\text{NQC}_{\nu=1/4}} \tilde{a}_{12}^2. \quad (\text{C121})$$

The un-equal mass sector is fitted with the same template as $\hat{A}_{33}^{\text{NQC}}$ with 3 modifications: (i) X_{12} is not factorized as in (C117); (ii) The spin variable in (C119) is chosen to be \hat{S} ; (iii) the transformation is only done for $i = 2$ in (C120), $c_{1i} \hat{A}_{33}^{\text{NQC}} = c_{3i} \hat{A}_{33}^{\text{NQC}} = 0$.

Moving now to the NQC frequency ω_{33}^{NQC} , we assume the following factorization

$$\omega_{33}^{\text{NQC}} = \omega_{33}^{\text{NQC}_0} \omega_{33}^{\text{NQC}_{\text{orb}}} \omega_{33}^{\text{NQC}_S}, \quad (\text{C122})$$

where $\omega_{33}^{\text{NQC}_{\text{orb}}}$ is fitted to the nonspinning data with a second-order polynomial in ν as

$$\omega_{33}^{\text{NQC}_{\text{orb}}} = 1 + a_1 \omega_{33}^{\text{NQC}} \nu + a_2 \omega_{33}^{\text{NQC}} \nu^2. \quad (\text{C123})$$

Then, $\omega_{33}^{\text{NQC}_S}$ is fitted to the test-particle data using

$$\omega_{33}^{\text{NQC}_S} = \frac{1 + b_1 \omega_{33}^{\text{NQC}} \hat{S}}{1 + b_2 \omega_{33}^{\text{NQC}} \hat{S}}. \quad (\text{C124})$$

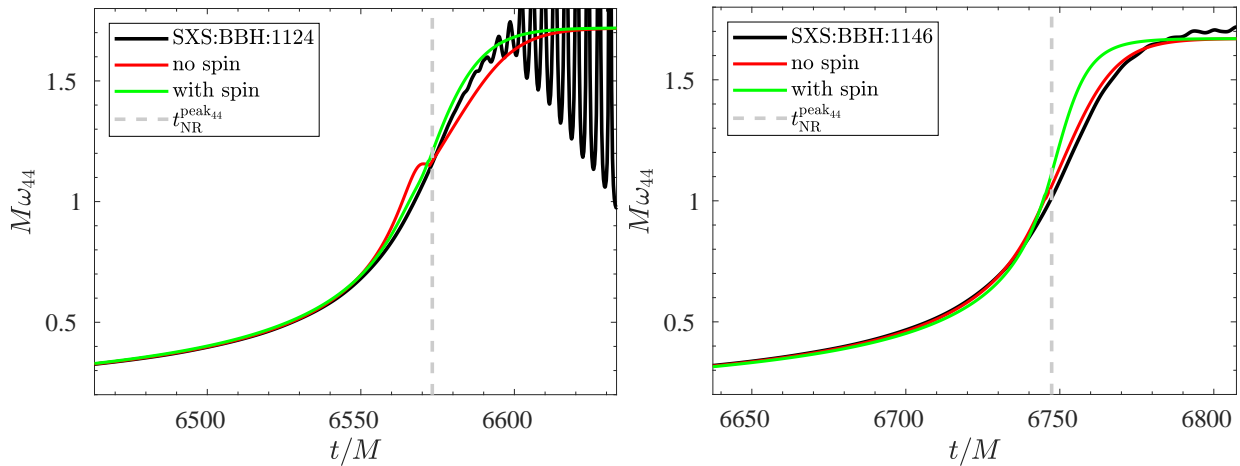


FIG. 22. In this figure we compare the frequency $M\omega_{44}$ for the two NR waveforms (black) SXS:BBH:1124 (1, 0.998, 0.998) (left panel) and SXS:BBH:1146 (1.5, 0.95, 0.95) (right) with the corresponding EOB waveforms, once obtained using the fits of Ref. [30] (right panel) and once with the spin-dependent fits presented in Appendix C 3 (green).

TABLE XXXIII. Coefficients of the (2, 2) quantities needed to calculate the NQC extraction point. From left to right the columns show $\{\hat{A}_{22}^{\text{NQC}}, \dot{A}_{22}^{\text{NQC}}, \omega_{22}^{\text{NQC}}, \dot{\omega}_{22}^{\text{NQC}}\}$.

	$\hat{A}_{22}^{\text{NQC}}$	$\dot{A}_{22}^{\text{NQC}}$	ω_{22}^{NQC}	$\dot{\omega}_{22}^{\text{NQC}}$			
$\hat{A}_{22}^{\text{NQC}_0}$	= 0.294773	$\dot{A}_{22}^{\text{NQC}_0}/\nu$	= -0.000243654	$\omega_{22}^{\text{NQC}_0}$	= 0.285588	$\dot{\omega}_{22}^{\text{NQC}_0}$	= 0.00628027
$a_1^{\hat{A}_{22}^{\text{NQC}}}$	= -0.052697	$a_1^{\dot{A}_{22}^{\text{NQC}}}$	= 2.86637	$a_1^{\omega_{22}^{\text{NQC}}}$	= 0.91704	$a_1^{\dot{\omega}_{22}^{\text{NQC}}}$	= 2.4351
$a_2^{\hat{A}_{22}^{\text{NQC}}}$	= 1.6088	$a_2^{\dot{A}_{22}^{\text{NQC}}}$	= -1.3667	$a_2^{\omega_{22}^{\text{NQC}}}$	= 1.7912	$a_2^{\dot{\omega}_{22}^{\text{NQC}}}$	= 4.4928
$b_1^{\hat{A}_{22}^{\text{NQC}_{m_1=m_2}}}$	= -0.705226	$b_1^{\dot{A}_{22}^{\text{NQC}_{m_1=m_2}}}$	= 0.02679530	$b_1^{\omega_{22}^{\text{NQC}_{m_1=m_2}}}$	= -0.46550	$b_1^{\dot{\omega}_{22}^{\text{NQC}_{m_1=m_2}}}$	= 0.001425242
$b_2^{\hat{A}_{22}^{\text{NQC}_{m_1=m_2}}}$	= -0.0953944	$b_2^{\dot{A}_{22}^{\text{NQC}_{m_1=m_2}}}$	= -0.0064409	$b_2^{\omega_{22}^{\text{NQC}_{m_1=m_2}}}$	= -0.078787	$b_2^{\dot{\omega}_{22}^{\text{NQC}_{m_1=m_2}}}$	= -0.00096073
$b_3^{\hat{A}_{22}^{\text{NQC}_{m_1=m_2}}}$	= -1.087280			$b_3^{\omega_{22}^{\text{NQC}_{m_1=m_2}}}$	= -0.852284		
$c_1^{\hat{A}_{22}^{\text{NQC}}}$	= 0.009335	$c_1^{\dot{A}_{22}^{\text{NQC}}}$	= -0.015395218	$c_1^{\omega_{22}^{\text{NQC}}}$	= -0.338008	$c_1^{\dot{\omega}_{22}^{\text{NQC}}}$	= -0.000063766
$c_{12}^{\hat{A}_{22}^{\text{NQC}}}$	= 0.582869	$c_2^{\dot{A}_{22}^{\text{NQC}}}$	= 0.008732589	$c_{12}^{\omega_{22}^{\text{NQC}}}$	= 1.077812	$c_{12}^{\dot{\omega}_{22}^{\text{NQC}}}$	= 0.000513197
				$c_{21}^{\omega_{22}^{\text{NQC}}}$	= 0.0555533		
				$c_{22}^{\omega_{22}^{\text{NQC}}}$	= -0.312861		
$c_{31}^{\hat{A}_{22}^{\text{NQC}}}$	= -0.140747			$c_{31}^{\omega_{22}^{\text{NQC}}}$	= 0.289185		
$c_{32}^{\hat{A}_{22}^{\text{NQC}}}$	= 0.505807			$c_{32}^{\omega_{22}^{\text{NQC}}}$	= -0.195838		

Finally, the spin-dependence in $\omega_{33}^{\text{NQC}_S}$ incorporates ν -dependent effects as

$$b_i^{\omega_{33}^{\text{NQC}}} \rightarrow b_i^{\omega_{33}^{\text{NQC}}} + c_i^{\omega_{33}^{\text{NQC}}} \nu \text{ with } i = \{1, 2\}. \quad (\text{C125})$$

Moving finally to the time-derivative of the frequency, $\dot{\omega}_{33}^{\text{NQC}}$, it is fitted with the ansatz

$$\dot{\omega}_{33}^{\text{NQC}} = \dot{\omega}_{33}^{\text{NQC}_0} \dot{\omega}_{33}^{\text{NQC}_{\text{orb}}} + \dot{\omega}_{33}^{\text{NQC}_S}, \quad (\text{C126})$$

where $\dot{\omega}_{33}^{\text{NQC}_{\text{orb}}}$ is fitted to nonspinning data with

$$\dot{\omega}_{33}^{\text{NQC}_{\text{orb}}} = 1 + a_1^{\dot{\omega}_{33}^{\text{NQC}}} \nu. \quad (\text{C127})$$

$\dot{\omega}_{33}^{\text{NQC}_S}$ if fitted to the test-particle data with

$$\dot{\omega}_{33}^{\text{NQC}_S} = b_1^{\dot{\omega}_{33}^{\text{NQC}_S}} \hat{S} + b_2^{\dot{\omega}_{33}^{\text{NQC}_S}} \hat{S}^2. \quad (\text{C128})$$

The spin dependence in $\dot{\omega}_{33}^{\text{NQC}_S}$ is then extrapolated to the comparable mass through

$$b_i^{\dot{\omega}_{33}^{\text{NQC}_S}} \rightarrow b_i^{\dot{\omega}_{33}^{\text{NQC}_S}} + c_i^{\dot{\omega}_{33}^{\text{NQC}_S}} \nu \text{ with } i = \{1, 2\}. \quad (\text{C129})$$

TABLE XXXIV. Coefficients of the (3, 3) quantities needed to calculate the NQC extraction point. From left to right the columns show $\{\hat{A}_{33}^{\text{NQC}}, \dot{\hat{A}}_{33}^{\text{NQC}}, \omega_{33}^{\text{NQC}}, \dot{\omega}_{33}^{\text{NQC}}\}$.

$\hat{A}_{33}^{\text{NQC}}$		$\dot{\hat{A}}_{33}^{\text{NQC}}$		ω_{33}^{NQC}		$\dot{\omega}_{33}^{\text{NQC}}$	
$\hat{A}_{33}^{\text{NQC}_0}$	= 0.0512928	$\hat{A}_{33}^{\text{NQC}_0}/\nu$	= -3.9568×10^{-4}	$\omega_{33}^{\text{NQC}_0}$	= 0.476647	$\dot{\omega}_{33}^{\text{NQC}_0}$	= 0.0110394
$a_1^{\hat{A}_{33}^{\text{NQC}}}$	= 0.09537	$a_1^{\dot{\hat{A}}_{33}^{\text{NQC}}}$	= 1.0985	$a_1^{\omega_{33}^{\text{NQC}}}$	= 1.0886	$a_1^{\dot{\omega}_{33}^{\text{NQC}}}$	= 2.7962
$a_2^{\hat{A}_{33}^{\text{NQC}}}$	= 3.7217	$a_2^{\dot{\hat{A}}_{33}^{\text{NQC}}}$	= -13.458	$a_2^{\omega_{33}^{\text{NQC}}}$	= 3.0658		
$b_1^{\hat{A}_{33}^{\text{NQC}_{\nu=0}}}$	= 0.00924494	$b_1^{\dot{\hat{A}}_{33}^{\text{NQC}_{\nu=0}}}$	= 1.41504×10^{-4}	$b_1^{\omega_{33}^{\text{NQC}_{\nu=0}}}$	= -0.236271	$b_1^{\dot{\omega}_{33}^{\text{NQC}_{\nu=0}}}$	= -4.5666×10^{-4}
$b_2^{\hat{A}_{33}^{\text{NQC}_{\nu=0}}}$	= -8.7052×10^{-5}	$b_2^{\dot{\hat{A}}_{33}^{\text{NQC}_{\nu=0}}}$	= 1.04680×10^{-4}	$b_2^{\omega_{33}^{\text{NQC}_{\nu=0}}}$	= -0.582892	$b_2^{\dot{\omega}_{33}^{\text{NQC}_{\nu=0}}}$	= -0.00388909
$b_3^{\hat{A}_{33}^{\text{NQC}_{\nu=0}}}$	= -0.479669	$b_3^{\dot{\hat{A}}_{33}^{\text{NQC}_{\nu=0}}}$	= -0.422066				
$c_{11}^{\hat{A}_{33}^{\text{NQC}}}$	= 0.0067063	$c_{21}^{\hat{A}_{33}^{\text{NQC}}}$	= -4.671176×10^{-4}	$c_1^{\omega_{33}^{\text{NQC}}}$	= -0.085544	$c_1^{\dot{\omega}_{33}^{\text{NQC}}}$	= 0.0290846
$c_{12}^{\hat{A}_{33}^{\text{NQC}}}$	= 4.814781	$c_{22}^{\hat{A}_{33}^{\text{NQC}}}$	= -4.0270198	$c_2^{\omega_{33}^{\text{NQC}}}$	= -0.523365	$c_2^{\dot{\omega}_{33}^{\text{NQC}}}$	= 0.0087659
$c_{21}^{\hat{A}_{33}^{\text{NQC}}}$	= 0.0111876	$d_0^{\hat{A}_{33}^{\text{NQC}_{\nu=1/4}}}$	= -0.090676				
$c_{22}^{\hat{A}_{33}^{\text{NQC}}}$	= -1.079532	$d_1^{\hat{A}_{33}^{\text{NQC}_{\nu=1/4}}}$	= -5.1643				
$c_{31}^{\hat{A}_{33}^{\text{NQC}}}$	= 2.967227	$d_2^{\hat{A}_{33}^{\text{NQC}_{\nu=1/4}}}$	= -3.2594				
$c_{32}^{\hat{A}_{33}^{\text{NQC}}}$	= -2.571783						

c. Calculation of NQC quantities from the postpeak analytical waveform

Let us finally discuss explicitly the computation of the NQC quantities $(A_{\ell m}^{\text{NQC}}, \omega_{\ell m}^{\text{NQC}}, \dot{A}_{\ell m}^{\text{NQC}}, \dot{\omega}_{\ell m}^{\text{NQC}})$ from

the NR-informed analytical description of the postpeak waveform, as defined in Sec. V A of [30], to which we refer the reader for the notation. Although the formulas have to be intended valid multipole by multipole, in the following we drop the (ℓ, m) indexes for clarity. The analytical expression for the amplitude and its time derivative read

$$A_h/\nu = e^{-\alpha_1 \frac{t-t_{\text{peak}}}{M_{\text{BH}}}} \left[c_1^A \tanh \left(c_2^A \frac{t-t_{\text{peak}}}{M_{\text{BH}}} + c_3^A \right) + c_4^A \right], \quad (\text{C130})$$

$$\dot{A}_h/\nu = \frac{c_1^A c_2^A e^{-\alpha_1 \frac{t-t_{\text{peak}}}{M_{\text{BH}}}} \text{sech}^2 \left(c_2^A \frac{t-t_{\text{peak}}}{M_{\text{BH}}} + c_3^A \right)}{M_{\text{BH}}} - \frac{\alpha_1 e^{-\alpha_1 \frac{t-t_{\text{peak}}}{M_{\text{BH}}}} \left[c_1^A \tanh \left(c_2^A \frac{t-t_{\text{peak}}}{M_{\text{BH}}} + c_3^A \right) + c_4^A \right]}{M_{\text{BH}}}, \quad (\text{C131})$$

while those for the phase and its derivatives read

$$\phi_h = -\omega_1 \frac{t-t_{\text{peak}}}{M_{\text{BH}}^2} - c_1^\phi \ln \left(\frac{1 + c_3^\phi e^{-c_2^\phi \frac{t-t_{\text{peak}}}{M_{\text{BH}}}} + c_4^\phi e^{-2c_2^\phi \frac{t-t_{\text{peak}}}{M_{\text{BH}}}}}{1 + c_3^\phi + c_4^\phi} \right), \quad (\text{C132})$$

$$\omega_h = -\dot{\phi}_h = \frac{\omega_1}{M_{\text{BH}}^2} - \frac{c_1^\phi c_2^\phi}{M_{\text{BH}}} \frac{c_3^\phi x(t) + 2c_4^\phi x^2(t)}{1 + c_3^\phi x(t) + c_4^\phi x^2(t)}, \quad (\text{C133})$$

$$\dot{\omega}_h = -\ddot{\phi}_h = \frac{c_1^\phi c_2^{\phi 2}}{M_{\text{BH}}^2} \left[\frac{c_3^\phi x(t) + 4c_4^\phi x^2(t)}{1 + c_3^\phi x(t) + c_4^\phi x^2(t)} - \left(\frac{c_3^\phi x(t) + 2c_4^\phi x^2(t)}{1 + c_3^\phi x(t) + c_4^\phi x^2(t)} \right)^2 \right], \quad (\text{C134})$$

where we introduced

$$x(t) = e^{-c_2^\phi \frac{t-t_{\text{peak}}}{M_{\text{BH}}}}. \quad (\text{C135})$$

The waveform quantities needed to compute the NQC correction to amplitude and phase are simply obtained by

evaluating the above expressions at $t = t_{\ell m}^{\text{NQC}} = t_{\ell m}^{\text{peak}} + 2$ multipole by multipole.

TABLE XXXV. Explicit coefficients of the fit of $\dot{A}_{44}^{\text{NQC}}$.

$\dot{A}_{44}^{\text{NQC}_0}$	=	-1.52614×10^{-4}
$a_1^{\dot{A}_{44}^{\text{NQC}}}$	=	-7.63783
$a_2^{\dot{A}_{44}^{\text{NQC}}}$	=	15.8089
$a_3^{\dot{A}_{44}^{\text{NQC}}}$	=	-5.88951
$a_4^{\dot{A}_{44}^{\text{NQC}}}$	=	11.1555
$b_1^{\dot{A}_{44}^{\text{NQC}}}$	=	3.76236×10^{-5}
$b_2^{\dot{A}_{44}^{\text{NQC}}}$	=	-0.819379
$c_{11}^{\dot{A}_{44}^{\text{NQC}}}$	=	-6.45958×10^{-6}
$c_{12}^{\dot{A}_{44}^{\text{NQC}}}$	=	-2.35613
$c_{21}^{\dot{A}_{44}^{\text{NQC}}}$	=	-298.678
$c_{22}^{\dot{A}_{44}^{\text{NQC}}}$	=	-1063.08

d. *The fitted derivative of the $(\ell, m) = (4, 4)$ amplitude at the NQC extraction point*

Unfortunately, we have realized that the accuracy of the derivative obtained with the above template does not always have sufficient accuracy. This is due to insufficient flexibility of the fitting template, that will be modified in future work. To overcome this difficulty, we give here an explicit fit of the amplitude time-derivative that is then

used in the main text. The derivative of NQC amplitude is separated in two terms as

$$\dot{A}_{44}^{\text{NQC}} = \nu \dot{A}_{44}^{\text{NQC}_0} \hat{A}_{44}^{\text{orb}}(\nu) + \hat{A}_{44}^{\text{Spin}}(\hat{S}, \nu), \quad (\text{C136})$$

where $\dot{A}_{44}^{\text{NQC}_0}$ is the peak amplitude in the test particle limit. The non-spinning behavior is modeled with

$$\hat{A}_{44}^{\text{orb}}(\nu) = \frac{1 + a_1^{\dot{A}_{44}^{\text{NQC}}} \nu + a_2^{\dot{A}_{44}^{\text{NQC}}} \nu^2}{1 + a_3^{\dot{A}_{44}^{\text{NQC}}} \nu + a_4^{\dot{A}_{44}^{\text{NQC}}} \nu^2}. \quad (\text{C137})$$

The spin dependence is first fitted to the test-particle limit using

$$\hat{A}_{44}^{\text{Spin}}(\hat{S}, \nu = 0) = \frac{b_1^{\dot{A}_{44}^{\text{NQC}}} \hat{S}}{1 + b_2^{\dot{A}_{44}^{\text{NQC}}} \hat{S}}, \quad (\text{C138})$$

and then extrapolated to the comparable mass region through

$$b_1^{\dot{A}_{44}^{\text{NQC}}} \rightarrow \frac{b_1^{\dot{A}_{44}^{\text{NQC}}} + c_{11}^{\dot{A}_{44}^{\text{NQC}}} \nu}{1 + c_{12}^{\dot{A}_{44}^{\text{NQC}}} \nu}, \quad (\text{C139})$$

$$b_2^{\dot{A}_{44}^{\text{NQC}}} \rightarrow \frac{b_2^{\dot{A}_{44}^{\text{NQC}}} + c_{21}^{\dot{A}_{44}^{\text{NQC}}} \nu}{1 + c_{22}^{\dot{A}_{44}^{\text{NQC}}} \nu}. \quad (\text{C140})$$

-
- [1] J. Aasi *et al.* (LIGO Scientific), *Class. Quant. Grav.* **32**, 074001 (2015), arXiv:1411.4547 [gr-qc].
- [2] F. Acernese *et al.* (VIRGO), *Class. Quant. Grav.* **32**, 024001 (2015), arXiv:1408.3978 [gr-qc].
- [3] B. P. Abbott *et al.* (Virgo, LIGO Scientific), *Phys. Rev. Lett.* **116**, 061102 (2016), arXiv:1602.03837 [gr-qc].
- [4] B. P. Abbott *et al.* (Virgo, LIGO Scientific), *Phys. Rev. Lett.* **116**, 241103 (2016), arXiv:1606.04855 [gr-qc].
- [5] B. P. Abbott *et al.* (VIRGO, LIGO Scientific), *Phys. Rev. Lett.* **118**, 221101 (2017), arXiv:1706.01812 [gr-qc].
- [6] B. P. Abbott *et al.* (Virgo, LIGO Scientific), *Astrophys. J.* **851**, L35 (2017), arXiv:1711.05578 [astro-ph.HE].
- [7] B. P. Abbott *et al.* (Virgo, LIGO Scientific), *Phys. Rev. Lett.* **119**, 141101 (2017), arXiv:1709.09660 [gr-qc].
- [8] B. P. Abbott *et al.* (LIGO Scientific, Virgo), *Phys. Rev.* **X9**, 031040 (2019), arXiv:1811.12907 [astro-ph.HE].
- [9] B. P. Abbott *et al.* (Virgo, LIGO Scientific), *Phys. Rev. Lett.* **119**, 161101 (2017), arXiv:1710.05832 [gr-qc].
- [10] B. Abbott *et al.* (LIGO Scientific, Virgo), *Astrophys. J. Lett.* **892**, L3 (2020), arXiv:2001.01761 [astro-ph.HE].
- [11] R. O’Shaughnessy, B. Farr, E. Ochsner, H.-S. Cho, V. Raymond, C. Kim, and C.-H. Lee, *Phys. Rev.* **D89**, 102005 (2014), arXiv:1403.0544 [gr-qc].
- [12] V. Varma and P. Ajith, *Phys. Rev.* **D96**, 124024 (2017), arXiv:1612.05608 [gr-qc].
- [13] L. London, S. Khan, E. Fauchon-Jones, X. J. Forteza, M. Hannam, S. Husa, C. Kalaghatgi, F. Ohme, and F. Pannarale, *Phys. Rev. Lett.* **120**, 161102 (2018), arXiv:1708.00404 [gr-qc].
- [14] A. K. Mehta, C. K. Mishra, V. Varma, and P. Ajith, *Phys. Rev.* **D96**, 124010 (2017), arXiv:1708.03501 [gr-qc].
- [15] R. Cotesta, A. Buonanno, A. Bohé, A. Taracchini, I. Hinder, and S. Ossokine, *Phys. Rev.* **D98**, 084028 (2018), arXiv:1803.10701 [gr-qc].
- [16] V. Varma, S. E. Field, M. A. Scheel, J. Blackman, L. E. Kidder, and H. P. Pfeiffer, *Phys. Rev.* **D99**, 064045 (2019), arXiv:1812.07865 [gr-qc].
- [17] A. Buonanno and T. Damour, *Phys. Rev.* **D59**, 084006 (1999), arXiv:gr-qc/9811091.
- [18] A. Buonanno and T. Damour, *Phys. Rev.* **D62**, 064015 (2000), arXiv:gr-qc/0001013.
- [19] T. Damour, P. Jaranowski, and G. Schaefer, *Phys. Rev.* **D62**, 084011 (2000), arXiv:gr-qc/0005034 [gr-qc].
- [20] T. Damour, *Phys. Rev.* **D64**, 124013 (2001), arXiv:gr-qc/0103018.
- [21] T. Damour, P. Jaranowski, and G. Schäfer, *Phys. Rev.* **D91**, 084024 (2015), arXiv:1502.07245 [gr-qc].
- [22] A. Bohé *et al.*, *Phys. Rev.* **D95**, 044028 (2017), arXiv:1611.03703 [gr-qc].
- [23] S. Ossokine *et al.*, (2020), arXiv:2004.09442 [gr-qc].
- [24] A. Nagar *et al.*, *Phys. Rev.* **D98**, 104052 (2018), arXiv:1806.01772 [gr-qc].
- [25] LIGO Scientific Collaboration, “LIGO Algorithm Library - LALSuite,” free software (GPL) (2018).

- [26] A. Nagar and P. Rettegno, Phys. Rev. **D99**, 021501 (2019), arXiv:1805.03891 [gr-qc].
- [27] S. Akcay, S. Bernuzzi, F. Messina, A. Nagar, N. Ortiz, and P. Rettegno, Phys. Rev. **D99**, 044051 (2019), arXiv:1812.02744 [gr-qc].
- [28] A. Nagar, F. Messina, P. Rettegno, D. Bini, T. Damour, A. Geralico, S. Akcay, and S. Bernuzzi, Phys. Rev. **D99**, 044007 (2019), arXiv:1812.07923 [gr-qc].
- [29] P. Rettegno, F. Martinetti, A. Nagar, D. Bini, G. Riemenschneider, and T. Damour, (2019), arXiv:1911.10818 [gr-qc].
- [30] A. Nagar, G. Pratten, G. Riemenschneider, and R. Gamba, (2019), arXiv:1904.09550 [gr-qc].
- [31] A. Nagar and A. Shah, Phys. Rev. **D94**, 104017 (2016), arXiv:1606.00207 [gr-qc].
- [32] F. Messina, A. Maldarella, and A. Nagar, Phys. Rev. **D97**, 084016 (2018), arXiv:1801.02366 [gr-qc].
- [33] T. Damour and A. Nagar, Phys.Rev. **D90**, 044018 (2014), arXiv:1406.6913 [gr-qc].
- [34] A. Nagar, T. Damour, C. Reisswig, and D. Pollney, Phys. Rev. **D93**, 044046 (2016), arXiv:1506.08457 [gr-qc].
- [35] T. Damour and A. Nagar, Phys.Rev. **D90**, 024054 (2014), arXiv:1406.0401 [gr-qc].
- [36] W. Del Pozzo and A. Nagar, Phys. Rev. **D95**, 124034 (2017), arXiv:1606.03952 [gr-qc].
- [37] A. Nagar, G. Riemenschneider, and G. Pratten, Phys. Rev. **D96**, 084045 (2017), arXiv:1703.06814 [gr-qc].
- [38] M. Boyle *et al.*, Class. Quant. Grav. **36**, 195006 (2019), arXiv:1904.04831 [gr-qc].
- [39] T. Damour, B. R. Iyer, and A. Nagar, Phys. Rev. **D79**, 064004 (2009), arXiv:0811.2069 [gr-qc].
- [40] Y. Pan, A. Buonanno, R. Fujita, E. Racine, and H. Tagoshi, Phys.Rev. **D83**, 064003 (2011), arXiv:1006.0431 [gr-qc].
- [41] A. Nagar, F. Messina, C. Kavanagh, G. Lukes-Gerakopoulos, N. Warburton, S. Bernuzzi, and E. Harms, Phys. Rev. **D100**, 104056 (2019), arXiv:1907.12233 [gr-qc].
- [42] T. Damour, A. Nagar, and S. Bernuzzi, Phys.Rev. **D87**, 084035 (2013), arXiv:1212.4357 [gr-qc].
- [43] R. Fujita, PTEP **2015**, 033E01 (2015), arXiv:1412.5689 [gr-qc].
- [44] E. Harms, S. Bernuzzi, A. Nagar, and A. Zenginoglu, Class.Quant.Grav. **31**, 245004 (2014), arXiv:1406.5983 [gr-qc].
- [45] “SXS Gravitational Waveform Database,” <https://data.black-holes.org/waveforms/index.html>.
- [46] L. T. Buchman, H. P. Pfeiffer, M. A. Scheel, and B. Szilagy, Phys. Rev. **D86**, 084033 (2012), arXiv:1206.3015 [gr-qc].
- [47] T. Chu, H. P. Pfeiffer, and M. A. Scheel, Phys. Rev. **D80**, 124051 (2009), arXiv:0909.1313 [gr-qc].
- [48] D. A. Hemberger, G. Lovelace, T. J. Loredo, L. E. Kidder, M. A. Scheel, B. Szilagy, N. W. Taylor, and S. A. Teukolsky, Phys. Rev. **D88**, 064014 (2013), arXiv:1305.5991 [gr-qc].
- [49] M. A. Scheel, M. Giesler, D. A. Hemberger, G. Lovelace, K. Kuper, M. Boyle, B. Szilagy, and L. E. Kidder, Class. Quant. Grav. **32**, 105009 (2015), arXiv:1412.1803 [gr-qc].
- [50] J. Blackman, S. E. Field, C. R. Galley, B. Szilagy, M. A. Scheel, M. Tiglio, and D. A. Hemberger, Phys. Rev. Lett. **115**, 121102 (2015), arXiv:1502.07758 [gr-qc].
- [51] G. Lovelace, M. Boyle, M. A. Scheel, and B. Szilagy, Class. Quant. Grav. **29**, 045003 (2012), arXiv:1110.2229 [gr-qc].
- [52] G. Lovelace, M. Scheel, and B. Szilagy, Phys.Rev. **D83**, 024010 (2011), arXiv:1010.2777 [gr-qc].
- [53] G. Lovelace *et al.*, Class. Quant. Grav. **32**, 065007 (2015), arXiv:1411.7297 [gr-qc].
- [54] A. H. Mroue, M. A. Scheel, B. Szilagy, H. P. Pfeiffer, M. Boyle, *et al.*, Phys.Rev.Lett. **111**, 241104 (2013), arXiv:1304.6077 [gr-qc].
- [55] P. Kumar, K. Barkett, S. Bhagwat, N. Afshari, D. A. Brown, G. Lovelace, M. A. Scheel, and B. Szilagy, Phys. Rev. **D92**, 102001 (2015), arXiv:1507.00103 [gr-qc].
- [56] T. Chu, H. Fong, P. Kumar, H. P. Pfeiffer, M. Boyle, D. A. Hemberger, L. E. Kidder, M. A. Scheel, and B. Szilagy, Class. Quant. Grav. **33**, 165001 (2016), arXiv:1512.06800 [gr-qc].
- [57] “Updated Advanced LIGO sensitivity design curve,” <https://dcc.ligo.org/LIGO-T1800044/public>.
- [58] S. Khan, S. Husa, M. Hannam, F. Ohme, M. Pürrer, X. Jiménez Forteza, and A. Bohé, Phys. Rev. **D93**, 044007 (2016), arXiv:1508.07253 [gr-qc].
- [59] D. Shoemaker, <https://dcc.ligo.org/cgi-bin/DocDB/ShowDocument?docid=2974>.
- [60] L. Baiotti, T. Damour, B. Giacomazzo, A. Nagar, and L. Rezzolla, Phys. Rev. Lett. **105**, 261101 (2010), arXiv:1009.0521 [gr-qc].
- [61] L. Baiotti, T. Damour, B. Giacomazzo, A. Nagar, and L. Rezzolla, Phys. Rev. **D84**, 024017 (2011), arXiv:1103.3874 [gr-qc].
- [62] A. Taracchini, A. Buonanno, G. Khanna, and S. A. Hughes, Phys.Rev. **D90**, 084025 (2014), arXiv:1404.1819 [gr-qc].
- [63] https://bitbucket.org/eob_ihes/teobresums/src/master/, TEOBResumS code.
- [64] G. Riemenschneider, P. Rettegno, and A. Nagar, in preparation, 2020.
- [65] S. Husa, S. Khan, M. Hannam, M. Pürrer, F. Ohme, X. Jiménez Forteza, and A. Bohé, Phys. Rev. **D93**, 044006 (2016), arXiv:1508.07250 [gr-qc].
- [66] D. Keitel *et al.*, Phys. Rev. **D96**, 024006 (2017), arXiv:1612.09566 [gr-qc].
- [67] X. Jiménez-Forteza, D. Keitel, S. Husa, M. Hannam, S. Khan, and M. Pürrer, Phys. Rev. **D95**, 064024 (2017), arXiv:1611.00332 [gr-qc].